UNIVERSITY OF MILANO

**DOCTORATE SCHOOL IN PHYSICS,
ASTROPHYSICS AND APPLIED PHYSICS**

**DEPARTMENT OF CHEMISTRY, BIOCHEMISTRY
AND MEDICAL BIOTECHNOLOGIES**

**DOCTORATE COURSE IN PHYSICS,
ASTROPHYSICS AND APPLIED PHYSICS
XXII CYCLE**

STUDY OF COLLOIDAL INTERACTIONS MEDIATED BY BIOMOLECULAR RECOGNITION AND BY ELECTROKINETIC FLOWS

FIS/07

Doctorate Thesis of:
Lucia FORNASARI

Advisor: **Prof. Tommaso BELLINI**
Co-advisor: **Dr. Davide PINI**
Director of the school: **Prof. Marco BERSANELLI**

Academic year 2009-2010

ai miei tesori

Letizia, Mattia e Pietro

Abstract

This PhD thesis focuses on new types of interparticle interactions in colloidal dispersions. In particular, it considers interactions mediated by two different phenomena - biomolecular recognition and electrokinetic flows. The general purpose of this investigation is twofold: while we investigate new mechanisms providing new forms of colloidal interactions, we also exploit the measured interactions to better describe the phenomena at their origin. Indeed, the observed colloidal interactions enable to detect both biomolecular recognition and electrokinetic flows with sensitivity hardly achievable in other ways. In all cases, interactions have been investigated by optical techniques: static and dynamic light scattering, electric transmitted light intensity and electric birefringence.

The first part of the thesis reports a systematic study of colloidal interactions performed on a dispersion of charged spherical latex particles having two peculiar properties: their surface can be functionalized with various surfactant molecules and their refractive index is very close to that of water. We have quantified interparticle interactions through the measurement of the second virial coefficients extracted from static and dynamic light scattering measurements. We have studied particles coated with various surfactants and in presence of various ionic strengths. In particular we have studied particles coated with glyco-lipids, so that the colloids are effectively coated with sugar groups. In agreement with previous literature we have found attractive interaction in carbohydrate-coated colloidal dispersions when calcium ions are present in the solution.

The second part of the thesis reports a previously undescribed interaction found when colloidal mixture of large and small colloids charged of the same sign are under the effect of an electric field at low (sub-kHz) frequencies. Measurements of the intensity of the transmitted polarized light as a function of field strength and frequency on rods-spheres mixtures have revealed that the previously observed negative torque acting on the rods at low frequency, is accompanied by a field-induced clearing of the dispersion. Measurements performed on mixtures of large (dilute) and small (semidilute) spherical colloids show that such clearing effect is universal and due to an anisotropic redistribution of the small spheres around the larger ones. $O(E^2)$ electro-osmotic flows, greatly enhanced by the presence of the small spheres, can be the responsible mechanism of the phenomena observed in rod-sphere and sphere-sphere binary mixture of charged colloidal particles.

Contents

Introduction

The thesis reports the investigation of new types of interactions in colloidal dispersions. We studied interactions mediated by two different phenomena - biomolecular recognition and electrokinetic flows. The general purpose of this investigation is twofold: on one side we investigate new mechanisms providing new forms of colloidal interactions, on the other, we exploit the measured interactions to better describe the phenomena that generate them. Indeed, the observed interactions enable to detect both biomolecular recognition and electrokinetic flows with sensitivity hardly achievable in other ways. In all cases, interactions have been investigated by optical techniques: static and dynamic light scattering, electric transmitted light intensity and electric birefringence.

The first part of this thesis is devoted to describing a method for studying biomolecular interactions through light scattering experiments by using colloidal particles as interaction amplifiers. Biomolecular interactions are often very weak and difficult to detect and quantify. The basic idea in our work is to coat colloidal particles with weakly interacting molecular groups and to inspect the behavior of the colloids to extract information on the molecules present on their surface.

The colloids employed in our work are spherical particles with radius $R = 30\,nm$ constituted by a fluorurate polymer. They have two peculiar properties: their surface can be easily coated with various molecular groups and their refractive index differs only slightly from that of water. As a consequence of the latter property, aqueous dispersions remain optically transparent also at high particles volume fractions. Moreover the weak scattering enables measuring the adsorption of molecular groups on particles surface by studying the variation of the light diffused by the colloids as a function of the quantity of adsorbing molecules added to the dispersion.

To evaluate the interaction between the particles we employed static and dynamic light scattering measurements to determine the value of the second virial coefficient B_2. B_2, being a spatial integral of the interaction potential, quantifies the colloidal interactions. In the case of non-interacting particles the diffused intensity depends on the particles volume v_p, on their volume fraction ϕ and on their

refractive index. In the case of interacting particles the diffused light depends also on the interaction potential. It can be shown that in dilute interacting system the diffused intensity I is related to the intensity scattered by the same dispersion in absence of interaction I_0 through a relation involving B_2 and the particles volume fraction ϕ:

$$I = I_0 \left(1 + 2\frac{B_2}{v_p}\phi\right)^{-1}.$$

An analogous procedure applies also to dynamic light scattering experiments; however in this case the relationship between the collective diffusion coefficient D and the virial coefficient is less immediate.

In biology the interaction between biomolecules is usually quantified through the binding coefficient K_n (or the dissociation constant K) defined as the ratio between the concentration of free molecules in solution and that of dimer or larger aggregates (while $K = 1/K_n$). We determined the relationship between B_2 and K. We evaluated the sensibility of our experimental technique in determining molecular dissociation constant and we found we are able to study very weak interactions. We can detect dissociation constant between the particles $K \approx 10\,\mu M$; the sensibility on molecular dissociation constant rapidly increases by incrementing the number of links between the particles.

We first measured repulsive electrostatic interaction due to the charges present on particles surface. We coated particles with various surfactants and we examined the light diffused by the colloidal dispersions at different ionic strengths. We modified the repulsive interaction between the colloids both by incrementing the ionic strength of the dispersion and by adding to the particles surface a surfactant, the HTAB, charged of opposite sign with respect to the particles. By measuring the diffused light intensity and the diffusion coefficient we determined for each sample the value of the second virial coefficient B_2. From the value of B_2 by using the expression of the electrostatic potential, we quantified the particles charge, which results dependent on the ionic strength and on the surfactant used to coat the surface of the colloids. The charge of the particles estimated from samples where the charges have been screened through electrolyte ionic strength is found to be different from that determined by screening charges through the HTAB adsorption. This finding is in agreement with renormalization charge theory which asserts that the charges involved in the particles interactions can be different from the structural charges present on the particles surface.

We determined two different experimental conditions in which particles interact as Hard Sphere, either by screening charges through ionic strength or by adding to the dispersion a given quantity of HTAB. The determination of the Hard Sphere condition is preliminary to the study of attractive interactions since residual electric repulsion could impair the detection of other, more subtle, interactions.

We decided to use our colloidal-based detector to study carbohydrate-carbohydrate interactions. Despite they play a crucial role in many cellular processes, carbohydrate interactions are very weak and difficult to detect. We performed dynamic light scattering measurements of suspensions with particles coated with *Dodecyl-α-D-Maltoside*, whose molecules consist of an hydrophobic tail while the head is a disaccharide. We prepared samples by adding to the dispersions HTAB and electrolyte, so to make particles interact as Hard Spheres. In agreement with the literature, we found attractive interaction between carbohydrate-coated colloids when Calcium ions are present in the dispersion. We verified the specificity of the attractive interaction between carbohydrate-coated colloids by adding to the sample the $EDTA$, a chelant molecule for Calcium ions. We observed an enhancement of the diffusion coefficient indicating a redispersion of the Calcium mediated carbohydrate-carbohydrate links.

In conclusion, the first part of this thesis presents a systematic study of interactions in a particular colloidal systems which, due to its peculiar properties, allows to study by optical means aqueous colloidal dispersions at high volume fractions. In such system interactions can be easily tuned and balanced. The acquired data demonstrate that by studying the ensemble behavior of the colloidal dispersion it is possible to obtain information on the interactions between particles superficial groups. This technique could be very interesting for studying weak molecular interactions, usually difficult to detect and quantify.

The second part of this thesis reports a previously undescribed effect originating in rod-sphere and sphere-sphere mixtures of charged colloids mixture in presence of an external oscillating electric field.

The behavior of colloidal dispersions under the effect of an external electric field is strictly determined by the dielectric properties of both the colloids and the suspending medium. In particular, when the colloids are charged particles, the behavior of the dispersion strongly depends on the electric field frequency. The simplest regime can be found at high field frequencies (MHz) where hydrodynamic and diffusional effects can be neglected. In this regime charged particles with their electric double layer can be assimilated to dielectric particles with a conductive skin and the behavior of colloids in electric field is efficiently described by the well known Maxwell-Wagner model, usually applicable to conductive particles. At low field frequencies, instead, electrodynamic processes and solvent flows play a crucial role in determining the behavior of the particles. In particular perturbation of the local neutral salt concentration, known as concentration polarization, is the basic mechanism at the origin of the so called α-relaxation. The concentration polarization asymmetrically affects the electric

double layer length λ_D and charge distribution on the two side of the particle. This process has a characteristic frequency

$$\nu_\alpha \approx \frac{D}{R^2}$$

where D is the mean ionic diffusion coefficient and R is the particle size. The concentration polarization is the slowest electrokinetic effect for charged particles in electrolyte solution.

It is known from the literature that rod-like particles when exposed to an electric field orient preferentially parallel to the field direction. However Mantegazza et al., by performing birefringence measurements, observed a low frequency phenomenon of anomalous orientation occurring when charged rod-like particles are dispersed in a mixture with a sufficient concentration of smaller spherical particles charged of the same sign. In this case rods orient preferentially perpendicular to the field direction. Since the low frequency anomaly can not be due to an induced dipole-induced dipole interaction, it should be interpreted in terms of other non-trivial mechanism.

This thesis work offers a better insight into the physics of such anomalous orientation phenomenon. We have performed Electric Transmitted Light Intensity (ETLI) measurements to study the scattering cross section of the colloidal dispersions. In particular we have determined the optical turbidity τ of the colloidal dispersion under the effect of an external ac electric field. τ is related to the transmitted intensity via the extinction equation:

$$I = I_0 exp(-\tau L),$$

with I_0 incident intensity, L length of the cell and I dc component of the transmitted intensity while the field is applied. We performed measurements with light polarization parallel or perpendicular to the field direction. By evaluating the field induced turbidity variation we confirmed the observation of the low frequency anomalous orientation in rod-sphere mixture. Moreover, in the same frequency range, we found an overall field-induced clearing of the mixture. By modeling the diffuse light expected in our colloidal dispersion we demonstrated that such clearing effect is due to a structuring of the secondary particles around the rods taking place in the same frequency range as the negative orientation of the rods. The characteristic frequency of the phenomenon $\nu_{mix} \cong 5\,kHz$ is significantly lower than the expected α-relaxation frequency. The value of ν_{mix} is instead comparable with D_s/R^2, the diffusion time of the small spheres around the rods of mean size R. The hypothesis is that ν_{mix} could reflect a process analogous to the ionic concentration polarization where the small charged spheres act as coions.

To test this hypothesis and to seek a generalization of these phenomena we performed experiments

in mixture of large and small spheres. We found the same low frequency field induced clearing for both polarization at frequencies $\nu < \nu_{mix} \approx 3 - 5\,kHz$. The observation of a clearing phenomenon in spheres mixtures, where no orientational effect is possible, clearly indicates that the application of an electric field produces an interaction between large and small particles. By modeling the light diffused by the mixture through a second virial expansion of the state equation for binary colloidal dispersion, we found that a decrease of the scattered intensity can be provoked by a repulsive interaction between large an small sphere. Data also show that the clearing is larger when the light is polarized perpendicularly to the field direction, thus indicating an anisotropic interaction.

To interpret ETLI data we modeled the geometrical distribution of the small spheres around each larger sphere. Due to basic optical properties, light scattering experiments are not sensible to density variation with odd symmetry. To account for our data, we thus assumed a small spheres distribution with even symmetry, with particles concentration incremented at the poles of the larger particles along the field direction and decreased in the equatorial region. We have reproduced the measured field induced turbidity variation with appropriate values for the refractive index variation and for the spatial extension of the accumulation and depletion regions.

All the observed phenomena point to the following scenario. As the electric field is turned on small particles accumulate, by mobility mismatch, on one side of the larger rod-like or spherical particles, while depleting on the other side. This polar accumulation remains undetected by ETLI experiments because of symmetry. Such accumulation and depletion process continues until it is compensated at $\nu < \nu_{mix}$ by diffusion of the small particles across the larger ones. The described process is analogous to the concentration polarization for electrolyte ions. We conceive this "colloidal concentration polarization" as the only possible electrokinetic process having the correct frequency that could justify the onset of strong non-linear electro-osmotic flows around each large sphere. At low frequency such electrokinetic flows have the appropriate amplitude to account for the negative torque in rod-sphere mixture and for the depletion of small spheres around the larger ones.

In conclusion in this thesis we demonstrated that biomolecular recognition and electrokinetic flows generate previously undescribed interactions phenomena. This interactions constitute:

- a method to detect and quantify weak molecular interaction;
- a mean to draw attention to a new electrokinetic phenomenon.

The PhD work has regarded also the modernizing of the apparatus for Birefringence and Electric Light Scattering measurements by writing a LabVIEW program to remotely control the apparatus

instruments.

1 Colloidal dispersions

1.1 Colloidal particles

Colloidal dispersions are liquid solutions in which small scraps of different material, usually solid particles or drops of a non-mixable liquid, are suspended by Brownian motion. Nature presents many different types of colloidal dispersions: the blood, the milk, the ice-cream are only few examples of a wide variety of products ranging from food to cosmetics and paints. The definition of colloidal particles refers to particles having a radius varying from some nanometers to $500\,nm$. The lower limit comes from the requirement that the colloids are significantly larger than the molecules of the constituent material and of the suspension medium. The upper limit ensures that the particles are small enough to have a Brownian diffusion motion not dominated from gravitational force or convection effect.

The interest for colloidal dispersions arises from different areas. Historically physicists have looked at colloids as a model system to verify statistical physics predictions. In fact colloidal particles are subject to mutual interactions which can be tuned and modified and whose intensities determine the macroscopic properties of the dispersion. Hence colloidal dispersions allow to experimentally study the connection between single constituent properties and the ensemble behavior. From a more practical point of view, colloids represent a rich source of applications: cosmetics, paints, foods, bonding agents are only some examples of materials whose efficiency directly depends on the properties of the constituent colloidal dispersions. More recently colloidal systems have been studied for interesting applications in the biomedical fields. In this case, the attention is devoted more to the single particle behavior than to the ensemble properties. In fact colloids present different characteristics from their corresponding macroscopic materials: for example semiconductor nanoparticles are strongly fluorescent or ferromagnetic colloidal particles are easily magnetizable.

Colloidal particles are usually 10^3 times larger than atoms. This fact has important consequences on colloids properties and behavior. The number density ρ (number of elementary unit per unit volume) of an atomic material is about $5 \cdot 10^{22}\, cm^{-3}$, for a colloidal suspension is about $5 \cdot 10^{13}\, cm^{-3}$. It follows that, since the strength of a solid is proportional to ρ while the particle potential energy is comparable in the two cases, colloidal crystals are about 10^9 times weaker than the corresponding atomic ones. Colloidal crystal can be easily disrupted or melted, provoking fluctuation in the suspension. Defining the relaxation time τ_R as the time taken by a particle to diffuse for a distance equal to its radius

$$\tau_R \approx \frac{R^2}{D},$$

where R and D stand for the particle radius and the diffusion coefficient respectively, it results that for an atomic material $\tau_R \approx 10^{-11}\, s$ while for colloids one is about $10^{-2}\, s$. This means that colloidal crystals have well-defined metastable (non-equilibrium) states, having lifetimes long enough to allow experimental study.

The scattering of radiation constitutes an important technique for the experimental study of colloidal system; light is the most used type of electromagnetic radiation, since its wavelength matches the range of colloidal extensions. In chapter 2 some experimental techniques involving light scattering will be described, with particular emphasis on the physical quantities that can be estimated with such measurements techniques.

The properties of colloidal dispersion strongly depend on the mutual interactions between the particles. Interactions can be attractive, such as Van der Waals force, or repulsive, as the electrostatic force. Colloidal dispersions are stable only when the repulsive forces are stronger than the attractive ones. In the next section a brief description of the interparticles colloidal interactions will be given. It's worthwhile noticing that the behavior of colloidal system is also affected by the solvent-particle structural properties, i.e. the electric charge, the dielectric constants of the materials.

1.2 Colloidal interactions

1.2.1 Hard sphere potential

Hard sphere potential describes the easiest possible interaction among colloidal particles. Colloidal particles are considered as impenetrable sphere, so that the resulting potential is an infinitely repulsive

barrier placed at a a distance $2R$, with R particles radius:

$$V(x) = \begin{cases} \infty & x < 2R \\ 0 & x > 2R. \end{cases} \tag{1.1}$$

The excluded volume of a sphere with radius R is $V_{ex} = \frac{2}{3}\pi(2R)^2$, namely 4 times the particle volume.

1.2.2 Van der Waals attraction

Two bodies are attracted by a force caused by the interaction between the fluctuating electromagnetic fields associated with their polarizabilities. This force is known as Van der Waals force. The attraction between two atoms at a distance r is proportional to r^{-6} (Lennard-Jones potential) while the interaction between two particles of radius R is given by:

$$V_A(r) = -\frac{A}{6}\left[\frac{2R^2}{r^2 - 4R^2} + \frac{2R^2}{r^2} + ln\left(1 - \frac{4R^2}{r^2}\right)\right], \tag{1.2}$$

where r is the distance between the particles centers. The Hamaker constant A is determined by both colloids and solvent properties, in particular their frequency-dependent polarizabilities. $A = 0$ in case of particles and dispersing medium having the same polarizabilities. Van der Waals force creates a potential minimum near $r = 2R$, which can be greater then the thermal energy k_BT (see Figure 1.1). Not stabilized suspended particles aggregate irreversibly under the effect of this force. It's therefore necessary to stabilize the colloidal dispersions, two approaches are commonly used: charge stabilization and steric stabilization.

1.3 Stabilization

1.3.1 Charge stabilization

Charged particles can be considered as "macroions": the ionisable groups on their surfaces dissociate when the particles are immersed in polar liquid such as water, giving rise to a net charge typically of the order of $10^2 - 10^5$ elementary charges e. The counterions leaving the surface move away from the macroion with Brownian motion, although they remain in its field of force. An electrical double layer, composed by the discharged counterions and by the ions of the electrolyte present in the suspension, is generated in proximity of the charged colloids. When two macroions approach each other, the overlap of the respective double layer prevents the particles aggregation, due to the double

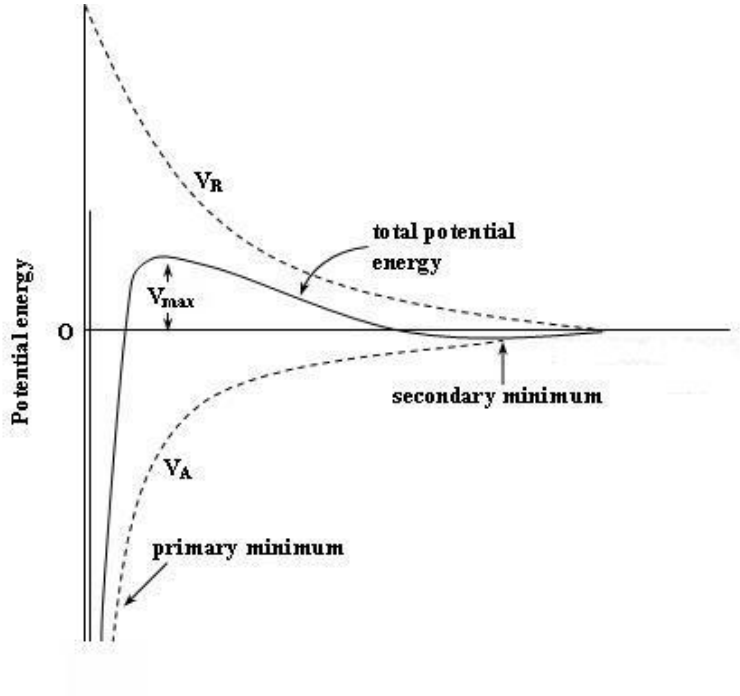

Figure 1.1: DLVO potential as a function of the particles interdistance.

layer repulsive force. Hence colloidal dispersions of charged particle are stable.

The first detailed treatment of the electric double layer have been proposed by Verwey and Overbeek [1]. This treatment describes the average spatial distribution of the ions in the macroions potential fields at the equilibrium with a Boltzmann distribution. This is done by regarding the ions in the suspension as point charge moving of Brownian motion and having high enough velocities. Poisson equation is then used to calculate the interaction potential. The resulting Poisson-Boltzmann equation is linearized. The simplest (but approximate) expression for the effective interaction potential between two charged colloids is the so called Yukawa potential:

$$V_R(r) = \begin{cases} \infty & r < 2R \\ \frac{q_e^2}{\epsilon r} e^{-\kappa_e r} & r > 2R, \end{cases} \tag{1.3}$$

where q_e is the effective macroions charge, ϵ is the solvent dielectric constant and κ_e is the Debye screening parameter, that in the case of a symmetric electrolyte assumes the form:

$$\kappa_e = \kappa = \frac{4\pi}{\epsilon k_B T} \sum_j \rho_j q_j^2, \tag{1.4}$$

with ρ_j and q_j number density and charge of the j ions respectively. The quantity κ^{-1} has the dimension of a length and is called Debye screening length. From Equation 1.4 it is evident that the

electrolyte concentration strongly affect the Debye length and thus the interaction potential.

Derjaguin, Landau, Verwey and Overbeek developed a theory to consider both the Van der Waals force and the electrostatic repulsive interaction. According to their model the total pair potential $V(r)$ (DLVO potential) is given by the sum of the Coulombic repulsion $V_R(r)$ (Equation 1.3) and of the attractive force $V_A(r)$ (Equation 1.2) and has the form sketched in Figure 1.1. For $r \approx 2R$ the attraction dominates and $V(r)$ has a primary minimum. The repulsive interaction dominates for larger r, except in the case of weakly charged particles and of high electrolyte concentration. Hence there is a maximum in the potential trend, which, to ensure dispersion stability, must be greater than thermal energy. Since Van der Waals attraction decays as r^{-6} while the repulsive force has an exponential decay, the total potential $V(r)$ presents a secondary minimum for larger value of r. In conclusion, a colloidal dispersion is stable if there is a negligible probability that the separation between two particle is smaller than the position of the maximum in $V(r)$.

1.3.2 Steric stabilization

Steric stabilization method consists in coating the colloidal particle surface with layers of polymer. Many different types of polymer can be used for this purpose, ranging from short chains to more complex structures. Coating can be achieved through physical adsorption or through chemical bonding of particles and polymers. Due to the great variety of systems obtained by varying particles, solvent or polymer chains, it's not possible to give a theory of steric stabilization which has the same generality as that of charge stabilization. In this context we can just describe the origin of the repulsive force between polymer coated colloids.

When two coated particles in Brownian motion approach each other, the polymer chains can only partially compress and interpenetrate. Hence a repulsive force between the particles originates. Differently form electrostatic stabilization the repulsive force is not influenced by the electrolyte concentration. It's worthwhile noticing that steric stabilization is effective also at high colloidal concentrations, while charge stabilization is more efficient at low concentrations.

To better describe the process of steric stabilization, it's necessary to investigate how polymer in solution interact with the solvent medium. Indeed the polymeric chain conformation is strongly affected by the interaction of each chain segment with the liquid molecules. In a "good solvent" polymer chains tend to maximize the polymer-solvent contacts, and thus the chains will be elongated. On contrary, in "bad solvent", the polymer chains assume a contract conformation; nevertheless in this case the excluded volume interaction between chain monomers become non negligible. In particular, if the two effects are balanced the solvent is called $\theta-$solvent. It has been shown by Flory that the

polymer mean dimension can be written as the mean quadratic distance between the start and the end of the chains and the following relation is valid:

$$\left\langle r^2 \right\rangle^{1/2} \propto n^{\nu},$$

where n is the number of total monomers and ν is a variable parameter (for a good solvent $n = 0.588$). The solvency of a liquid is influenced by the temperature so that a solvent can become a good or a bad solvent by modifying its temperature.

Polymer-solvent interactions play a crucial role also when polymer chains are adsorbed on colloids surfaces and also in this case the polymer-polymer interaction is influenced by the temperature. At the $\theta-$point there is no interaction, while in other conditions the interaction can be both attractive or repulsive. In a good solvent, if Van der Waals attraction can be neglected, the effective pair potential between colloids can be approximated with an hard sphere potential, as described in subsection 1.2.1. In this case the radius to be considered to calculate the excluded volume is the sum of the particle radius and of the coating thickness, also if in many condition the polymer dimensions are negligible with respect to particle ones. When polymer can attract each other, the effective colloidal potential will contain, in addition to the hard core steric repulsion, a narrow attractive well. This situation is described through a Sticky Hard Spheres model, which will be analytically presented in the following chapters.

1.4 New colloidal interactions

A proper characteristic of colloidal dispersion is the high surface-to-volume ratio; this fact together, with the small dimension of colloidal particles, make surface phenomena determining factors for the physical behavior of these systems. Moreover, colloidal suspensions allow to easily vary the conditions into which interactions are analyzed: for example, to modify the intensity of the repulsive interaction between charged particles it is enough to change the electrolyte concentration in the solution. During the past few years many interesting phenomena involving colloidal particles dispersions have been discovered and reported. In particular, we devoted our attention to two different classes of colloidal interaction phenomena.

1.4.1 Biomolecular mediated interactions

In recent years many papers have been published linking biology to colloidal science. In particular two major research approach can be identified.

On one side controlling and tuning interactions between particles has always been a relevant challenge both experimentally and theoretically. It's worthwhile mentioning a work of Valignat et al. *Reversible self-assembly and directed assembly of DNA-linked micrometer-sized colloids*[2]. They prepared DNA-functionalized polystyrene microbead binary mixtures by conjugating two types (green and red) of fluorescent NeutrAvidin-coated particles with biotin-modified DNA. Various polymers, differing for the chain-length, were also added to the solution to prevent particles collapse, since polymer brush imparts steric repulsion between the particles and limits the number of available linkers between them. The particles had a diameter $d = 1$ μm. A first DNA sequence, called G-type, was attached to green-particles surface while another type, called R-type, was attached to red-particles surface. G-type and R-type DNA sequences were 61-base oligonucleotides: 50 bases are in common to both the DNA's and are hybridized to form a spacer. The 11-end bases of G-type sequence are complementary to the 11-end bases of the R-type sequence, thus acting as "sticky tail". G-type and R-type microbeads are shown in Figure 1.2.

Figure 1.2: G-type and R-type microbeads (radius $R_0 = 0.5$ μm) stabilized through a polymer which forms a layer of thickness h on the particles surface. Part of the DNA sticky ends is hidden inside this layer [2].

In standard experiments R-type and G-type beads were mixed in equal parts and observed by optical fluorescence microscopy. At room temperature with four copolymers as stabilizers a rapid formation of clusters was observed and after few hours aggregation was almost complete. In Figure 1.3 a detailed study of the number of singlet breads fraction as a function of the temperature for different stabilizers is reported. It shows the reversibility of the aggregation process and a strong dependence of the melting temperature T_m^b on the type of stabilizer, where the melting temperature is defined as the temperature at which half of the beads are unbound. In particular T_m^b increases as the mass of the copolymer decreases, according to the fact that larger polymer spacers keep the particles further apart

thus reducing the number of DNA links.

Valignat et al. proposed also a comparison between the melting temperature of the DNA- functionalized beads and the melting temperature T_m^s of the free DNA in solution, i.e. the temperature at which half strands are random coil and half form double helixes. T_m^s can be calculated through nearest-

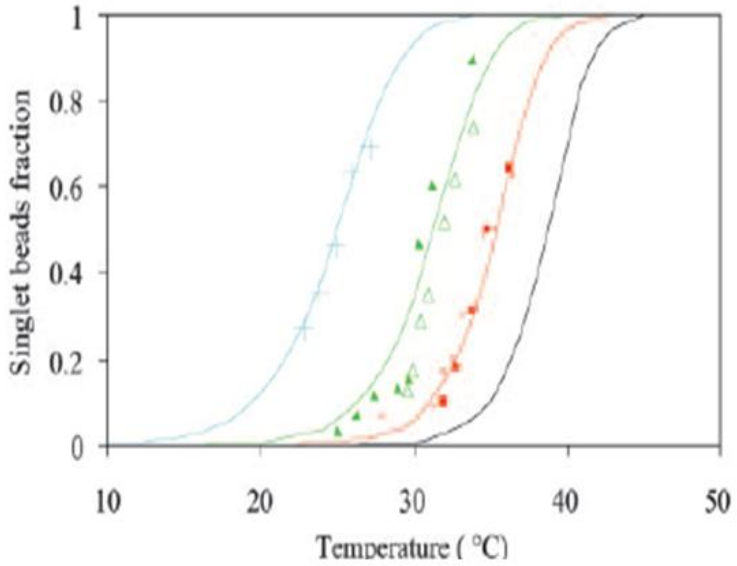

Figure 1.3: Fraction of single unbound beads vs. temperature. Discrete marks are experimental point obtained with different stabilizers while solids lines are the best fits [2].

neighbor thermodynamics and results of the same magnitude order of T_m^b. However both the difference between T_m^s and T_m^b and the strong dependence of the melting temperature on the stabilizers length, bring to the conclusion that adsorbing copolymers on microbrads drastically changes the melting behavior of the DNA-functionalized particles.

Valignat et al. proposed also a geometric estimation of the available DNA links N_s between two coated beads (see also Figure 1.2):

$$N_s = \frac{2\pi R_0}{L}(L-h)^2\Gamma, \tag{1.5}$$

where Γ is the particle surface density of strands.

Another approach to the "biology combined with colloidal science" research current consists in using colloidal particles as mediators and amplifiers for the study of biological interactions. The difference between the two approaches is that, in the first one biology is at service of colloidal science to improve colloidal potentiality, while in the second case colloids are exploited to get better knowledge

of some biological interactions.

Baksh et al. [3] proposed a study of membrane-membrane interactions which employs colloidal phase transition of membrane-coated silica beads (see Figure 1.4). Membrane-derivatized silica beads were dispersed, underwater, where they settle gravitationally onto the underlying substrate forming a two-dimensional colloid. As highlighted in section 1.1 the behavior of a colloidal system depends on the pair potential interaction between suspended particles; for membrane-coated silica beads the potential is dominated by the membrane-membrane interactions. The chemical composition of the membrane was adjusted to modulate pair interaction potential to give rise to condensed phase. Thus, the effects of protein binding to membrane-associated ligands were expected to produce significant change in colloidal phase. It was found that in all cases proteins binding triggers a condensed-to-

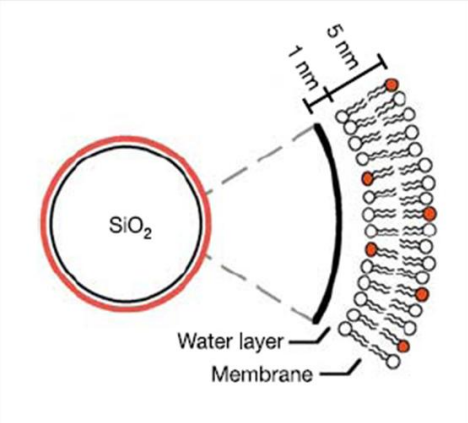

Figure 1.4: Schematic illustration of the membrane-derivatized silica beads [3].

disperse colloidal phase transition. A quantitative analysis of the phenomenon was performed by extracting the pair distribution function $g(r)$ (see Figure 1.5).

In literature have been also reported a series of study on carbohydrate molecules performed by using gold nano-particles as substrate [4, 5, 6, 7]. Carbohydrates are a class of molecules that, although very weakly interacting, are fundamental in life: they play a crucial role in cellular transport and recognition phenomena. Their micro-domains are functional units associated with cell adhesion, signal transduction and other normal and pathological processes. Characteristic features for carbohydrates interaction are its strong dependency on divalent cations and its extremely low affinity, which is compensated in nature by polyvalent presentation of the ligands: while the single molecule interaction is weak, usually carbohydrates interaction involves a molecular ensemble, so that the resulting interaction is much more intense. However these features make the study of such interaction a real challenge.

Colloidal particles coated with carbohydrate molecules are very similar to real biological system, and

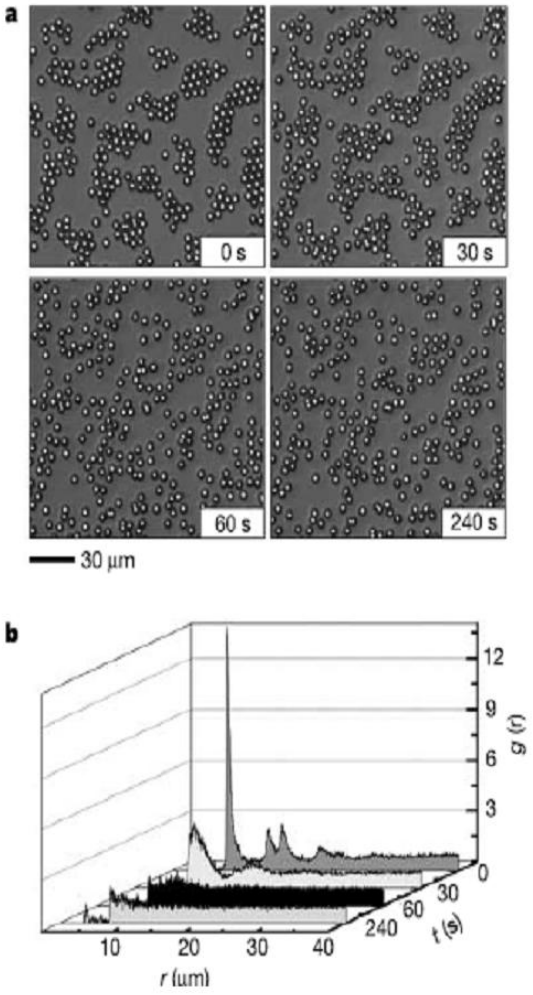

Figure 1.5: Protein-binding-triggered colloidal phase transition. **a** Time sequence of images of the condensed-to-dispersed colloidal phase transition, triggered by protein addition. **b** Corresponding plot of g(r) [3].

allow to study and quantify the carbohydrate interactions. In [4, 5] carbohydrate molecules have been modified to have a lipid tail and a glycol-head (glycosphingolipid), in order to adhere to gold particles of spherical shape with radius of $3\,nm$. The principal experimental technique used in these works is the Surface Plasmon Resonance. A schematic representation of the studied systems is shown in Figure 1.6: gold surfaces have been coated with glycolipid. It has been studied the interaction between these functionalied surfaces and gold nanoparticles covered with the same carbohydrate. It has been

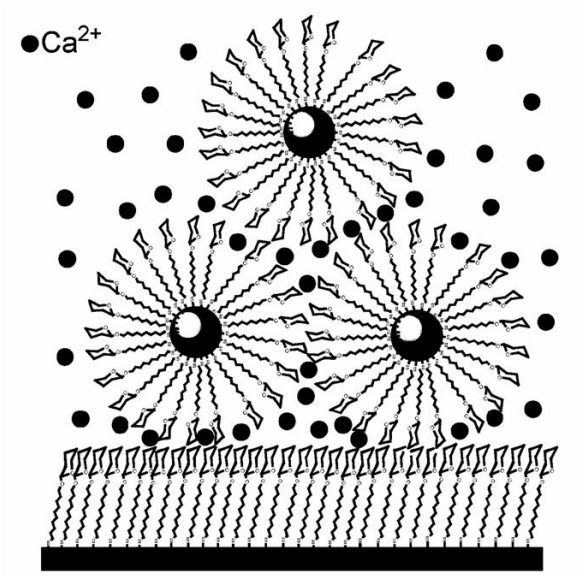

Figure 1.6: Schematic representation of the binding structure used to study carbohydrate-carbohydrate interactions in [4].

observed that the carbohydrate-carbohydrate interaction is active only when Ca_{2+} ions are dissolved in solution, according to the well known fact that carbohydrate interactions strongly depends on the presence of divalent ions.

In the cited paper the principally studied carbohydrate are the LewisX and the Lactose. The first one presents a slow association phase and a gradual dissociation phase; the binding has a high affinity and a dissociation constant $K = 5.4 \times 10^{-7}\,M$. The measured dissociation constant for the Lactose-Lactose binding is $K = 1.4 \times 10^{-5}\,M$, two magnitude order inferior to the LewisX one. Thus the Lactose interaction is much weaker. A common characteristic to all cited papers is that the collapse of the colloidal system is employed to study and quantify biomolecular interaction.

We employed light scattering technique to study and quantify carbohydrate-carbohydrate interactions. According to [8], low-refractive-index nanoparticles can be used to detect molecular interaction and quantify the dissociation constant of the binding. This methods allows the study of interactions in a low intensity regime, because it does not need colloidal particles collapse.

1.4.2 Electric field induced electrokinetic interactions

In the second part of this PhD thesis our attention has been devoted to a particular effect originating in colloidal suspension under the effect of an external oscillating electric field.

The first observation of electokinetic phenomena date back to 1809, when Reuss observed that clay particles dispersed in water migrate under the effect of an electric field [9]. Electrokinetic phenomena are characterized by tangential motion of liquid referred to an adjacent charged surface and involve the interaction between ionic screen clouds, applied electric fields and hydrodynamic flows. They play a significant role in colloidal and interface science [10, 11, 12], not only as a tool for surface characterization but also for their many practical applications for example in analytical chemistry, separation science and electrochemistry. The most important electrokinetic phenomena are:

- *Electrophoresis*: refers to the relative movement of particle with respects to a stationary liquid under the influence of an external electric field.
- *Electroosmosis*: in an electrolyte solution the liquid in proximity of a charged surface is dragged under the influence of an external electric field (see section 5.4 for a detailed description).
- *Streaming potential*: a potential difference originates when an electrolyte is forced to flow past a charged surface.
- *Sedimentation potential*: a potential difference originates when charged particles sediment in a liquid.

Electrokinetic phenomena are typically second order phenomena, where forces of a certain kind create fluxes or flows of another type. The basic mechanism which regulates electrokinetics is as follows: when a charged surface is immersed in an electrolyte, a ionic screening cloud (double layer) forms in proximity of the surface. In most situations the double layer is thin compared to the other system dimensions. If an electric field is applied, the ions in the screening cloud experience a force which gives rise to a fluid flow whose velocity approaches the stationary Smoluchowski value just outside the charged double layer:

$$u = -\frac{\epsilon\zeta}{\eta} E_{\parallel}, \tag{1.6}$$

where ϵ and η are the solvent dielectric constant and viscosity respectively, $E_{\parallel}$ is the component of the electric filed tangential to the surface and ζ is the so called "zeta potential", the potential drop across the double layer.

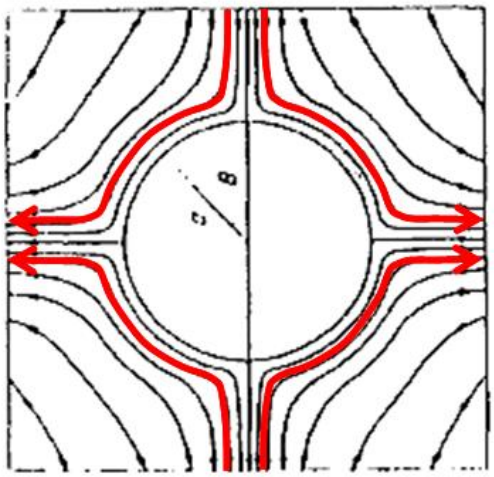

Figure 1.7: Pattern of distribution of nonlinear flows near a polarized particle.

The simplest theory to study electrokinetic phenomena is the Standard Electrokinetic Model (SEM) [10, 11]: only linear electrokinetic effects are considered and quantities like particle mobility, ionic current, particle polarization are modeled through a set of linearized $O(E)$ equations. One of the basics approximation assumed in SEM is that the zeta potential ζ is considered an equilibrium quantity, and thus taken to be constant.

However, in many cases, the combination of electric and dynamic effects give rise to non-trivial interaction phenomena. As reviewed by Squires and Bazant [13], during last decades many interesting and counter-intuitive effects have been experimentally discovered and theoretically predicted. We consider some pioneering theoretical work of the Ukrainian school [14, 15]. Murtsovkin was the first to predict that, under certain conditions, nonlinear solvent flows appear near disperse particles polarized by an external electric field. In particular, in [15], he considers the case of dielectric or infinitely polarizable spherical particles under the action of an alternating electric field and demonstrates that in both cases nonlinears flows originate near polarized particles having the distribution pattern sketched in Figure 1.7.

In recent years a renewed interest toward electrokinetic phenomena have been documented, thanks also to the growing interest for microfluidic application where electrokinetics plays a crucial role. Squires and Bazant published a series of work [13, 16] on induced-charged electro-osmosis (ICEO) at polarizable surfaces, a physical process discovered independently by Ramos et al. [17] in experiment and by Ajdari [18] in theoretical calculations similar to that predicted by Murtsovkin for metal particles. The basic mechanism is as follows: consider a ideally polarizable conducting body in an

electrolyte subject to an electric field. Initially the field lines intersect the particle surface at right angle to satisfy boundary conditions. However, the field drives current of ions in the electrolyte, which cannot penetrate the solid/liquid interface. At low frequencies, ions accumulate and this charge cloud expels field lines, until none intersects the particle surface. The induced charge is dipolar, giving rise to quadrupolar ICEO flow (see Figure 1.8), similar to the one depicted in Figure 1.7. In this context, Ajdari [18] first predicted that an asymmetric array of electrodes, subject to AC forcing at particular frequency, could function as a microfluidic pump as many groups later demonstrated experimentally [19, 20, 21].

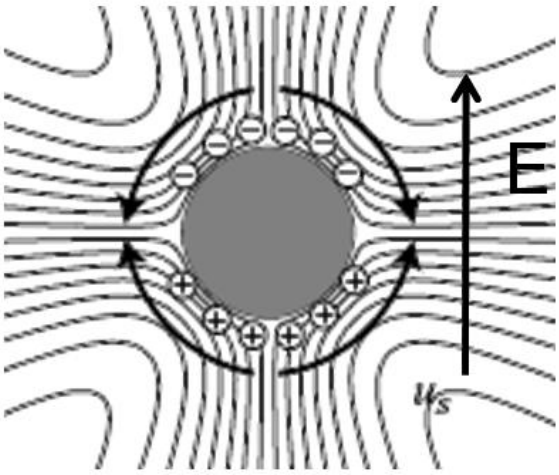

Figure 1.8: Electro-osmotic flow around a conducting cylinder with zero net charge.

Another surprising phenomena involving electric field effect on colloidal solution is reported by Grier [22]. He performed experiments with aqueous suspension of monodisperse colloidal silica spheres with diameter $d = 3\,\mu m$ confined between two parallel metal coated glass surfaces which allow to apply an external electric field to the solution. For biases below $2.4\,V$ the ions in solution screen out the electric field. For higher biases, the spheres levitates into clusters: each cluster is composed by a toroidal vortex in which spheres move upwards outside and downwards inside the vortex (see Figure 1.9). The origin of this phenomenon is a combined action of electrokinetic and gravitational forces.

All the cited works document the great variety and complexity of electrokinetics phenomena.

The second part of the thesis work investigates an intriguing phenomenon firstly observed by Mantegazza et al. [23]. They studied binary mixture of charged rod-like particles immersed in a sea of smaller spherical particles charged of the same sign, noticing the occurrence of an anomalous birefringence signal, which corresponds to an anomalous field-induced particles orientation. In absence of secondary particles, as explained in chapter 5, rod-like particles align parallel to the electric

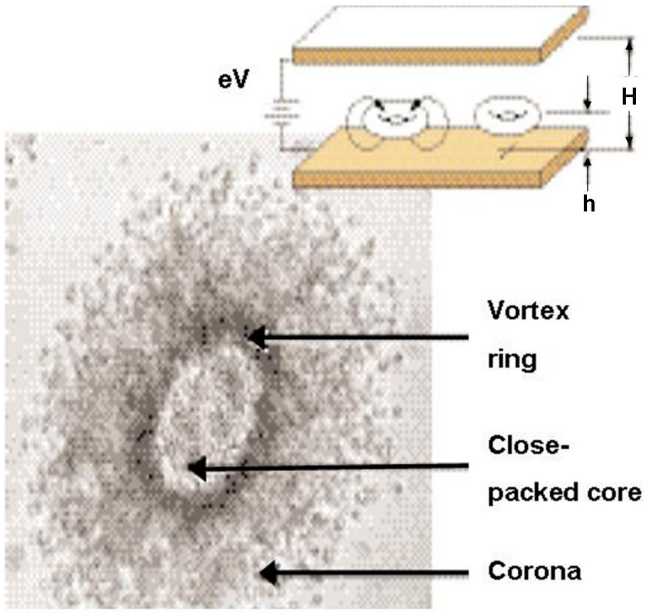

Figure 1.9: Colloidal vortex rings structure. The inset shows the experimental geometry, with parallel metal coated glass surfaces applying a constant vertical bias to a confined suspension.

field direction. When rod-like particles are immersed in a dispersion of small spheres, the rods align perpendicularly to the external field. The exploration of many different dispersions indicate that this anomalous behavior is a universal feature of the electric response of mixture of charged rod and spheres. In [23] a quantitative analysis of the phenomenon is performed; however the physical processes governing this behavior are still unknown. This thesis work attempts to acquire better insight into the physics of these systems, taking advantage of the theoretical ICEO model.

2 Experimental techniques and materials

When a material is exposed to a light beam, the incident electromagnetic field exerts a force on the charges of the medium. As a consequence charges are accelerated and radiate light. In a region of the material smaller than the cube light wavelength, all the atoms experience basically the same electric field. Considering many subregions, the scattered electric field is obtained by the superposition of the field scattered from each subregion. If the medium is uniform, namely the dielectric constant is the same in each subregion, the waves diffused by each subregion have the same amplitude but differ for a phase factor depending on the relative spatial position of the subregions. Thus scattered waves interfere constructively only in the forward direction. If the dielectric constant is not uniform, the radiated waves are no more identical in amplitude and scattering take place in directions other than the forward one. According to this view, light scattering is due to dielectric constant fluctuations inside the illuminated volume.

Light scattering is a versatile and non-invasive method to study diffusive systems. Many different experimental techniques employ the scattering of light as basic physical mechanism to detect properties of the considered medium. We present some of these techniques with particular emphasis on the physical mechanisms exploited by the measurements and on the physical quantities they allow to study.

2.1 Static Light Scattering

In a scattering experiment a beam of plane wave monochromatic light is incident on a scattering medium and the diffused intensity is measured at various angles. Indicating with $\boldsymbol{k}_0$ and $\boldsymbol{k}$ the wave

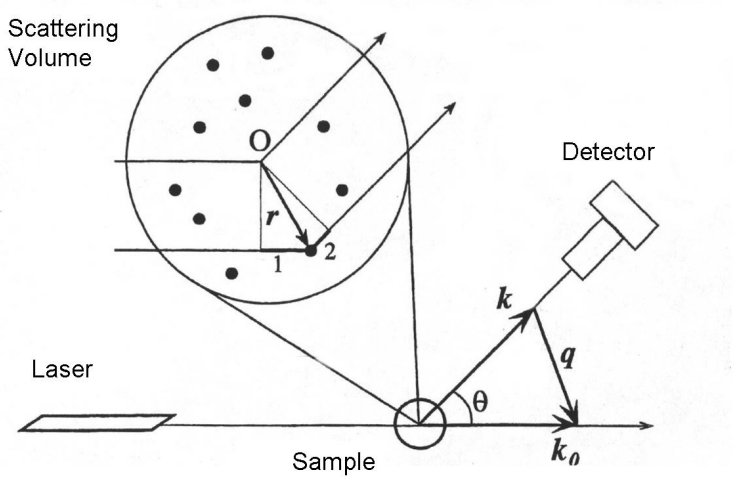

Figure 2.1: Scattering vector.

vector of the incident and diffused wave respectively, the difference vector $\boldsymbol{q} = \boldsymbol{k}_0 - \boldsymbol{k}$ is called scattering vector (see Figure 2.1). In the case of elastic scattering $|\boldsymbol{k}_0|=|\boldsymbol{k}|$ so that the amplitude of the scattering vector results:

$$q = |\boldsymbol{q}| = \frac{4\pi n}{\lambda} sin(\frac{\theta}{2}), \tag{2.1}$$

with n refractive index of the medium, λ wavelength of the incident beam and θ scattering angle.

In the most general case, the intensity diffused by particles of arbitrary form and dimension can be calculated by solving Maxwell equation with particular boundary conditions (Mie theory). However, due to the complexity of such calculations, some approximations can be assumed to simplify the treatment.

The most used approximations are the Rayleigh and the Rayleigh-Gans approximations. The first applies to particles smaller than the light wavelength λ and with generic refractive index n_p. The particles act as punctiform dipoles that oscillate at the same frequency of the incident field. The Rayleigh-Gans approximation is applicable to particles with larger dimensions than the light wavelength and relative refractive index approximately equal to one, that means

$$m \equiv \frac{n_p}{n_s} \approx 1, \tag{2.2}$$

where n_s is the solvent refractive index. Within the Rayleigh-Gans approximation, the treatment of light diffusion is performed by dividing the particles volume into elementary volumes each satisfying Rayleigh approximation hypothesis. The contributions of all elementary volumes are summed.

The Rayleigh model expresses the intensity I diffused at a distance r from spherical particles in the case of light polarized perpendicularly to the scattering plane:

$$I \cong \frac{I_0 R^6 k^4}{r^2} \left(\frac{m^2 - 1}{m^2 + 2} \right), \tag{2.3}$$

where R is the particles radius, k the incident wavevector amplitude and m is defined as in Equation 2.2. If the observation point is not on the scattering plane Equation 2.3 is modified to include the dependence on the azimuthal angle ϕ (see Figure 2.2):

$$I \cong \frac{I_0 R^6 k^4}{r^2} \left(\frac{m^2 - 1}{m^2 + 2} \right) sin^2 \phi. \tag{2.4}$$

Our measurements are performed at $\phi = 90°$. Equation 2.3 and Equation 2.4 have a $1/r^2$ dependence,

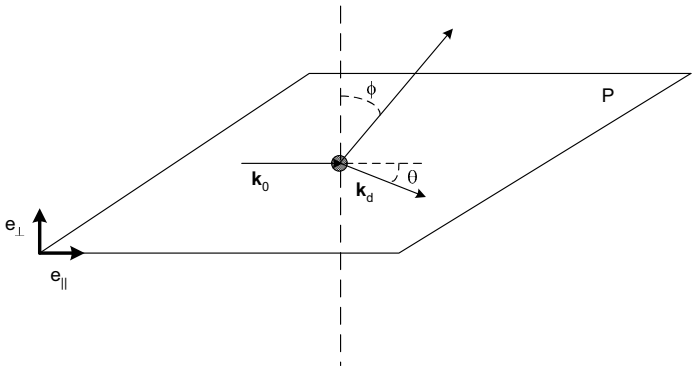

Figure 2.2: Scattering plane.

where r is the distance between the particle and the detector. This dependence assures that the total scattered power across a spherical surface centered on the scattering volume does not depend on r. The k^4 factor embodies the dependence on the radiation employed: i.e. a blue light ($\lambda = 450\,nm$) compared to a red light ($\lambda = 670\,nm$) produces an increment of the scattered intensity proportional to $(\frac{670}{450})^4 \cong 5$. It worthwhile noticing that the diffused intensity depends on the square of the scattering volume, namely for spherical particles on the sixth power of the radius.

The Rayleigh-Gans approximation is valid when the following conditions are satisfied:

$$\begin{aligned} |m - 1| &<< 1 \\ 2kR\,|m - 1| &<< 1 \end{aligned} \tag{2.5}$$

The fundamental hypothesis for this approximation are shown in Figure 2.3.

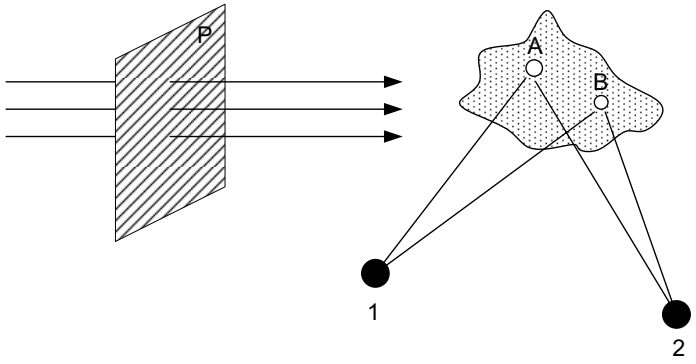

Figure 2.3: The volume of a particle satisfying Rayleigh-Gans approximation conditions can be decomposed into elementary volumes (i.e. A and B) which radiate as Rayleigh dipoles. The total diffused intensity is found by summing the contributions from all the elementary volumes.

The particle volume can be subdivided into elementary volumes (A and B in the figure): each volume is a source of diffused waves which interfere causing a total diffused intensity in each spatial direction. Equation 2.5 assures that there is a negligible phase lag between the elementary volumes. The Rayleigh-Gans approximation can be applied also to particles with dimensions greater than the light wavelength if their refractive index is similar to the solvent one.

Considering polarized radiation, the scattering amplitude diffused by each elementary volume v is given by:

$$dA(\theta) = i\left(\frac{3}{4\pi}\right)\frac{k^3}{2}(m-1)e^{i\delta}dv$$

The exponential term includes a dependence on the observation angle θ, which is not present for non-interacting Rayleigh scatterers. It is easy to show that $\delta = \boldsymbol{q}\cdot\boldsymbol{r}$, where $|\boldsymbol{r}|$ is the distance between the scattering elementary volume and $|\boldsymbol{q}| = \frac{4\pi}{\lambda}sin(\frac{\theta}{2})$ is the scattering vector (see Figure 2.4).

The total diffused intensity is calculated through the integral of the contributions coming from the elementary volume on the total particle volume V:

$$A(q) = \left(\frac{i}{2\pi}\right)k^3(m-1)\int_V e^{i\boldsymbol{q}\cdot\boldsymbol{r}}d^3r.$$

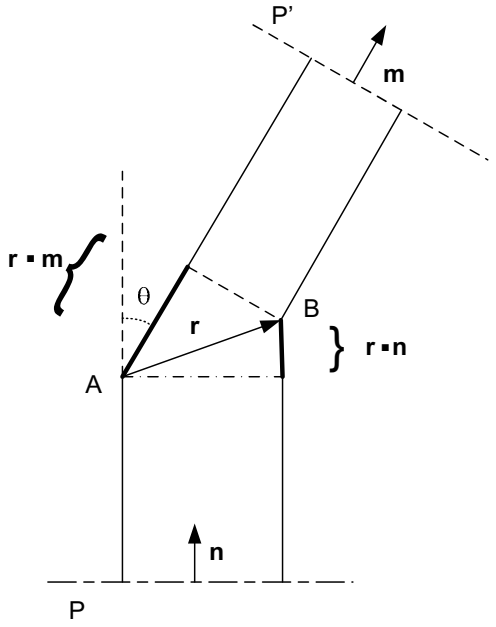

Figure 2.4: Geometric construction of the phase difference between to diffused waves coming from two points A and B of the same particle. The difference between path PAP' and the path PBP' is given by $dr = \boldsymbol{r} \cdot (\boldsymbol{m} - \boldsymbol{n})$, where $\boldsymbol{n}$ and $\boldsymbol{m}$ are the unit vector pointing in the direction of the incident and the diffused field. Hence $\delta = r(\frac{2\pi}{\lambda})sin(\frac{\theta}{2}) = \boldsymbol{r} \cdot \boldsymbol{q}$.

The total scattered intensity is given by:

$$I(q) = \frac{I_0}{k^2 r^2} |A(q)|^2 = I_0 \frac{k^4 v^2}{4\pi^2 r^2} (m-1)^2 P(q),$$

where P(q) is defined as:

$$P(q) = \frac{1}{v^2} \left| \int_V e^{i\boldsymbol{q}\cdot\boldsymbol{r}} d^3 r \right|^2 = |F(q)|^2 . \tag{2.6}$$

$F(q)$ is the particle form factor. For particles with simple geometry it can be calculated as an integral on the particle volume. In the case of spherical particles $F(q)$ assumes the value:

$$F(q) = \frac{3}{(qR)^3}(sin(qR) - qRcos(qR)) = \left(\frac{9\pi}{2(qR)^3}\right)^{1/2} J_{3/2}(qR) \tag{2.7}$$

where $J_{3/2}$ is the Bessel function of order $3/2$.

Correlated particles

When the scattering volume contains spatially correlated particles, the scattered intensity must include a term S(q), called structure factor, that accounts for the spatial correlation between fields diffused by different particles. It is possible to show that the intensity diffused by a volume V containing N particles satisfying the Rayleigh-Gans approximation requirements is:

$$I(q) = \left\langle \left| \sum_j A_j(q) e^{i\boldsymbol{q}\cdot\boldsymbol{r}_j} \right|^2 \right\rangle ,$$

where the parenthesis $\langle\rangle$ indicate that a temporal mean is performed due to the particles motion inside the scattering volume while $A_j(q)$ is the field diffused by the j particle located at a position r_j. By replacing the square modulus with the product between the summation argument and its complex conjugate

$$I(q) = \left\langle \sum_{i,j} A_j(q) A_i(q) e^{i\boldsymbol{q}\cdot(\boldsymbol{r}_j - \boldsymbol{r}_i)} \right\rangle ,$$

the diffused intensity can be written as:

$$I(q) = N |A(0)|^2 P(q) \left\langle \int d^3 r \sum_{i,j} e^{i\boldsymbol{q}\cdot\boldsymbol{r}} \delta(\boldsymbol{r} + \boldsymbol{r}_j - \boldsymbol{r}_i) \right\rangle , \tag{2.8}$$

where monodisperse particles have been considered ($A_i(q) = A_j(q)$) and the factor $P(q) = \left(\frac{A(q)}{A(0)}\right)^2$ can be calculated through Equation 6.8. Since the only term depending on time is the δ term Equa-

tion 2.8 can be rewritten as:

$$I(q) = N\left|A(0)\right|^2 P(q) \int d^3 r e^{i\boldsymbol{q}\cdot\boldsymbol{r}} \left\langle \sum_{i,j} \delta(\boldsymbol{r} + \boldsymbol{r}_j - \boldsymbol{r}_i) \right\rangle$$

The scattered intensity is proportional to the Fourier transform of the quantity

$$\left\langle \sum_{i,j} \delta(\boldsymbol{r} + \boldsymbol{r}_j - \boldsymbol{r}_i) \right\rangle,$$

which can be decomposed into two contribution:

$$\left\langle \sum_{i,j} \delta(\boldsymbol{r} + \boldsymbol{r}_j - \boldsymbol{r}_i) \right\rangle = \left\langle \sum_{i\neq,j} \delta(\boldsymbol{r} + \boldsymbol{r}_j - \boldsymbol{r}_i) \right\rangle + N\delta(r)$$

In particular

$$\frac{1}{N} \left\langle \sum_{i\neq,j} \delta(\boldsymbol{r} + \boldsymbol{r}_j - \boldsymbol{r}_i) \right\rangle = \rho g(r)$$

where $\rho = N/V$ is the number density while $g(r)$ is the pair correlation function.

Accordingly a new function, the structure factor $S(q)$ can be defined as:

$$S(q) = 1 + \rho \int e^{i\boldsymbol{q}\cdot\boldsymbol{r}} g(r) d^3 r. \tag{2.9}$$

Finally the intensity diffused by a solution containing N particles results:

$$I(q) = N\left|A(0)\right|^2 P(q) S(q) \tag{2.10}$$

where

$$|A(0)|^2 = I_0 \frac{k^4 v^2}{4\pi^2 r^2} (m-1)^2. \tag{2.11}$$

The former calculations show that the scattered intensity is related through a Fourier transform to the correlation density inside the scattering volume. It's worthwhile noticing that the structure factor can also be interpreted as the ratio between the intensity scattered by the interacting system and the one scattered by the same system in absence of interactions.

2.1.1 Static Light Scattering experimental setup

The Static Light Scattering experimental setup, shown in Figure 2.5, is composed by a laser source (A), some optical components (B), an injector (C), a temperature controlled cell holder (D), a photo-

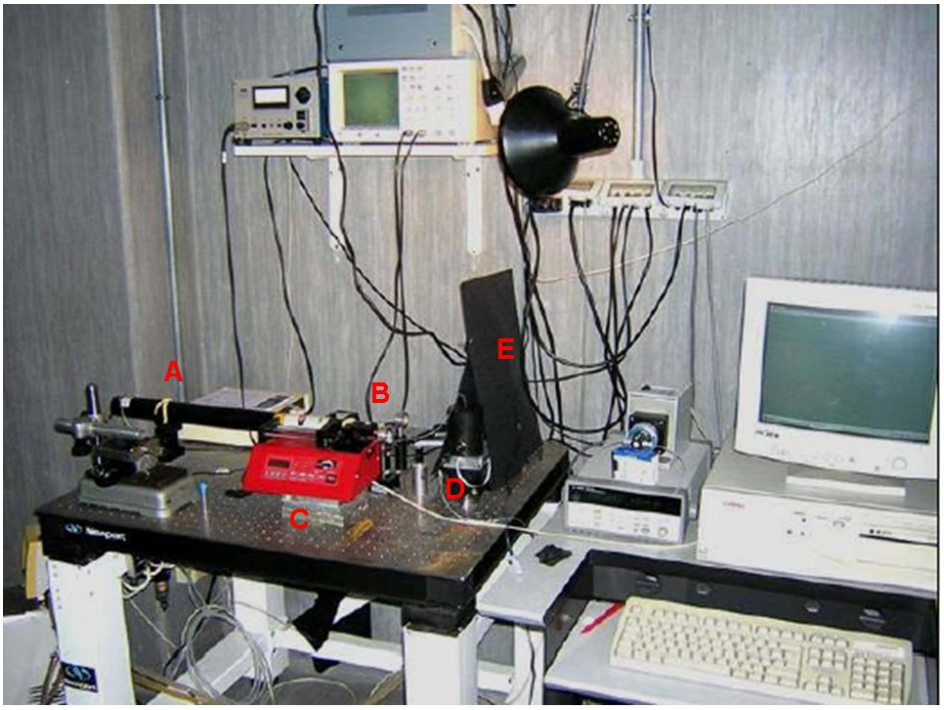

Figure 2.5: Static Scattering experimental setup: the letters highlight the main parts of the apparatus.

tube (E) and a PC for the data analysis.

Laser source and optical components

The optical source is a He-Ne laser (LGK 7665P, Lasos) with wavelength $\lambda = 632.8\,nm$ and a power of $15\,mW$. The laser beam is directed through a lens (focal length $f = 10\,cm$) which focuses the beam inside the cell. A filter is used to preserve the phototube.

The cell and the cell holder

For the experiments we used a parallelepiped cell in optical glass with $1 \times 1\,cm$ square base. The cell is placed inside a cell holder which contains a resistance to heat the sample and a refrigeration circuit to maintain the desired temperature. The temperature is remotely controlled through the PC. A remotely controlled magnetic stirrer (Variomag) is positioned inside the base of the cell holder. A magnetic anchor $6 \times 3\,mm$ is placed in the cell.

Injector

The injector is used to add small quantity of surfactant to the sample during the measurement. The injector is a Genie plus syringe pump (Kent Scientific) with Hamilton syringes. The syringe is linked

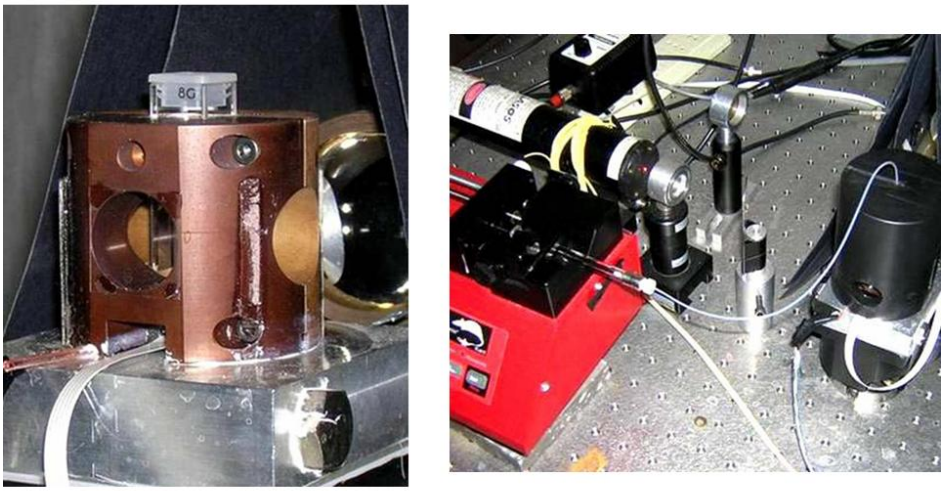

Figure 2.6: Cell holder (left) and injector (right) of the Static Light Scattering experimental setup.

to a small tube which connects directly to the cell through a hole located on the cell plug. The pump is remotely controlled through the PC to set the quantity and the frequency of the surfactant additions.

Signal detection

A phototube RCA 931B is placed at an angle of 90° and collects the light diffused by the sample. The phototube is connected to the PC through a 34970A Data acquisition control unit (Agilent technologies).

2.2 Dynamic Light Scattering

A colloidal suspension illuminated by coherent light, at any instant, presents a grainy random far-field diffraction pattern or speckle pattern (see Figure 2.7(a)).

At some point in the far field the waves scattered by the particles interfere constructively, generating a large intensity, while at some other points destructive interference leads to a small intensity. Moreover, due to particles Brownian motion, the scattering medium is not static but evolves in time. The speckle pattern fluctuates from one random configuration to another. The intensity $I(\boldsymbol{q}, t)$ at one point in the far field fluctuates in time, as sketched in Figure 2.7(b). This random signal contains

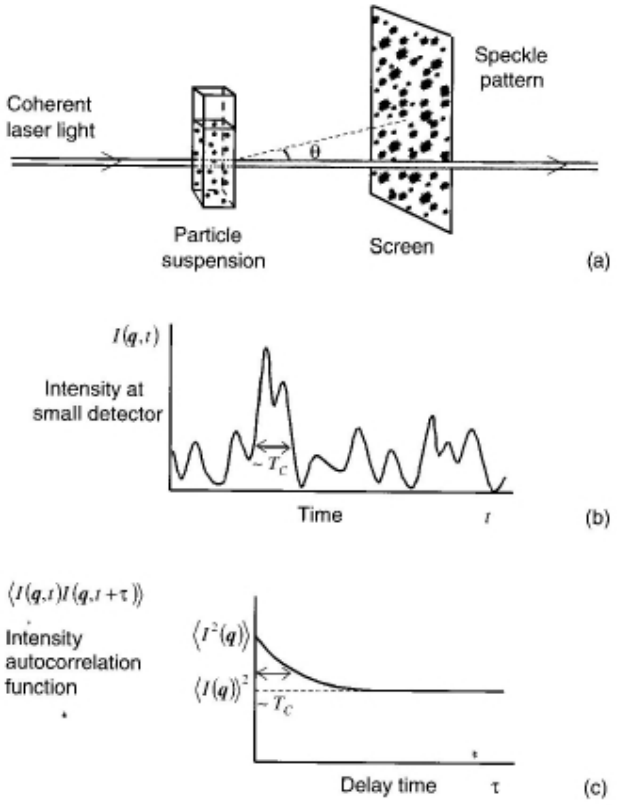

Figure 2.7: (a) Coherent light scattered by a random medium such as a colloidal suspension, generates a random diffraction, or speckle, pattern in the far field. As the particles move of Brownian motion, their position and the phase of the scattered light change. Hence the speckle pattern fluctuates from one random configuration to another. (b) The fluctuating intensity captured by a detector having size comparable to a speckle size. (c) The time autocorrelation function of the scattered intensity shown in (b). The time-dependent part of the correlation function decays with a time constant T_c equals to the typical fluctuation time of the scattered light.

information on the particles motion. It's worthwhile noticing that the intensity fluctuations cannot be detected by human eye for two reasons: they are too fast with respect to the human eye response time and they vary from one point to another so that they coincide only over short spatial length. A region where the phases of the diffused waves do not vary significantly is called coherence area. In different coherence areas the intensities fluctuate independently; if the light collector opening is larger than a coherence area the signal to noise ratio reduces due to deletion effect between light waves coming from different coherence regions. For a monochromatic source the diffused light is coherent inside a solid angle of the order of λ^2/A, where A is the section of the scattering volume perpendicular to the scattering direction.

In Dynamic Light Scattering measurement (DLS) the main sample properties are extracted from the time correlation function of the fluctuating intensity, defined as:

$$G^{(2)}(\tau) = \langle I(\boldsymbol{q},t)I(\boldsymbol{q},\tau)\rangle \equiv lim_{T\to\infty}\frac{1}{T}\int_0^T dtI(\boldsymbol{q},t)I(\boldsymbol{q},t+\tau). \tag{2.12}$$

The signal $I(\boldsymbol{q},t)$ is compared with a delayed version of itself $I(\boldsymbol{q},t+\tau)$ for all starting time t and for a range of delayed time τ. Typical behavior of the intensity correlation function is shown in Figure 2.7(c). At zero delay time Equation 2.12 reduces to:

$$lim_{\tau\to 0}\langle I(\boldsymbol{q},0)I(\boldsymbol{q},\tau)\rangle = \left\langle I^2(\boldsymbol{q})\right\rangle$$

For greater delay times, fluctuations in $I(\boldsymbol{q},t)$ and $I(\boldsymbol{q},t+\tau)$ are not correlated, so that the average in Equation 2.12 can be separated:

$$lim_{\tau\to\infty}\langle I(\boldsymbol{q},0)I(\boldsymbol{q},\tau)\rangle = \langle I(\boldsymbol{q},0)\rangle\langle I(\boldsymbol{q},\tau)\rangle = \langle I(\boldsymbol{q})\rangle^2$$

Since $\left\langle I^2(\boldsymbol{q})\right\rangle \geq \langle I(\boldsymbol{q})\rangle^2$ for every $I(\boldsymbol{q},t)$, the starting value of the correlation function is always greater then the value at long time. Thus the intensity correlation function decays from the mean-square intensity value at small times to the square of the mean at long times through a characteristic decay time T_c, that is a measure of the fluctuation time of the intensity. A significant case is represented by the exponential decay:

$$G^{(2)}(\tau) - G^{(2)}(\infty) \propto exp\left(-\tau/\tau_c\right),$$

where τ_c indicates the correlation time.

Another important quantity is the electromagnetic field correlation function $G^{(1)}(\tau)$, that is the

Fourier transform of the spectrum:

$$G^{(1)}(\tau) = \langle E(\boldsymbol{q}, t)E^*(\boldsymbol{q}, t+\tau))\rangle \,.$$

As a consequence the spectrum can be written as:

$$S(\omega) = \frac{1}{2\pi}\int G^{(1)}(\tau)e^{-i\omega\tau}d\tau,$$

where ω is the frequency.
In general there is not an easy relation linking $G^{(1)}(\tau)$ to $G^{(2)}(\tau)$. In many DLS experiments, the total diffused light is the sum of waves diffused by independent particles and presents a gaussian statistic. In this specific case the Siegert relation is valid:

$$G^{(2)}(\tau) = I_0^2\left(1+\gamma\left|g^{(1)}(\tau)\right|^2\right), \tag{2.13}$$

where $g^{(1)}(\tau) = G^{(1)}(\tau)/G^{(1)}(0)$ is the normalized field correlation function, I_0 is the mean detected light and γ is an efficiency factor. For perfectly coherent incident light measured on a singular coherent area $\gamma = 1$; if the light detected comes from a region J times larger than a coherence area, the efficiency factor is of the order of $1/J$. A low efficiency makes the measurement very sensible to the presence of intensity fluctuation caused by laser instability or by the presence of dust in solution. It could be desirable to measure light coming from a singular coherence area. However, if the coherence area is too small, there is not a sufficient intensity reaching the detector. In DLS experiments it is necessary to find a compromise between these two requirements.

Correlation function of particles moving of Brownian motion

As introduced in the previous section, the intensity fluctuation are caused by the Brownian motion of the particles in the dispersion. The smaller the particles are, the larger is the diffusing velocity. According to Brownian model, every particle moves on a casual path, but there is a net flux of particles moving from high concentration regions toward low concentration regions. The Brownian motion is responsible for the diffusion motion, which can be characterized through the diffusion coefficient D . According to the diffusive motion laws, the displacement Δx in the time δt of a particles moving of Brownian motion in a certain direction is:

$$\overline{\Delta x^2} = 2D\delta t$$

Consider a pair of particles moving with relative motion; the waves diffused by the two particles at the observation point have a phase difference given by $\boldsymbol{q} \cdot \boldsymbol{r}$, with $\boldsymbol{r}$ relative distance vector. The diffused intensity becomes completely independent from its initial value when the particles moves of a distance $\Delta x \approx q^{-1}$ along the scattering vector $\boldsymbol{q}$. The correlation time τ_c acquires the value:

$$\tau_c \approx \frac{1}{Dq^2}. \tag{2.14}$$

and is the time necessary to a particle to moves on a distance q^{-1} along $\boldsymbol{q}$.

It can be shown [24] that the correlation function for the diffused light can be written as:

$$G^{(1)}(\tau) = I_S e^{i\omega_0 \tau} e^{-Dq^2\tau} \tag{2.15}$$

and the spectrum assumes the form:

$$S(\omega) = \frac{I_S}{\pi} \frac{Dq^2}{(Dq^2)^2 + (\omega - \omega_0)^2} \tag{2.16}$$

Determination of particles dimension

Starting from Equation 2.13 and Equation 2.15, the measure of the intensity correlation function allows to determine the diffusion coefficients of the particles in the suspension. The diffusion coefficient of an infinite dilute dispersion depends on the particles shape and is related to the friction coefficient f through the relation:

$$D = \frac{k_B T}{f}, \tag{2.17}$$

where k_B is the Boltzmann constant and T is the absolute temperature.
For a spherical particle of radius R, $f = 6\pi\eta R$, where η is the dynamic viscosity of the solvent. η is a temperature dependent quantity, as shown in Figure 2.8. By substituting f in Equation 2.17, the Stokes-Einstein relation is obtained:

$$D = \frac{k_B T}{6\pi\eta R}, \tag{2.18}$$

and the radius of spherical particles can be calculated as:

$$R = \frac{k_B T}{6\pi\eta D}.$$

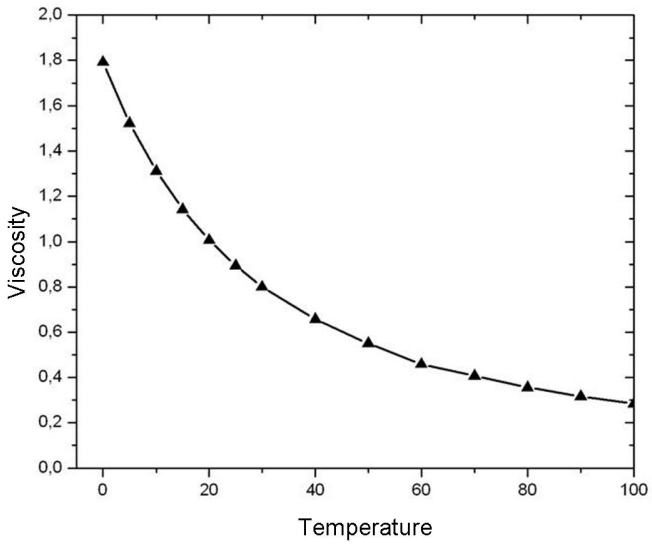

Figure 2.8: Temperature dependence of water viscosity.

It's worthwhile noticing that diffusing particles drag the solvent, so that an apparent hydrodynamic radius can be introduced:

$$R^h_{app} = \frac{k_B T}{6\pi\eta D_{app}},$$

where D_{app} is the diffusion coefficient measured through DLS experiments. The apparent hydrodynamic radius allows to model also the scattering signal coming from non-spherical particles.

The previous treatment applies rigorously only to very dilute solution, where viscosity and particles interactions can be neglected. Solvent viscosity indeed grows with the particles concentration affecting, through Equation 2.18, the diffusion coefficient and the determination of the particles radius.

The presence of interactions between the particles can have different effects on the dynamic behavior of the system. Repulsive interactions create local concentration fluctuations which dissipate more rapidly: thus the diffusion coefficient is higher and the apparent hydrodynamic radius is lower. On contrary, attractive interactions make fluctuations dissipate slower, so that the diffusion coefficient is lower and the apparent hydrodynamic radius is higher.

2.2.1 Dynamic Light Scattering experimental setup

The Dynamic Light Scattering experimental setup, shown in Figure 2.9, is composed by a laser source (A), some optical components (B), a temperature controlled cell holder (C), a phototube (D) and a PC for the data analysis.

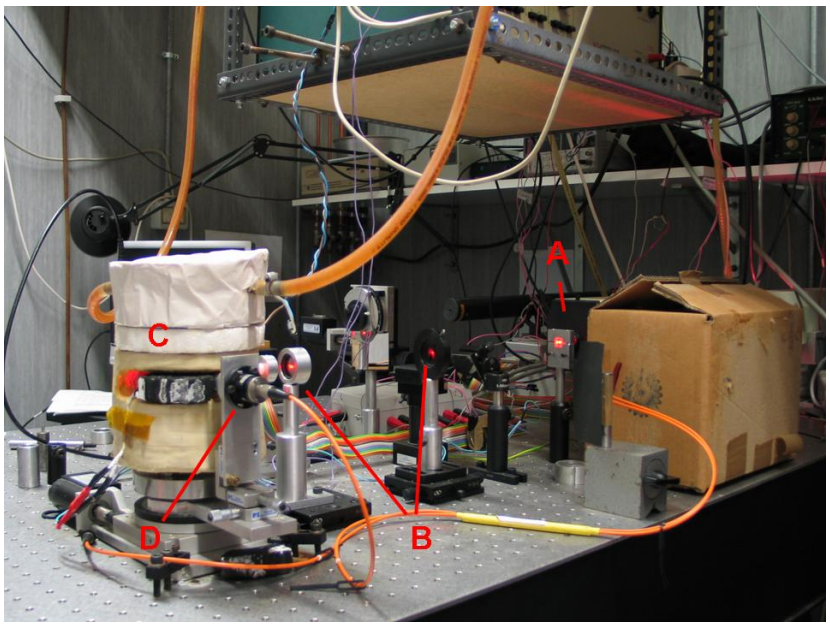

Figure 2.9: Dynamic Light Scattering experimental setup. The letters refer to the principal parts of the instrument described in the text.

Laser sources

The principally used optical source is a He-Ne laser (LGK 7626S, Lasos) with wavelength $\lambda = 632.8\,nm$ and a power of $50\,mW$. The beam has an exit diameter of $0.49 \pm 0.05\,mm$ and a divergence inferior to $1.7\,mrad$.

To perform measurements on very dilute sample we used a COMPASS 315M (Coherent) laser of wavelength $\lambda = 532\,nm$ and $150\,mW$ of power. In this case the beam diameter is $0.34 \pm 0.02\,mm$ and the divergence is inferior to $2.2\,mrad$.

Optical configuration

To perform measurements with the He-Ne laser, the laser beam is vertically polarized and passes through a pin-hole with $2\,mm$ diameter and placed at a distance of $26\,cm$ from the laser. Instead to use the green laser, two 45° mirrors were added to carry the laser beam in the right direction.

The laser beam is focused through a lens with focal length $f = 10\,cm$ into the center of the

thermostat. The longitudinal position of the lens can be varied thus modifying the dimension of the light spot on the sample. Indeed, for a Gaussian beam:

$$w_0 = \sqrt{\frac{\lambda z_0}{\pi}}, \tag{2.19}$$

where, as shown in Equation 2.2.1, w_0 is the beam characteristic dimension and z_0 is the so called Rayleigh range, the length over which the beam is collimated.

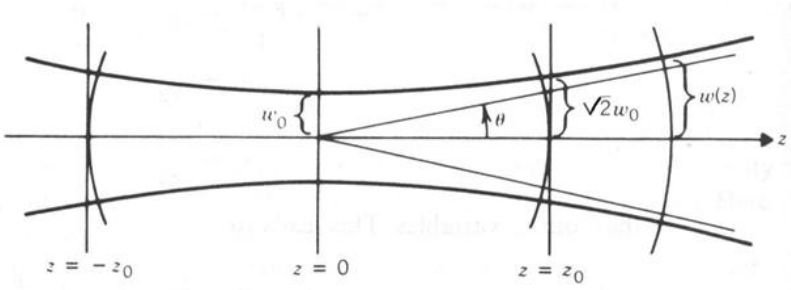

Figure 2.10: Gaussian beam.

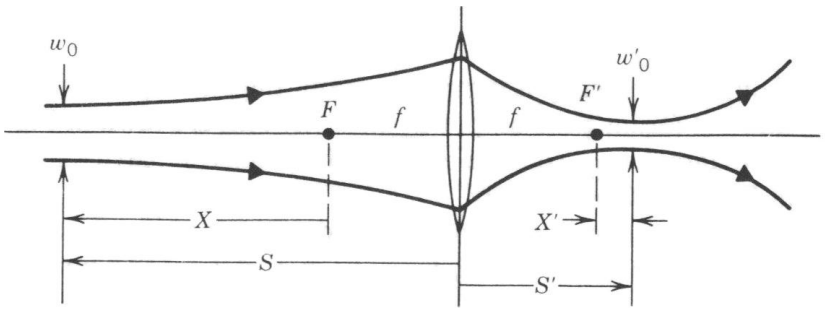

Figure 2.11: Focusing of a gaussian beam.

If a gaussian beam is focused through a lens, its beam waist varies according to the following equation:

$$w'_0 = \sqrt{\frac{\lambda z'_0}{\pi}} = w_0 \sqrt{\frac{f^2}{X^2 + z_0^2}} \tag{2.20}$$

According to Figure 2.11 X is the distance between the beam waist and the lens minus the lens focal length. In our setup, $X = 0.35\,m$ and thus $w'_0 = 3.1 \cdot 10^{-5}\,m$ and $z'_0 = 4.7\,mm$. The beam waist of the focused beam is short: as a consequence a short displacement of the lens causes a large variation in the dimension of the beam reaching the cell.

Figure 2.12: Sample cell for Dynamic Light Scattering measurements.

Sample cell

To be able to measure small sample volumes ($65\,\mu l$) we have designed the cell shown in Figure 2.12. The inner cell is a cylindric cell with one open side, realized by Pasquali S.R.L.. The inner and the external diameter are 3 and $5\,mm$ respectively; the height is $32\,mm$. The external cell is a parallelepiped with square base $1 \times 1\,cm$ (Starna) endowed with a holed Plexiglass plug and a Teflon support to hold the cylindric cell. A cylindric Plexiglass support is positioned on the bottom of the large cell. The support has a center hole with a diameter equal to the external diameter of the cylindric cell.

To test the alignment of the system we positioned a millimeter paper at a distance of approximately $2\,m$ from the thermostat to control that the light beam is not deviated by the sample cell.
The optical matching between the two cells is realized through a oil (Castor oil refined, Riedel-de Haën) with refractive index $n = 1.479 \pm 0.002$, very close to the glass refractive index.
In some cases of very dilute samples, measurements have been performed by injecting the sample directly in the big parallelepiped cell. During preliminary test measurements we have noticed that the use of the cylindric cell requires a higher alignment precision than the parallelepiped cell, because the beam can be deviated by the bending of the cell surface.

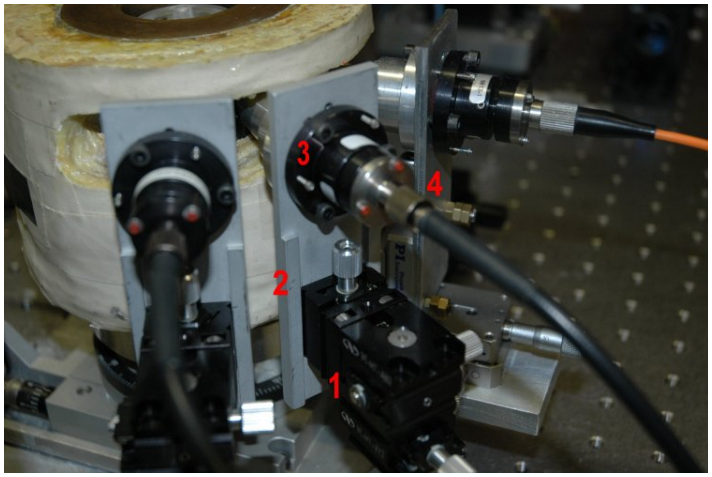

Figure 2.13: Apparatus for light detection through optical fiber. The numbers highlight the main parts described in the text.

The cell holder

The diffusion coefficient D depends on the temperature both explicitly and through the viscosity. The curves that describe the viscosity temperature dependence is of the form $\eta = a \cdot e^{b/T}$. In a water solution the factor T/η of Equation 2.18 varies of about 3% every centigrade degree. It is thus important to control and stabilize the temperature.

To control the sample temperature the cell is placed inside a metal thermostat covered with an insulating material. The cap of the thermostat contains some electric resistances and a tube for water circulation. The system is remotely controlled through a PC with a RTC (Remote Temperature Control) software (INSTEC), which allows to set, reach and maintain the desired temperature.

The temperature is measured through two independent thermistor placed inside the thermostat in the proximity of the sample. The precision in controlling the temperature is 0.1 degrees.

Light detection through optical fiber

The diffused light is collected through an apparatus previously realized in our laboratory and composed by different parts, as highlighted in Figure 2.13. A holed truncated cone is mounted on a metal plate (2) and extends inside the cell holder. Inside the cone are inserted a rotating polarizer and a lens with focus inside the sample cell. On the opposite side of the plate there is a collimator (OZ Optics) (3), consisting in a lens and an optic fiber connector (4). The connector focuses the detected light, previously straightened by the lens, inside the optic fiber. Three combined translators (1) give access to the illuminated zone inside the sample cell.

The collected light is carried through a mono-mode optic fiber ($10\,\mu m$ core diameter) to a pho-

toncounting head (PMT R7400, Hamamatsu), i.e. a phototube connected to the PC. The mono-mode optic fibers transport only a single propagation mode of the electromagnetic field and thus allow to detect only one speckle. To maximize the efficiency of the detected signal the beam diameter at the collection point w'_0 and at the exit of the optic fiber a_f must be as small as possible. Indeed the intensity depends on these diameters through the relation:

$$I \propto \left(\frac{1}{w'_0 2 + a_f^2} \right). \tag{2.21}$$

Another relation for the diameters can be written by considering that the optic fiber has to capture only one speckle an that the incident beam needs to be very focused to increment the incident power:

$$w'_0 = a_f. \tag{2.22}$$

Hence during optical alignment we have minimized both the diameters trying to satisfy Equation 2.22.

The signal is analyzed through a digital correlator BI9000AT (Brookhaven Instruments Corporation).

2.3 Birefringence

A system (solid or liquid) is said to be birefringent if a light beam propagates across the sample with different velocities depending on the incident angle and on the polarization direction. Such a system presents always three perpendicular directions with a related refractive index. When the light propagates along one of these directions, it maintains the entrance polarization and the phase velocity is given by $v_i = c/n_i$ (where the index i stands for the light polarization direction). In a birefringent medium the relations between induced dipoles are of tensorial nature. In general, simple liquids or colloidal dispersions can present an induced birefringence under the effect of external fields which perturb the spatial isotropy giving the sample an axial symmetry. When the external field is the electric one the effect is called electric birefringence or Kerr effect.

The birefringence in a uniaxial system is defined as:

$$\Delta n = n_{\parallel} - n_{\perp},$$

namely the difference between the refractive indexes in the direction parallel and perpendicular to the symmetry axis respectively i.e. for the Kerr effect the electric field direction. When the sample

structure is isotropic Δn must be independent on the sign of the electric field E, so that one expects Δn to depend at the lower order to E^2 (Kerr effect). The extent of the Kerr effect is usually quantified through the Kerr constant B, that expresses the dependence of Δn on E^2 in the limit of low field.

$$B = lim_{E\to 0}\frac{n_{\parallel} - n_{\perp}}{\lambda E^2}, \tag{2.23}$$

where λ represents the wavelength of the incident light. Generally birefringence experiments focus on studying the relaxation of the induced birefringence after the electric field id turned off, a process governed by the rotational correlation time [25]. Few studies are instead devoted to the steady-state amplitude of the Kerr constant in an ac field, the approach employed in [23]. In Frequency Resolved Electric Birefringence (FREB) experiments a sine-wave voltage of frequency ν is applied to a cell endowed of two electrodes. In complex notation the applied electric field can be written as:

$$E_0 = Re[E_{0\nu}e^{-i2\pi\nu t}].$$

After a starting transient, the signal consists of a dc and an ac component, Δn_{dc} and Δn_{ac} respectively. FREB measurements study the steady component of the induced birefringence as a function of the external field frequency ν. In particular the dc part of the Kerr coefficient results:

$$B\,(\nu) = \frac{\Delta n_{dc}(\nu)}{\lambda (E_0^2)_{dc}}, \tag{2.24}$$

where $(E_0^2)_{dc} = E_0^2/2$ is the mean-square amplitude of the applied electric field.

When particles with no permanent dipole and with axially symmetric polarizability are considered, the orientation of the particles can be specified through the angle θ between the particles axis and the electric field direction. In that case the optical polarizability tensor of the particles $\underline{\underline{\alpha^o}}$ is diagonal, with diagonal elements given by $\alpha_{\parallel}^o$ and $\alpha_{\perp}^o$. Assuming $\Delta\alpha^o = \alpha_{\parallel}^o - \alpha_{\perp}^o$, it can be shown [25] that the Kerr coefficient $B(\nu)$ of the suspension can be written as:

$$B(\nu) = \frac{N\Delta\alpha^o S_{dc}(\nu)}{\lambda n \epsilon_0 E_{0\nu}^2}, \tag{2.25}$$

where n is the solvent refractive index, ϵ_0 the vacuum dielectric permittivity while S_{dc} denotes the dc component of the non polar orientational order parameter defined as:

$$S_{dc}(\nu) \equiv \int_0^{\pi} P_2(cos\theta) f_{dc}(\theta) sen\theta d\theta, \tag{2.26}$$

with $f_{dc}(\theta)$ normalized dc component of the orientational distribution function and P_2 Legendre polynomial of degree 2 defined as $P_2(x) = \frac{1}{2}(3x^2-1)$. In particular $S_{dc} = 1$ for perfect parallel alignment while $S_{dc} = 0$ for isotropic orientational distribution. Hence to calculate $B(\nu)$ it's necessary to know the angular distribution function $f_{dc}(\theta)$ of the suspended particles when exposed to an oscillatory electric field, with $f_{dc}(\theta)$ strictly depending on the particle-solvent properties and on the frequency of the applied electric field. When slightly charged particles immersed in aqueous solvent are considered, their interaction with the electric filed is not governed by a simple electrostatic coupling but the orientational distribution function $f_{dc}(\theta)$ must include the contributions due to ions transport by conduction, diffusion and hydrodynamic which all cooperate to particles alignment. In this situation it is more convenient to directly relate the Kerr coefficient $B(\nu)$ to the force acting on the dispersed particles. It has been shown [26] that the angular distribution function $f_{dc}(\theta)$ can be related to the torque $\boldsymbol{\sigma}_{dc}(\theta)$ acting on each particle:

$$f_{dc}(\theta) = Fexp\left(\frac{1}{k_B T}\int_0^{\theta} \boldsymbol{\sigma}_{dc} \cdot \boldsymbol{u}_{\theta} d\theta\right), \tag{2.27}$$

with F normalization constant and $\boldsymbol{u}_{\theta}$ versor in θ direction. By combining Equation 2.27 with Equation 2.25 an expression of $B(\nu)$ as a function of $\boldsymbol{\sigma}_{dc}$ is obtained . The separation of the Kerr coefficient in a dc and an ac components derives from its linear dependence on the squared electric field [27]. $B(\nu)$ can thus be evaluated from the torque independently for each frequency ν.

2.3.1 Electric and Hydrodynamic torque

The total torque $\boldsymbol{\sigma}_{dc}$ contains an electric and an hydrodynamic contribution, because a colloid under an external electric field experience both the effects:

$$\boldsymbol{\sigma}_{dc} = \boldsymbol{\sigma}_{dc,E} + \boldsymbol{\sigma}_{dc,H} \tag{2.28}$$

The evaluation of $\boldsymbol{\sigma}_{dc,E}$ and $\boldsymbol{\sigma}_{dc,H}$ proceeds by determining the moment of the forces acting on the particle surface:

$$\boldsymbol{\sigma}_{dc,E,H} = \int_S \boldsymbol{r} \times \left(\underline{\underline{\gamma}}_{dc,E,H} \cdot \boldsymbol{n}\right) dS, \tag{2.29}$$

where $\boldsymbol{r}$ is the vector identifying the position of the particle surface element dS, $\boldsymbol{n}$ is the versor normal to dS, $\underline{\underline{\gamma}}_{dc,E}$ is the Maxwell electric stress tensor while $\underline{\underline{\gamma}}_{dc,H}$ is the hydrodynamic stress tensor, accounting for viscosity and pressure.

We first evaluate the electric stress tensor $\underline{\underline{\gamma}}_{dc,E}$. It is worthwhile noticing that, for a dilute system,

the electric field $\boldsymbol{E}$ around particle surface is due to the superposition of three contributions i.e. we can write $\boldsymbol{E} = \boldsymbol{E}_0 + \boldsymbol{E}_{p,dc} + \boldsymbol{E}_{p,ac}$, where $\boldsymbol{E}_0$ is the external electric field (in FREB experiments an a.c. field), $\boldsymbol{E}_{p,dc}$ is the steady field inside the unperturbed double layer and $\boldsymbol{E}_{p,ac}$ is the oscillating field due to the induced polarization of the particle. When dealing with spherical particles the latter term $\boldsymbol{E}_{p,ac}$ is a dipolar field oscillating at the same frequency ν of the externally applied electric field. In this case it is useful to relate the electric field to the associated dipole potential $\Psi_{dip}(\boldsymbol{r}) = \Re\left[\Psi_{dip,\nu}(\boldsymbol{r})e^{-i2\pi\nu t}\right]$ whose complex amplitude is given by:

$$\Psi_{dip,\nu}(\boldsymbol{r}) = \frac{1}{4\pi\epsilon_0\epsilon_s}\frac{\alpha\boldsymbol{E}_{0,\nu}\cdot\boldsymbol{r}}{r^3}.$$

In the above equation $\boldsymbol{r}$ is the distance from the center of the sphere, ϵ_s is the solvent relative dielectric constant and α is the polarizability of the particle with including its counterion cloud. The calculation of α can be performed within the context of the Standard Electrokinetic model either numerically [28] or through approximate analytical solutions [29, 30, 31]. The polarizability α is determined by a dynamic local balance of incoming and outgoing ions carried by hydrodynamic, diffusion and electromigration flows, and thus is always a "kinetic" quantity. Generally α is a complex variable because of the finite velocities of both the ions and the solvent flows. In the case of non spherical particles, the polarizability is a tensor $\underline{\underline{\alpha}}$ and the dipolar potential assumes the form:

$$\Psi_{dip,\nu}(\boldsymbol{r}) = \frac{1}{4\pi\epsilon_0\epsilon_s}\frac{\left(\underline{\underline{\alpha}}\boldsymbol{E}_{0,\nu}\right)\cdot\boldsymbol{r}}{r^3}.$$

The diagonal elements of the polarizability tensor, $\alpha_\parallel$ and $\alpha_\perp$ are the particle polarizability in the direction parallel and perpendicular to the particle's axis respectively. With this notation the d.c. component of the electric torque $\boldsymbol{\sigma}_{dc,E}$ assumes the form:

$$\boldsymbol{\sigma}_{dc,E} = \langle\boldsymbol{p}\times\boldsymbol{E}_0\rangle = \frac{1}{2}\Re\left(\underline{\underline{\alpha}}(\nu)\cdot\boldsymbol{E}_{0,\nu}\right)\times\boldsymbol{E}_{0,\nu}, \tag{2.30}$$

with $\boldsymbol{p} = \Re\left(\underline{\underline{\alpha}}(\nu)\boldsymbol{E}_0 e^{-i2\pi\nu t}\right)$. Indicating with $\alpha_\parallel^{'}$ and $\alpha_\perp^{'}$ the real part of $\alpha_\parallel$ and $\alpha_\perp$ respectively the electric torque can be expressed in term of the difference between the real parts of the polarizability:

$$\boldsymbol{\sigma}_{dc,E} = -\frac{1}{2}\left(\alpha_\parallel^{'} - \alpha_\perp^{'}\right)E_{0,\nu}^2 sin\theta cos\theta\boldsymbol{u}_\theta. \tag{2.31}$$

The evaluation of the hydrodynamic torque $\boldsymbol{\sigma}_{dc,H}$ is far more complicated. In fact, when centro-symmetric particles are considered, there is no E-level. The calculation of Equation 2.29 requires the

knowledge of solvent flow velocity to E^2 level.

In [32], Fixman reported an electrokinetics algorithm which allows to obtain numerical solution to the full, non-linearized electrokinetic problem. This algorithm models a system consisting of one macroion (a cylindrical section with identical, hemispheroidal endcaps) in a salt solution subject to an arbitrary sequence of pulsed electric fields and pulsed translational and rotational velocities. The evolving fields considered include the solvent flow obeying to Navier-Stokes equations with solvent-inertia suppressed, the electrostatic potential, satisfying Poisson's equation, the mobile ion concentrations according to Smoluchowski diffusion equations and possibly a redistribution of macroion surface charge. This algorithm calculates dielectric response, force and torque acting on the particle. From Fixman's calculation results that while $\boldsymbol{\sigma}_E$ gives always a positive contribution to the total torque acting on colloidal particles i.e. it orient rod-like particles with the long axis parallel to the field direction, the hydrodynamic torque $\boldsymbol{\sigma}_H$ can be negative in the case of coions having low diffusion coefficient, thus favoring particles perpendicular orientation.

2.3.2 Birefringence experimental setup

The experimental setup for Birefringence measurement is shown in Figure 2.14. A monochromatic

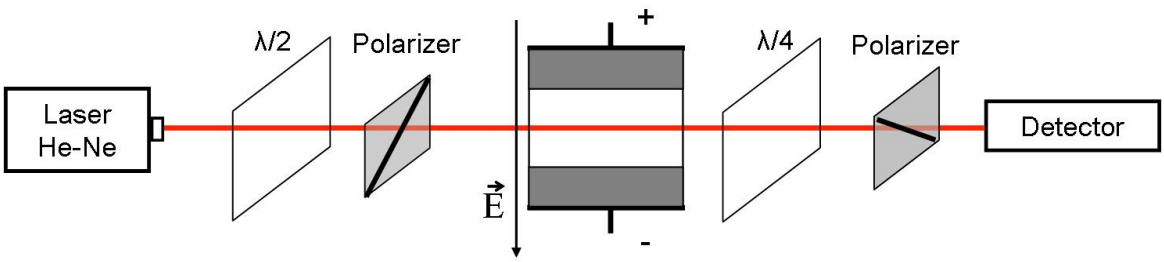

Figure 2.14: Scheme of the optical setup for Birefringence measurements.

linearly polarized laser beam is directed through a Kerr cell, a cuvette endowed of two windows realized in optical glass and in which are inserted two parallel plain electrodes. A tension pulse with variable amplitude and frequency is applied to the electrodes. The setup for the electric field generation will be explained in detail in the following subsection.

In birefringence measurements the relative position between the electrodes and the laser beam polarization plays a crucial role: the electric field must form a $45°$ angle with the light polarization direction. The $\lambda/2$ plate forms a 45° angle between the light polarization direction and the horizontal direction, namely the direction of the external electric field. Another polarizer (called analyzer in the following), which can be remotely controlled, is positioned after the exit window of the cell: the

optical axis of the analyzer is crossed to that of the entrance polarizer. If the studied sample is not a birefringent one, there is no light intensity transmitted through the system; on contrary, if the sample presents optical birefringence, the transmitted intensity becomes elliptically polarized and thus is partially transmitted. A $\lambda/4$ plate is inserted between the Kerr cell and the analyzer in order to increment the instrumental sensibility and to reduce the errors due to parasitic effects. Therefore the transmitted light is collected by a photodiode, preceded by an interferential filter. The optical signal is then sent to an oscilloscope, together with the voltage applied at the cell electrodes. The cell is positioned into a temperature controlled cell holder (see next section), which allows to reduce the sample evaporation under the effect of the electric field.

The measurement consists in revealing the light transmitted by the sample in presence of the electric field and in zero field condition. If the electric field is applied along the x direction and the laser beam propagates along z, being the polarizer oriented at $45°$ respect to x, the optical field incident on the cell is:

$$E_x^o = E_y^o = \frac{E^o}{\sqrt{2}}.$$

If the sample in the cell is birefringent $n_x = n_\parallel \neq n_\perp = n_y$ and thus the x and y components of the light beam are out of phase of an angle δ given by:

$$\delta = \frac{2\pi(n_\parallel - n_\perp)l}{\lambda},$$

with l optical path length and λ laser beam wavelength. The radiation transmitted by the cell is thus elliptically polarized and has a non-null intensity given by:

$$I(\delta \neq 0) = I_0 sen^2(\frac{\delta}{2}),$$

where I_0 is the cell transmitted intensity. According to that the Kerr coefficient results:

$$B = \frac{1}{\pi l E^2} arcsen\sqrt{\frac{I(\delta \neq 0)}{I_0}}. \tag{2.32}$$

However, with this optical configuration, to know B it's necessary to know I_0. To increment signal-to-noise ratio, it is better to discross polarizer and analyzer of a small angle α: in this way, the light intensity transmitted in zero field condition I_α is function of the angle α and of the incident light

intensity I_0. In this way B assumes the form:

$$B = \frac{1}{\pi l E^2}[arcsen(\sqrt{\frac{I_\delta}{I_\alpha}} - sen\alpha) - \alpha]. \tag{2.33}$$

Electric field generation and signal acquisition

The PhD work has regarded also the reconfiguration of the experimental setup for the generation of the electric field and for signal acquisition for Birefringence and Electric Transmitted Light Intensity (ETLI) measurements, whose connections scheme is shown in Figure 2.15.

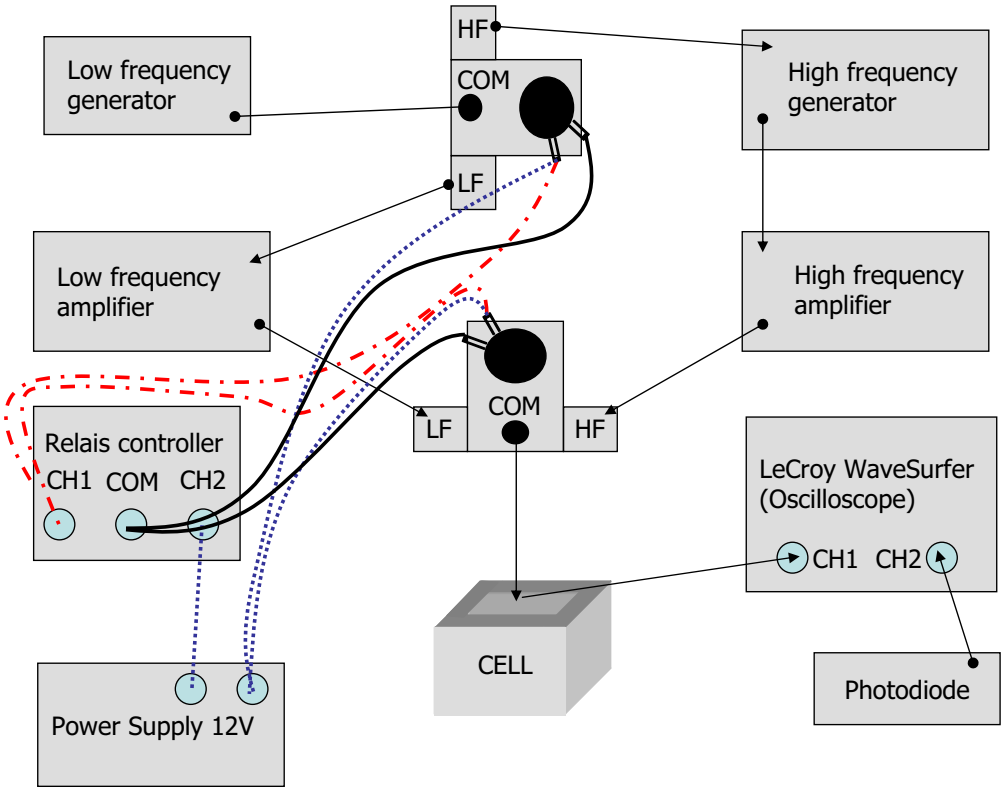

Figure 2.15: Electric scheme of Birefringence and ETLI setup for electric field generation.

The measurement is controlled in remote mode through a LabVIEW program. All the instruments are connected to the PC through RS−232 serial ports (except the amplifiers which do not need to be remotely controlled). Figure 2.16 shows the logic scheme of the setup for Birefringence and ETLI measurements: the only difference between the two apparatus is the presence in the birefringence setup of an analyzer after the cell, remotely controlled through the PC.

The electric field is generated by an arbitrary wave function generator (Agilent 33120), whose output is sent at the COM port of a coaxial relay (TOHTSU CX230L). The arbitrary generator is also

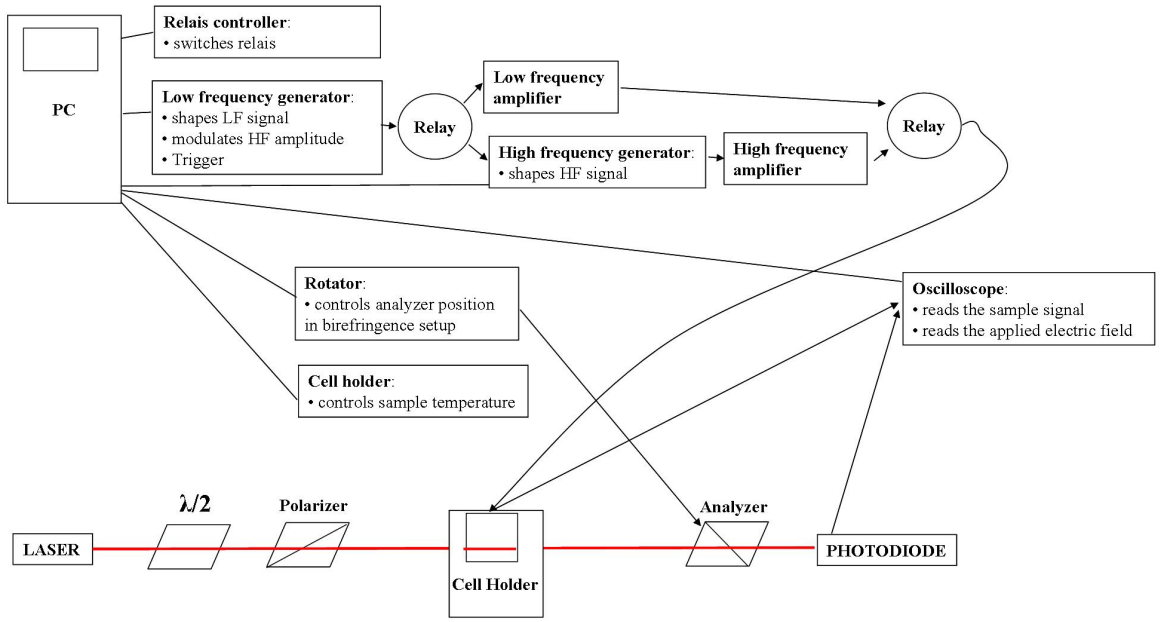

Figure 2.16: Logic scheme of Birefringence and ETLI measurements setup.

the trigger for the whole system: its trigger signal is sent to the EXT channel of the Oscilloscope (LeCroy WaveSurfer Xs). The relay has two output ports: one for the "low frequency" line (electric field frequency $\nu \leq 1\,MHz$) and the other for the "high frequency" line ($\nu \geq 1\,MHz$). In the low frequency line the electric wave function passes through a Low Frequency Amplifier (Krohn-Hite) and then enters into another relay (TOHTSU CX530) to be eventually sent to the sample cell electrodes. For the generation of a high frequency signal, the arbitrary generator produces a square wave which will be modulated with the desired amplitude and frequency by an High Frequency Generator (HP-ESG4400B) and will be amplified by an High Frequency Amplifier (AR75). The output is then sent to the port of a second relay. Both the relays are remotely controlled through a relays controller (National Control Device). In this way it is possible to send to the cell a low frequency or an high frequency field. The relay controller is fundamentally a serial switch between two channel: on channel 2 the relays are connected in series with a $12\,V$ power supply while on channel 1 no power supply is included in the circuit. In this way, by switching between the two relay controller channels, it's possible to make both the relays changing their state and to select the low frequency or the high frequency line.

The electric field is carried to the cell electrodes through coaxial cable. A coaxial T precedes the cell to send the field to the cell and to read the applied field on the oscilloscope. To read the actually applied field a passive coaxial probe (LeCroy) is necessary: indeed in our measurements we apply to the cell electrodes voltages of the order of some tens of volt, which cannot be directly measured by the oscilloscope. The oscilloscope has two channelsl: channel 1 is used to measure the applied field,

while channel 2 is connected to the photodiode and records the optical signal.

The cell for Birefringence and Electric Transmitted Light Intensity measurements is a $10 \times 10 \times 10\,mm$ cell appositely realized by STARNA and has two optical glass windows. Two vertical electrodes, with $1\,cm^2$ of surface are positioned inside the cell. The electrodes are realized in stainless steel and are placed at a distance of $1\,mm$, divided by a Teflon separator.

The cell is bedded into a cell holder, realized on purpose by Quantum Northwest (see Figure 2.17). The cell holder has four round windows with diameter of $6.4\,mm$ and is endowed of a lifter mecha-

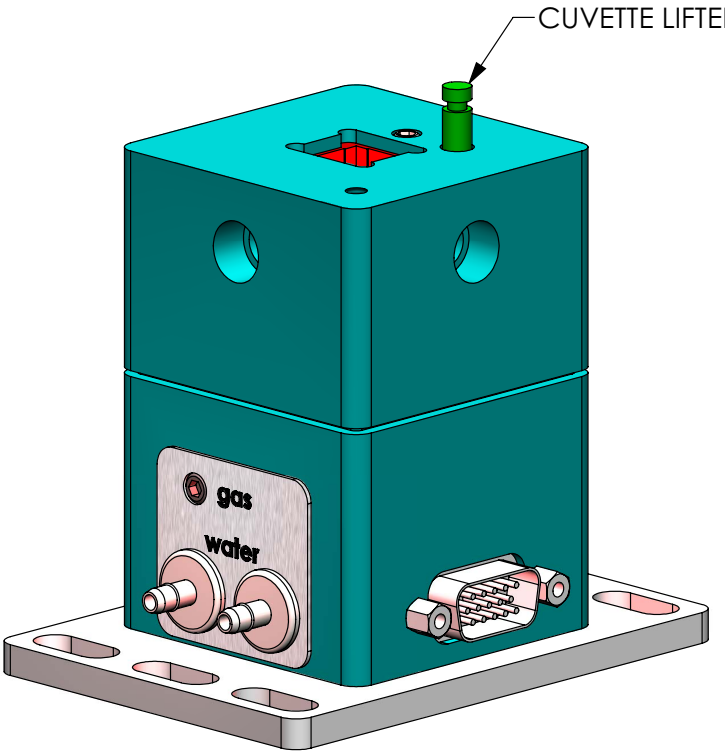

Figure 2.17: Cell holder.

nism to insert and extract the cuvette. The cell holder is designed to maintain the sample to a constant temperature, which can be remotely programmed through RS$-$232 interface. The sample cell, inside the cuvette holder, lays on a Peltier plate: a gas flux guarantees the same temperature in the whole volume.

Program for remote control

The program, realized in LabView, remotely controls the measurement and analyze the acquired data. As shown in Figure 2.16 the instrument controlled by the program are:

- **Low frequency generator**: is the trigger of the whole measurement setup. It shapes electric

field in the low frequency range. For field frequency higher than 1 MHz it sends to the high frequency generator a square wave to be modulated.

- **High frequency generator**: shapes electric field in the high frequency range.
- **Relays controller**: switches both the relays selecting low or high frequency line.
- **Rotator**: controls analyzer position in birefringence measurements.
- **Cell holder**: sets and controls the sample temperature.
- **Oscilloscope**: reads the sample optical response and the applied electric field.

The LabView program remotely assigns the above mentioned functions to the various instruments. Since the measured effects are often small and noisy, it is proper to mediate the signal, i.e. to apply the same field many times and to mediate the sample response for each frequency. The program allows to select the number of field repetitions for each frequency and automatically calculates the mean sample signal. In birefringence measurement the program calculates the Kerr coefficient and plot a preview plot of B vs. ν to control the measurement progress. The program manages different types of measurements: frequency and amplitude scan, angle scan, temperature scan.

2.4 Electric Transmitted Light Intensity

Electric Transmitted Light Intensity measurements (ETLI) determine the variation in the light transmitted by a sample induced by the application of an external electric field.

2.4.1 Turbidity determination

We used ETLI measurements to determine the optical turbidity variation induced by the electric field inside the samples. The turbidity τ is connected to the transmitted intensity I through the extinction equation:

$$I = I_0 exp(-\tau L), \tag{2.34}$$

where I_0 is the incident light intensity and L is the optical path length inside the sample. The following treatment is meaningful only if the optical path of a photon through the sample is small with respect to $\tau^{-1} = \Lambda$, which can be interpreted as the mean free path of the photon inside the diffusing medium.

In the case of a completely non-absorbing medium, the optical turbidity is directly related to the total scattering and can be calculated from the diffused intensity $I_s(\boldsymbol{q})$. For this purpose, we need to

introduce scattering cross section Σ which is defined through the differential equation:

$$\frac{\partial \Sigma}{\partial \Omega} = \frac{I_s(\boldsymbol{q}) R^2}{I_0} \tag{2.35}$$

where R is the distance between the diffusing volume V and the detector position i.e. the point where the scattered intensity I_s is measured. According to Equation 2.35 the turbidity can be defined as the total cross section per unit volume and is calculated through the integration of the former equation on the whole solid angle:

$$\tau = \frac{1}{V} \int \frac{\partial \Sigma}{\partial \Omega} d\Omega = \frac{\int I(\boldsymbol{q}) R^2 d\Omega}{I_0 V}. \tag{2.36}$$

In other terms, the turbidity represents the total power loss per unit of scattering volume and per unit of incident intensity.

In our measurements we are interested in determining the turbidity variation induced by the application of an external electric field. Through our experimental setup we are able to directly measure the transmitted intensity variation. Indicating with I_E the mean transmitted intensity in presence of an external electric field and with I_M the transmitted intensity during the rest period, and referring to Equation 2.34, the relative transmitted intensity variation is:

$$\frac{I_E - I_M}{I_M} = \frac{I_0 e^{-\tau_E L} - I_0 e^{-\tau_M L}}{I_0 e^{-\tau_M L}} = e^{-(\tau_E - \tau_M) L} - 1,$$

where τ_E and τ_M indicate the sample turbidity in presence and in absence of the electric field respectively. According to the former equation:

$$e^{-(\tau_E - \tau_M) L} = 1 + \frac{I_E - I_M}{I_M}$$

and by setting $\Delta\tau = \tau_E - \tau_M$ it results:

$$\Delta\tau = -\frac{1}{L} ln \left(1 + \frac{I_E - I_M}{I_M} \right). \tag{2.37}$$

In particular, in our experiments, we are interested in studying the turbidity variation in the two cases of light polarized parallel and perpendicular to the electric field direction, so that τ_E will assume the two intuitive notation $\tau_{\parallel}$ and $\tau_{\perp}$. In the following we will substitute the symbol τ_M with τ_0 where the 0 indicate that no electric field is applied. In zero field condition, the sample has an anisotropic orientational distribution and thus the measured turbidity does not depend on light polarization direction.

2.4.2 Electric Transmitted Light Intensity experimental setup

In Figure 2.18 is presented the optical scheme of the ETLI experimental setup. A laser beam passes

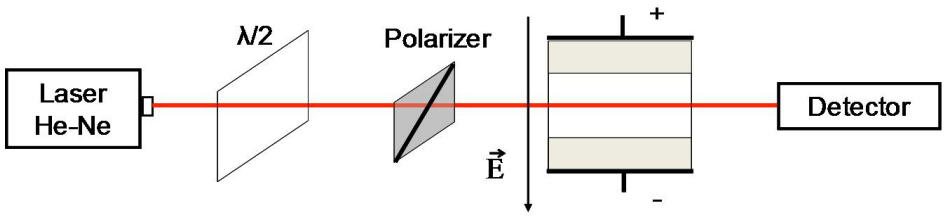

Figure 2.18: Optical scheme of the experimental setup for Electric Transmitted Light Intensity measurements.

through a sample cell endowed of two electrodes. At the cell electrodes is applied an oscillating electric field. A photodiode records the variation of transmitted light intensity induced by the external electric field. The laser employed in our measurements is an HeNe LASOS laser (LGK 7627S) with $\lambda = 632.8\,nm$ and $50\,mW$ of power. The laser beam has a diameter of $0.49 \pm 0.05\,mm$ and a divergence lower than $1.7\,mrad$. In order to optimize the signal-to-noise ratio for each sample we used a photodiode with variable gain. The photodiode is attached to a carriage with adjustable height and lateral position. A $\lambda/2$ plate is positioned after the laser, to turn the vertical polarization of the laser beam of $45°$. A polarizer, mounted on a rotator, is positioned after the $\lambda/2$: with this setup it is possible to select a light polarization parallel or perpendicular to the electric field direction. The sample cell is positioned inside a thermostat, the same used in Birefringence measurements and described in the former section.

2.5 Materials

2.5.1 ... to study biomolecular interactions

2.5.1.1 PFR 94 nanoparticles (PhP)

PFR 94 nanoparticles (Solvay-Solexis S.p.A.) are constituted by a fluorurate polymer and have a gummy, i.e. isotropy, internal structure. For more information on the chemical structure of the particles see [8]. We decided to use these colloids since their refractive index is $n = 1.3248 \pm 0.0005$ at $30°C$ of temperature, thus approximately equal to the water refractive index ($n_{H_2O} = 1.3319 \pm 0.0002$).

Hence, when the PFR 94 particles are immersed in water they are transparent and the light diffused by the dispersion is more or less the same as the one diffused by water alone. For this reason this

colloids are also called *Phantom Particles* (PhP).

Thus, when the PhP are coated with a small quantity of a material having refractive index significantly different from the water one, the increment of the scattering signal can be completely ascribed to the variation of the optical contrast. Hence this system allows to study weak biomolecular interactions if the coating molecules produce a significant variation in the diffused light.

Determination of particles radius

We determined the radius of the particles (PFR 94) through dynamic light scattering measurements. To avoid particles interaction we prepared a sample of bare particles, without the addition of any surfactant, with volume fraction $\phi = 0.001$ in water. Since the refractive index of the particles is close to that of water, the dispersion had a low scattering power and thus we performed measurements with the laser having $\lambda = 532\,nm$. From the correlation function shown in Figure 2.19 we extracted the mean particles radius $r = 30\,nm$.

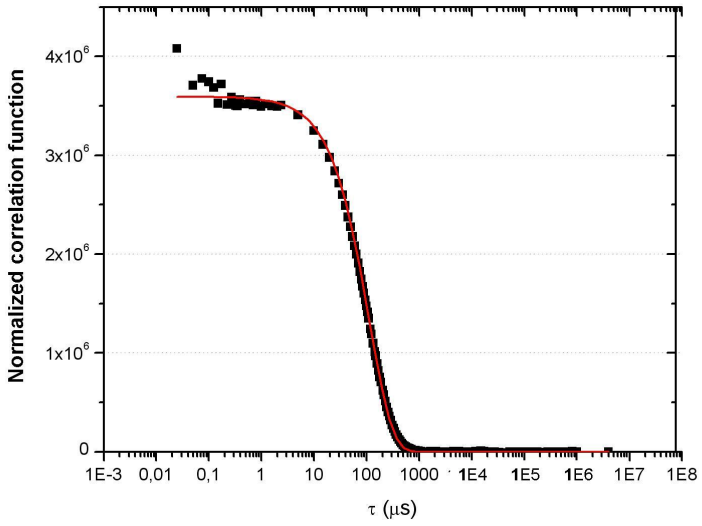

Figure 2.19: Normalized correlation function of a sample of PhP with $\phi = 0.001$.

2.5.1.2 Surfactants

Surfactants are molecules constituted by an hydrophobic and an hydrophilic part. The hydrophobic tail can be easily adsorbed onto fluorurate particles surface, leaving the hydrophilic part at contact with the water. In this PhD thesis we used three different surfactants.

The *Brij 56* has chemical formula

$$C_{16}H_{33}(OCH_2CH_2)_{10}OH$$

and its molecular weight is $683\,gmol^{-1}$.

The $C_{12}E_5$ has chemical formula

$$H-(OCH_2CH_2)_5OCH_2(CH_2)_{10}CH_3$$

and its molecular weight is $406.6\,gmol^{-1}$. Both these surfactants are neutral.

We have used another surfactant, the *Exadecyl-Trimetil-Ammonio Bromuro (HTAB)* which is charged. Its chemical formula is

$$C_{19}H_{42}BrN$$

and its molecular weight is $364.447\,gmol^{-1}$.

Glycolipids

We devoted our attention to carbohydrate-carbohydrate interactions and, in particular we coated PhP surface with *Dodecyl-α-D-Maltoside* and with *Dodecyl-β-D-Maltoside*. They are both disaccharides, i.e. constituted by two glucose molecules., have the same molecular weight ($510.62\,gmol^{-1}$) and the same chemical formula

$$C_{24}H_{46}O_{11}.$$

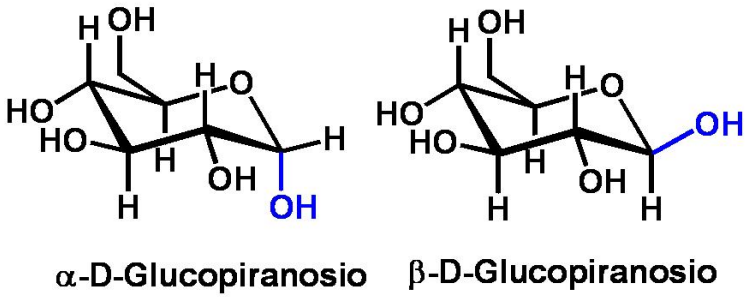

Figure 2.20: Glucose anomers.

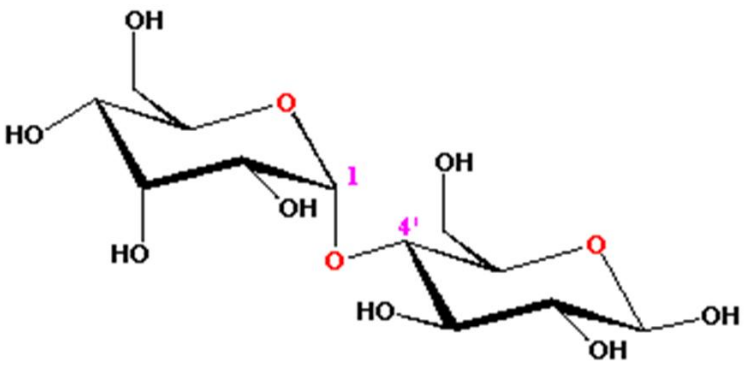

Figure 2.21: Dodecyl-α-D-Maltoside molecular structure.

They differ only for the spatial configuration of one of the carbon atoms and thus for the direction of the relative carbon-hydrogen binding. Figure 2.20 illustrates the α and β anomers of the glucose. Figure 2.21 shows the structure of Dodecyl-α-D-Maltoside.

We also wanted to study Lactose-Lactose interaction. However this molecule has low solubility, so that it can be used only at very low molar concentration but in this condition also colloidal particles become very dilute. Thus, for the moment, we could not prepare a suitable Lactose-PhP solution.

2.5.1.3 Sample preparation

We tested the stability of the particles by coating their surfaces with two different types of surfactant. In the following we describe the coating method employed.

To evaluate particles coating degree we used static light scattering measurements. We studied the intensity diffused by the sample while adding small quantity of surfactant (Figure 2.22 shows the coating with Brij56).

To describe the diffused intensity we can use Rayleigh-Gans approximation, since the difference between the refractive index of the particles and that of water is small [33]. Accordingly, the total field scattered by a particle coated with surfactant molecules can be written as the sum of the field scattered by the particle and that scattered by the surfactant (T):

$$E = E_{Php} + E_T$$

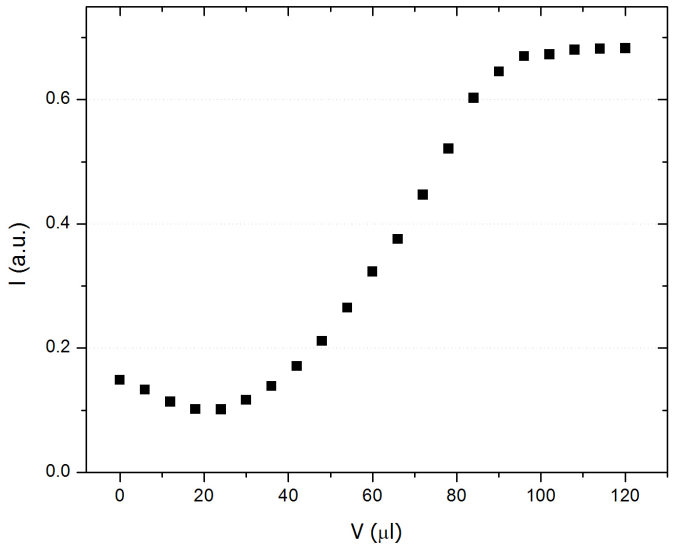

Figure 2.22: Mean intensity diffused at 90° by a sample of PhP as a function of the volume of Brij56 added to the dispersion. Each point corresponds to an addition of 6 μl of surfactant.

In the Rayleigh-Gans limit, the intensity diffused by the coated particles is [8]:

$$I = aN\left(v_P\,\Delta n_{P,W}\ + v_T\,\Delta n_{T,W}\right)^2\ +\ b$$

where a and b are constants which depend respectively on the signal detection efficiency and on the light diffused by impurities in the sample, v_P is the particle's volume, N is the particles number density and $\Delta n_{P,W} = n_P^2 - n_W^2$ is the difference between the square refractive indexes of particles (n_P) and of water (n_W). Likewise v_T is the volume of surfactant adsorbed onto one particle and $\Delta n_{T,W} = n_T^2 - n_W^2$ is the difference between the square refractive indexes of surfactant (n_T) and of water. It can be shown that:

$$v_T = \frac{M_T v_P [T_T]}{(\rho_T \phi}$$

where M_T and ρ_T are the surfactant mass and density, while T_T is the molar concentration of added surfactant. The curve (see Figure 2.22) starts from an initial value I_0, decreases to a minimum I_m and than monotonically grows reaching a stationary value. The minimum is due to the fact that the particles refractive index is lower than water. Hench by adding small volume of surfactant the refractive index of the coated particles match the water refractive index. The stationary tail indicate that the particles are fully coated with the surfactant.

2.5.2 ... to study electric field induced interactions

2.5.2.1 PTFE particles

Polytetrafluoroethylene (PTFE) particles are realized by Solvay-Solexis through polymerization in dispersion. The PTFE particles have a rod-like shape with $240\,nm$ long semiaxis and axial ratio close to 3. They have a uniaxial internal crystal structure with an average refractive index 1.37 and optical anisotropy $\Delta n = 0.04$. The PTFE particles bear a negative surface charge due in part to the adsorption of anionic surfactant during polymerization procedure and in part to the end groups of polymer chains. The highly hydrophobic surface allows the surface charge to be controlled by adsorption of surfactants. In particular by adding the anionic surfactant AOT ($C_{20}H_{37}O_7SNa$) the PTFE charge can be incremented.

2.5.2.2 Sulfate Latex spheres

Sulfate Latex spheres (Invitrogen) are polymer particles in the colloidal size range constituted by polystyrene. They are negatively charged and stabilized by sulfate charges. The particles suspensions are stable up to $0.3\,M$ univalent electrolyte concentration. The latex spheres have refractive index of 1.59 at a wavelength of $590\,nm$. The Sulfate Latex spheres are produced with various radius dimensions. In our experiments we used P200 (radius $R = 200\,nm$), P40 ($R = 40\,nm$) and P30 ($R = 30\,nm$).

Part I

Introduction

In the first part of this thesis a new experimental technique to study biomolecular interactions is proposed and tested. The basic idea is to employ bio-functionalized colloidal particles as interactions mediators and amplifiers. The employed colloidal particles are monodisperse spheres of radius $30\,nm$ which can be coated with different molecular groups. The main property of such colloids is to have a refractive index slightly different from that of water. In agreement with the literature we can study, by optical means, functionalized colloidal dispersion also at high particles volume fraction. By studying the light diffused by the colloidal dispersion we can obtain information on the interaction between biomolecules present on the particles surface.

In colloidal system the second virial coefficient B_2 contains information on the interaction potential between colloidal particles. In section 3.1 we show how to obtain B_2 value from Static Light Scattering and Dynamic Light Scattering measurements. In section 3.2 we study the second virial coefficient of charged particles, in order to quantify the electrostatic potential and the electric charge of the particles. In agreement with the literature we find that in colloidal system the charges involved in the particles interactions are different from the structural charges present on the particles surface (section 3.3). In section 3.4 we discuss the second virial coefficient expected in colloidal system with particles interacting via "Sticky Hard Sphere" potential . To bridge the biomolecular binding coefficient K_n (or the dissociation constant K) with the measured scattering intensity, we determined the relationship between B_2 and K. We evaluated the sensibility of our experimental technique in determining molecular dissociation constant and we found we are able to study weak interaction such as carbohydrate-carbohydrate ones (see section 3.6).

In chapter 4 we firstly illustrate experimental results in suspensions of particles with repulsive electrostatic interactions. From the measured second virial coefficient we extracted the charge of the particles. We determined two different experimental conditions under which particles interact as Hard Sphere. The determination of Hard Sphere condition is preliminary to the study of attractive interactions since residual electric repulsion could impair the detection of other, more subtle, interactions. The Hard Sphere limit could be achieved both by screening charges through ionic strength and by adding to particles surface a surfactant charged of opposite sign respect to the colloids. We decided to use our colloidal-based detector to study carbohydrate-carbohydrate interactions. Despite they play a crucial role in many cellular processes, carbohydrate interactions are very weak and difficult to detect and quantify. In section 4.2 we present some preliminary measurements on carbohydrate coated particles. In agreement to previous literature we have detected attractive interaction between carbohydrate-coated colloids when Calcium ions are present in the dispersion.

3 Study of interactions through second virial coefficient formalism

3.1 Virial coefficient from diffuse light experiments

The state equation for an ideal gas is:

$$PV = Nk_BT,$$

with N number of molecules. When the ideality conditions are not satisfied, the state equation can be rewritten as an expansion in power of the number density N/V:

$$\frac{P}{k_BT} = \frac{N}{V}\left(1 + B_2(T)\frac{N}{V} + B_3(T)\left(\frac{N}{V}\right)^2 + \dots\right). \tag{3.1}$$

The expansion coefficients are called virial coefficients. In particular the second virial coefficient B_2 is given by:

$$B_2 = -\frac{1}{2}\int d\boldsymbol{r}(e^{-\frac{V(\boldsymbol{r})}{k_BT}} - 1). \tag{3.2}$$

B_2 is thus a quantity directly related to the two-bodies interaction potential $V(\boldsymbol{r})$ between gas molecules. If the interaction is attractive B_2 assumes negative values, while in presence of repulsive potentials B_2 is a positive quantity. B_2 has the dimensions of a volume.

The same approach can be used for the description of dilute colloidal solutions. In this case $V(\boldsymbol{r})$ is the two-bodies interaction potential between colloids. Thus the knowledge of B_2 reveals information on the particles interaction. Higher order terms can be neglected in most situations. Indeed in dilute system higher orders in density expansion are neglectable being the density a small quantity.

Moreover the coefficients $B_3, B_4 \ldots$ account for three-body, four-body...interactions that in dilute system are rare. Thus Equation 3.2 can be truncated at the second term. In colloidal science it could be interesting to develop methods for determining experimentally B_2 and thus to evaluate the interaction potential between particles.

Light scattering techniques are widely used in the characterization of colloids since they allow to obtain information on the samples in a non-invasive way. In this thesis we studied how to obtain second virial coefficient from light scattering measurements. As introduced in chapter 2, the intensity of the diffuse light in the forward direction is proportional to the mean square fluctuation of dielectric constant [34]:

$$I \propto \frac{\left\langle \delta\epsilon_r^2 \right\rangle}{\lambda^2} \tag{3.3}$$

where λ is the light wavelength in vacuum. In general $\left\langle \delta\epsilon_r^2 \right\rangle$ depends on the fluctuations due to the solvent and those due to the variations in solute concentration $\left\langle \delta c_r^2 \right\rangle$, where c is the mass concentration per solute unit volume. From the theory of fluctuations:

$$\left\langle \delta c_r^2 \right\rangle = \frac{k_B T}{V_s} \frac{1}{\chi_T} c = \frac{k_B T}{V_S} \frac{1}{\frac{\partial \pi}{\partial c}} c,$$

where T is the absolute temperature, k_B is the Boltzmann's constant, V_s is the scattering volume and χ_T is the coefficient of isothermal compressibility. The second equality follows from the definition of isothermal compressibility $\chi_T = \frac{\partial \pi}{\partial c}$, with π osmotic compressibility. π can be expressed through a virial expansion in function of the concentration c, in analogy with Equation 3.2. Thus the intensity diffused by a colloidal dispersion can be rewritten to explicitly shows the second virial coefficient B_2:

$$I = \frac{Kc}{\frac{1}{M_0} + \frac{2B_2}{M_0^2 c}},$$

where M_0 is the molecular mass and K is a constant that for vertically polarized light has the value:

$$K = \frac{4\pi^2 n^2}{N_A \lambda^4} \left(\frac{\partial n}{\partial c} \right).$$

Hence the diffuse intensity results:

$$I = KcM_0 \left(1 + \frac{2B_2}{M_0} c \right)^{-1}. \tag{3.4}$$

In [35] an equation which relate the diffuse intensity to the particles mass is reported:

$$I = KM_0c. \tag{3.5}$$

To account for particles interactions an apparent mass M can be defined [35]:

$$M = M_0 \left(1 + \frac{2B_2}{M_0}c\right)^{-1}. \tag{3.6}$$

and accordingly an equation similar to Equation 3.4 can be written:

$$I = KcM = \frac{KM_0c}{1 + \frac{2B_2}{M_0}c} = \frac{KM_0c}{1 + k_Ic} = \frac{I_0c}{1 + k_Ic}, \tag{3.7}$$

with

$$k_I = \frac{2B_2}{M_0}. \tag{3.8}$$

When studying the light diffused by colloidal dispersion it is more convenient to express the scattered intensity as a function of the volume fraction ϕ defined as:

$$\phi = \frac{Nv_P}{V}$$

where N is the particles number, v_P is the volume of each particle and V is the total volume of the colloidal dispersion. c and ϕ are directly proportional and the proportionality constant is the particle density d. Thus Equation 3.7 can be rewritten as:

$$I = \frac{KM_0d\phi}{1 + k_Id\phi} = \frac{Kv_P\phi}{1 + k_I'\phi} \tag{3.9}$$

with

$$k_I' = k_I\rho = \frac{2B_2}{v_P}. \tag{3.10}$$

Hence from a static light scattering experiment the second virial coefficient can be extracted through Equation 3.9 by knowing the particles volume fraction and the volume of each particles. Through this treatment we found a relationship between the scattered intensity and the second virial coefficient. The former argument applies to static light scattering.

When considering Dynamic Light Scattering experiments we need to write a relationship for the diffusion coefficient of interacting particles analogous to Equation 3.6 for the mass. A collective

diffusion coefficient D can be defined as linearly dependent on the colloids concentration:

$$D = D_0(1 + k_D c), \tag{3.11}$$

where D_0 is the diffusion coefficient of non-interacting particles. The coefficient k_D is related to the second virial coefficient by the following relation:

$$k_D = \frac{2B_2}{M_0} - k_f. \tag{3.12}$$

k_f is not unambiguously defined. A general expression is:

$$k'_f = k_f \rho = k'_{f0} + \int_0^\infty dx F(x) \left[1 - e^{-\frac{V(x)}{k_B T}}\right], \tag{3.13}$$

where the term k'_{f0} is related to the hard sphere potential while F(x) can be defined in different way [36]. According to [35, 37] we assumed:

$$\begin{aligned} k'_{f0} &= 6.55 \\ F(x) &= 11.89(1 + x) + 0.706 - 1.69(1 + x)^{-1}. \end{aligned} \tag{3.14}$$

3.2 Virial coefficient of charged particles

As introduced in subsection 1.3.1, around charged particles there is an electric double layer, which guarantees a repulsive interaction between particles preventing colloidal collapse. Indeed a charged sphere in an electrolyte solution produces ions redistribution around its surface: the counterions are attracted in proximity of the particles while the coions are pushed away. On complex the solution is neutral. All the ions dissolved in the solution, such as all the colloidal particles, undergo Brownian motion.

By studying the second virial coefficient of a colloidal system with an electrostatic repulsive interaction between the particles, it is possible to determine the surface charge of the colloids, which is related to the surface potential ψ_s through Poisson-Boltzmann equation. In the case of plane symmetry, the Poisson-Boltzmann equation describing the potential in an electrolyte solution can be exactly solved. Instead, in presence of spherical symmetry, just an analytical solution can be obtained. The Poisson-Boltzmann equation for a symmetric electrolyte is given by [11]:

$$\frac{1}{r^2}\frac{\partial}{\partial r} r^2 \frac{\partial \psi}{\partial r} = \frac{2ezn_b}{\epsilon\epsilon_0} sinh\left(\frac{ez\psi}{k_B T}\right), \tag{3.15}$$

where ϵ and ϵ_0 are the solvent ad vacuum dielectric constant respectively, e is the electron charge and z is the electrolyte valence.

Loeb, Overbeek and Wiersema [38] published a numeric treatment of spherical system in z-z electrolyte solution, showing that the surface charge density can be expressed as:

$$q = \frac{Q}{4\pi a^2} = \frac{\epsilon\epsilon_0 k_B T}{ez}\kappa \left[2sinh\left(\frac{1}{2}\Psi_S\right) + \frac{4}{\kappa a}tanh\left(\frac{1}{4}\Psi_S\right)\right], \tag{3.16}$$

with a particles radius and $\kappa^{-1} = \lambda_D$, with λ_D Debye length. Ψ_S is the adimensional potential on the sphere surface and is given by:

$$\Psi_S = \frac{ez\psi_s}{k_B T}, \tag{3.17}$$

where ψ_s is the potential on the sphere surface solving Poisson-Boltzmann equation. The knowledge of the surface potential ψ_s is thus necessary to determine the charge of the sphere in solution.

Two spherical particles in a symmetric electrolyte solution experience a repulsive force due to their screened charges. Since the spherical geometry is more complex than the plane one, an exact analytic formula for the interaction potential can not be written. A possible approximation is the Derjaguin approximation, which is valid when the distance h between the two spheres is small in comparison with their radius a [39]. Under these conditions, the elements on each particle surface interact as they would be on two parallel planes; the total interaction can be calculated as the sum of all the infinitesimal contributions. However, when $h < \lambda_D$ this approximation is not valid anymore. In this case it's worthwhile considering the potential energy Φ associated to the repulsive interaction:

$$F = -\frac{\partial \Phi}{\partial h}. \tag{3.18}$$

By regarding Φ as due to the superposition of electric potentials of two isolate spheres the following equations are obtained:

$$\begin{aligned} F &\approx \pi\epsilon\epsilon_0 \left(\tfrac{k_B T}{ze}\right)^2 \Psi_S^2 \tfrac{1+\kappa(h+2a)}{(h/2a)+1} e^{-\kappa h} \\ \Phi &= 4\pi\epsilon\epsilon_0 \left(\tfrac{k_B T}{ze}\right)^2 \tfrac{a^2}{h+2a}\Psi_S^2 e^{-\kappa h}. \end{aligned} \tag{3.19}$$

Hence through the knowledge of the second virial coefficient obtained by scattering experiments, it is possible to evaluate the amplitude of the interaction potential; in the case of electrostatic repulsive interaction also the particles surface charge can be evaluated.

3.3 Charge renormalization

The Debye-Huckel approximation to solve Poisson-Boltzmann equation is valid within the limit of low interaction. When the charge on particles surface grows, the Debye-Huckel approximation fails to give exact solutions to the problem. It has been shown [40, 41] that, in the case of highly charged particles, Debye-Huckel approximation can already be used by substituting to the structural particles charge Z an effective charge Z_{eff}. Z_{eff} is obtained by considering the counterions cloud surrounding the particles and the particle itself as a unique entity. Since the counterions screen part of the particle charge results $Z_{eff} < Z$.

Consider a dispersion of spherical highly charged colloids with radius a and surface charge Ze, with e electron charge. We call ϵ the solvent dielectric constant, T the absolute temperature and c_s the electrolyte concentration in the solution. The system is characterized by a Bjerrum length:

$$\lambda_B = \frac{\beta e^2}{\epsilon}; \tag{3.20}$$

λ_B indicates the minimum distance between dissociate charges. As introduced in subsection 1.3.1, when charged colloids are regarded, each particles is surrounded by a spatial region forbidden to other particles due to electrostatic repulsion. Hence, by analogy with solid state physics, it is possible to define around each particle a Wigner-Seitz cell: the cell has null net charge and assumes the same symmetry of the colloid, in this case spherical symmetry. The radius of the Wigner-Seitz cell R is so defined that the ratio $(a/R)^3$ is the colloidal volume fraction. The Poisson-Boltzmann equation and the relative boundary conditions for the mean electrostatic field $\Phi(r)$ can be written for the Wigner-Seitz cell (Φ has been multiplied for βe to be adimensional):

$$\begin{aligned} &\nabla^2\Phi(r) = \kappa_{res}^2 sinh\Phi(r) && a < r < R \\ &\boldsymbol{n}\cdot\nabla\Phi(r) = \tfrac{Z\lambda_B}{a^2} && r = a \\ &\boldsymbol{n}\cdot\nabla\Phi(r) = 0 && r > a \end{aligned} \tag{3.21}$$

where $\boldsymbol{n}$ is the outgoing unit vector normal to the surface and κ_{res} is the inverse of the screening length defined in terms of the ionic strength: $\kappa_{res} = 8\pi\lambda_B c_s$. The first boundary condition assures the constance of the surface charge; the second condition fixes the electroneutrality of the cell. It can be shown [41] that the Yukawa potential (see Equation 1.3) can be written as:

$$\beta v(r) = Z_{eff}^2 \lambda B \left(\frac{e^{-k_{PB}a}}{r}\right), \tag{3.22}$$

namely it maintains the same shape of the traditional potential but the charge Z and the screening length κ_{res} are substituted respectively by the effective charge Z_{eff} and by κ_{PB}, the inverse of the screening length of the macroions on the Wigner-Seitz cell border defined as:

$$\kappa_{PB} = 4\pi\lambda_B(n_+^R + n_-^R) = \kappa_{res} cosh\Phi_R. \tag{3.23}$$

Hench, even in presence of highly charged colloids, the electrostatic interaction can be represented through a Yukawa potential, which has an easy form.

The effective charge Z_{eff} can be determined through the following expression [41]:

$$Z_{eff} = \frac{tanh\Phi_R}{\kappa_{PB}\lambda_B}\left\{\left(\kappa_{PB}^2 aR - 1\right) sinh\left[\kappa_{PB}(R-a)\right] + \kappa_{PB}(R-a) cosh\left[\kappa_{PB}(R-a)\right]\right\} \tag{3.24}$$

which explicitly shows the Z_{eff} dependence on the surface potential Φ_R, on the particle radius a and on the inverse of the screening length. The effective charge can thus be calculated by solving Poisson-Boltzmann equation to obtain Φ_R and by substituting Equation 3.23 in Equation 3.24.

3.4 Second virial coefficient for attractive particles

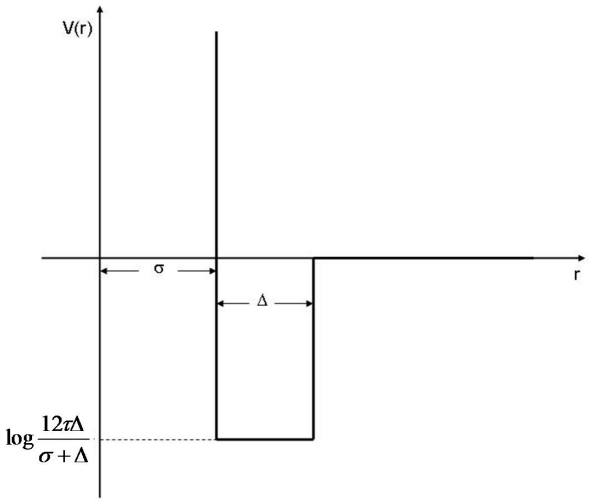

Figure 3.1: Sticky hard sphere potential.

The interaction between two spherical particles that attract at small distance while do not interact at large distance can be schematized through a Sticky Hard Sphere potential (SHS), sketched in Figure 3.1. The infinite repulsive barrier at $r = \sigma = 2a$, with a spheres radius, is due to the fact that the

particles are hard spheres, i.e. they can not compenetrate. The attractive region is modeled through a hole whose width tends to 0 as its depth tends to infinity. For higher distances the potential is null, i.e. the spheres do not interact. The SHS potential can be expressed as [42, 43]:

$$\frac{V(r)}{k_B T} = \begin{cases} +\infty & 0 < r < \sigma \\ log\frac{12\tau\Delta}{\sigma+\Delta} & \sigma < r < \sigma + \Delta \\ 0 & r > \sigma + \Delta \end{cases} \tag{3.25}$$

The τ parameter, called stickiness parameter, accounts for the fact that the hole becomes deeper as it tightens. Moreover, by inserting Equation 3.25 for the potential in Equation 3.2, it is possible to calculate with analytical methods the second virial coefficient as a function of the τ parameter:

$$B_2 = \frac{1}{2}\left[\int_0^{\sigma} d^3r + 4\pi \int_{\sigma}^{\sigma+\Delta} dr r^2 \left(1 - e^{-log\frac{12\tau\Delta}{\sigma+\Delta}}\right)\right] \cong \frac{2}{3}\pi\sigma^3\left[1 - \frac{1}{4\tau}\right]$$

The second equivalence has been obtained by assuming $\Delta << \sigma$; the factor $\frac{2}{3}\pi\sigma^3$ is the excluded volume term, namely the hard sphere second virial coefficient:

$$B_2^{HS} = \frac{2}{3}\pi\sigma^3 \tag{3.26}$$

Thus, by modeling attractive interaction through the SHS potential of Equation 3.25, the second virial coefficient results:

$$B_2 = B_2^{HS}\left[1 - \frac{1}{4\tau}\right] \tag{3.27}$$

3.5 Second virial coefficient and dissociation constant

In chemistry the equilibrium constant K_n or more often the dissociation constant K are used to describe molecular interaction. Since we found how to extract the second virial coefficient from light scattering experiments, it is now necessary two find a relationship between B_2 and K to compare our results with those present in literature.

3.5.1 Equilibrium constant of a chemical reaction

A generic chemical reaction can be represented through the equation [44]:

$$\sum_{i=0}^{m} b_i B_i = 0 \tag{3.28}$$

where B_i is the i molecule of the reaction, b_i is the number of molecules involved in the chemical reaction and the summation extends to all the m interacting species. If both the volume V and the temperature T are held constant and the system is regarded as ideal, the variation of the Helmholtz free energy A can be expressed as a function of the chemical potential μ_i:

$$\Delta A = \sum_i \left(\frac{\partial A}{\partial N_i} \right)_{T,V,N} b_i = \sum \mu_i b_i.$$

At the equilibrium the free energy has a minimum and thus:

$$\Delta A = \sum \mu_i b_i = 0 \tag{3.29}$$

The chemical potential can be expressed as:

$$\mu_i = -k_B T ln \frac{\zeta_i}{N_i},$$

where ζ_i is the single molecule partition function and does not depend on the molecules number N_i. By substituting the expression of the chemical potential in Equation 3.29 the following equality is obtained:

$$\Delta A = -k_B T \sum_i b_i \left(ln\zeta_i - lnN_i \right) = \Delta A_0 + k_B T \sum_i b_i lnN_i = 0$$

where

$$\Delta A_0 = -k_B T \sum_i b_i ln\zeta_i.$$

The quantity ΔA_0 is called standard free energy variation of the reaction and depends only on the temperature and on the volume while does not depend on the number N_i of molecules of each species involved in the reaction. The equilibrium condition can thus be written as:

$$\sum_i lnN_i^{bi} = ln(N_1^{b1} N_2^{b2} ... N_m^{bm}) = -\frac{\Delta A_0}{k_B T}.$$

The equilibrium constant K_N is defined as:

$$K_N \equiv e^{-\frac{\Delta A_0}{k_B T}} \tag{3.30}$$

and accordingly the mass action law results:

$$N_1^{b1} N_2^{b2} ... N_m^{bm} = K_N(T, V).$$

Since ΔA_0 depends only on the temperature and on the volume, also K_N depends only on these two variables and does not depend on N_i.

If the known quantity is not the number of molecules in the solution but rather their density $n_j = \frac{N_j}{V}$ the chemical potential results:

$$\mu_i = -k_B T ln \frac{\zeta_i'}{n_i},$$

where

$$\zeta_i'(T) = \frac{1}{V}\zeta_i(V,T).$$

In this case the equilibrium condition can be written as:

$$n_1^{b1} n_2^{b2} ... n_m^{bm} = K_n(T). \tag{3.31}$$

The equilibrium constant K_n depends only on the temperature and is related to K_N through the equality:

$$K_n(T) = \frac{1}{V^b} K_N(T,V), \tag{3.32}$$

where $b = \sum_{i=1}^{m} b_i$.

If in the solution there are only molecules of one species which interact to form dimers the former relation becomes:

$$K_n(T) = V K_N(T,V).$$

Since K_N is an adimensional constant, K_n has the dimensions of a volume.

3.5.2 Relationship between equilibrium constant and second virial coefficient

We consider now a reaction in which a unique molecular species is involved and the interacting molecules form dimers. The reaction can be schematized as:

$$A + A \rightleftharpoons AA. \tag{3.33}$$

The equilibrium constant K_n is defined as:

$$K_n = \frac{n_D}{n^2}.$$

where n and n_D indicates the molecules and dimers number density. However to describe molecular interaction it is more often used the dissociation constant K defined as the inverse of the equilibrium constant:

$$K = \frac{n^2}{n_D}.$$

Since the constant K is usually expressed in moles per liter (Molar) it is necessary to divide both n and n_D for the Avogadro's number N_A obtaining:

$$K = \frac{n^2}{n_D N_A}. \tag{3.34}$$

Small dissociation constants (of the order of mM) indicate an high interaction degree between the molecules while high K value indicate high dissociation.

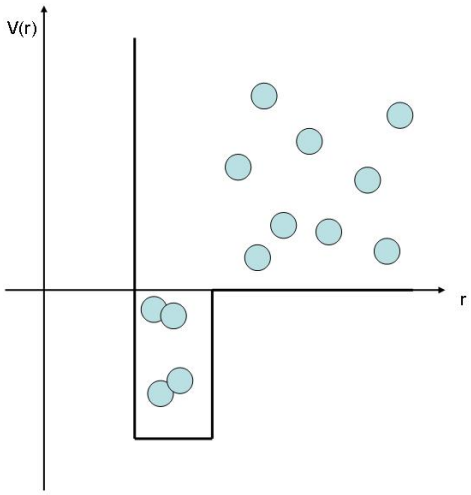

Figure 3.2: Schematic representation of dimer formation in presence of a sticky hard sphere potential.

To find a relationship between K, the quantity used in chemistry to evaluate molecular interactions, and B_2, which can be measured with light scattering experiments, it is necessary to find an expression for the dimer density n_D. The interaction potential between the molecules can be described as a Sticky Hard Sphere potential (see section 3.4). Accordingly the dimer can form when $\sigma < r < \sigma + \Delta$, i.e. the distance between the molecules is included between the width σ of the repulsive region and the largeness Δ of the attractive hole (see Figure 3.2). The probability to find two molecules inside those region is given by the integral of the radial distribution function $g(r)$ between

σ and $\sigma + \Delta$:

$$\int_{\sigma}^{\sigma+\Delta} d^3\boldsymbol{r} g(\boldsymbol{r}).$$

To obtain the density of dimers in solution it's necessary to multiply the former equation for the square particle density n^2 and to divide by two not to count particles twice:

$$n_D = \frac{n^2}{2} \int_{\sigma}^{\sigma+\Delta} d^3\boldsymbol{r} g(\boldsymbol{r}).$$

In dilute system the radial distribution function $g(\boldsymbol{r})$ can be written as:

$$g(\boldsymbol{r}) \cong e^{-\frac{V(\boldsymbol{r})}{k_B T}},$$

where $V(\boldsymbol{r})$ is the particles interaction potential. Thus the dimer density results:

$$n_D = \frac{n^2}{2} \int_{\sigma}^{\sigma+\Delta} d^3\boldsymbol{r} e^{-\frac{V(\boldsymbol{r})}{k_B T}}. \tag{3.35}$$

By considering a Sticky Hard Sphere potential, with stickiness at contact, the virial coefficient results:

$$B_2 = -\tfrac{1}{2} \int d^3r (e^{-\frac{V(r)}{k_B T}} - 1) =$$

$$= \tfrac{1}{2} \left[\int_0^{\sigma} (1 - e^{-\frac{V(\mathbf{r})}{k_B T}}) d^3\mathbf{r} + \int_{\sigma}^{\sigma+\Delta} (1 - e^{-\frac{V(\mathbf{r})}{k_B T}}) d^3\mathbf{r} + \int_{\sigma+\Delta}^{\infty} (1 - e^{-\frac{V(\mathbf{r})}{k_B T}}) d^3\mathbf{r} \right] =$$

$$= \tfrac{2}{3}\pi(\sigma + \Delta)^3 - \int_{\sigma}^{\sigma+\Delta} e^{-\frac{V(\mathbf{r})}{k_B T}} d^3\mathbf{r}$$

If the interaction range is much smaller than the hard sphere range ($\sigma >> \Delta$) it can be assumed $\frac{2}{3}\pi(\sigma + \Delta)^3 \cong \frac{2}{3}\pi\sigma^3 = B_{HS}^2$. Hence it can be evaluated the difference:

$$\Delta B_2 = B_{HS}^2 - B_2 = \int_{\sigma}^{\sigma+\Delta} e^{-\frac{V(\mathbf{r})}{k_B T}} d^3\mathbf{r}. \tag{3.36}$$

By substituting Equation 3.36 into Equation 3.35, the dimer density, in dilute solution, is directly proportional to the second virial coefficient variation respect to hard sphere B_2^{HS}. By recalling Equation 3.34, the dissociation constant can be related to ΔB_2:

$$K = \frac{2}{N_A \Delta B_2} = \frac{4}{v_P N_A \Delta k_I'}, \tag{3.37}$$

where k_I' is the coefficient which can be evaluated through light scattering experiments $k_I' = 2B_2/v_P$.

Equation 3.37 indicates that K becomes smaller as the potential becomes more attractive.

3.6 Sensibility

We evaluated the sensibility of the proposed method for measuring dissociation constants. In static light scattering measurements we have a sensibility on $\Delta k'_I$ of the order of unit; since $K = 4/(V_P N_A \Delta k'_I)$ (with V_P expressed in liter since K is in Molar units) we can measure dissociation constants of the order of $10\,\mu M$.

However in our experiments we measure the dissociation constant K between the functionalized colloidal particles. To compare our measurement results with the values present in the literature for molecular dissociation constants, we have to evaluate the relationship between K of the colloids and K_m of the biomolecules arranged on particles surface. According to [2], the equilibrium constant K_{eq} depends on temperature T through the van't Hoff relation

$$K_{eq} = e^{-\frac{\Delta G_c^0}{RT}},$$

where ΔG_c^0 is the standard Gibbs free energy of the reaction between colloids. If the colloids in a pair are attached by N_l links

$$\Delta G_c^0 = N_l \Delta G^0,$$

where ΔG^0 is the standard Gibbs free energy for each link. This treatment neglects the numerous combinations with which N links can be made between two colloids, each bearing N_{tot} sticky links. According to [2] we also neglect the change of rotational entropy of the colloids upon aggregation. The former equations demonstrate the great potentiality of our colloidal-based detector: by incrementing the density of sticky ends on particles surface we obtain a largely enhanced sensibility on evaluating molecular dissociation constant.

As described in subsection 1.4.1, the number of links N_l can be estimated with a geometric approach through the formula:

$$N_l = \frac{2\pi R_0}{L}(L-h)^2\Gamma, \tag{3.38}$$

where Γ is the particle surface density of strands, R_0 is the colloids radius, h is the length of the impenetrable coating layer while the difference $L-h$ is the length of the sticky ends of the molecules. By substituting all the parameters with those corresponding to our experimental samples we obtain that we are able to detect very weak molecular interactions with K_m of the order of M.

4 Experimental results of biomolecular interactions

4.1 Determination of particles charge

PFR94 particles, being charged, experience a repulsive electrostatic interaction and thus to compute their interaction potential it is necessary to know the particles charge. We have determined the second virial coefficient from light scattering experiments for different samples presenting repulsive interaction between the colloids and, following the procedure shown in section 3.2, we have determined the value of the particle charge. Since the effective charge, namely the charge that take parts to interaction, can be different from the structural charge present on particles surface, as described in section 3.3, we have analyzed our data to extract both structural and effective charge values. The effective charge have been determined with both static and dynamic light scattering experiments.
We decided to study the value of the particles charge by coating their surface with the non-ionic surfactant $C_{12}E_5$. All the experiments have been performed at the same temperature (T=30 C).

4.1.1 Effective charge from static light scattering measurements

We initially considered a solution of PhP coated with $C_{12}E_5$ surfactant in NaCl $1\,mM$. We studied the intensity of the $90°$ diffuse light as a function of the particles volume fraction ϕ, here reported in Figure 4.1. As it can be recognized from the graph, at low particles volume fractions, the curve trend is linear, since the particles are too dilute to experiments any interaction. Instead, as ϕ grows, the trend becomes non-linear. According to the treatment proposed in section 3.1 we fitted the curves through the function:

$$I = \frac{I_0\phi}{1 + k'_I\phi} + c \tag{4.1}$$

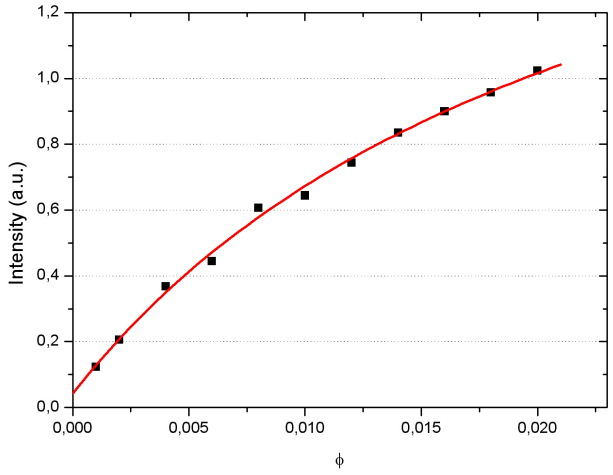

Figure 4.1: 90° diffuse light intensity for a PhP sample coated with $C_{12}E_5$ surfactant in a ionic strength $I = 1\,mM$ NaCl. Black squares are the experimental points while the red line is the fit obtained through Equation 4.1

where the constant c has been added to account for impurities scattering. From the fit we obtained

$$k'_I = 33.35 \tag{4.2}$$

which corresponds to a second virial coefficient

$$B_2 = \frac{k'_I v_P}{2} = 1.88 \cdot 10^{-21}\, m^3 \tag{4.3}$$

The volume of the particles have been calculated by assuming particles radius $R = 30\,nm$, the value measured with dynamic light scattering on a sample of bare PhP with $\phi = 0.001$, namely with sufficiently dilute particles to experience interactions.

It's worthwhile noticing that in absence of attractive interaction and with completely screened charges the interaction between the colloids is of excluded volume type. Since in this situation

$$B_2 = \frac{2}{3}\pi\sigma^3$$

with $\sigma = 2R$, k'_I assumes the value

$$k'^{HS}_I = \frac{2B_2}{v_P} = \frac{2\frac{2}{3}\pi\sigma^3}{\frac{4}{3}R^3} = 8 \tag{4.4}$$

Thus by comparing Equation 4.2 with Equation 4.4 we deduce that the ionic strength $I = 1\,mM$ NaCl of the dispersion is not enough to screen charges, since there is a strong repulsive interaction.

As described in details in section 3.2, in presence of electrostatic repulsive interaction, it's possible to determine the electrostatic potential and the particles charge from B_2 value . We realized an algorithm with *Mathematica* which allows to determine the superficial charge of the particles corresponding to a certain B_2 value. The algorithm proceeds as follows. Since

$$B_2 = -\frac{1}{2}\int d^3h \left(e^{-\frac{V(h)}{k_B T}} - 1\right)$$

where the interaction potential V as function of the particles distance h is given by

$$V(h) = 4\pi\varepsilon\varepsilon_0 \left(\frac{k_B T}{ze}\right)^2 \frac{a^2}{h+2a}\,\Psi_s^2\, e^{-\kappa h},$$

from the knowledge of B_2 the potential Ψ_s can be estimated, where Ψ_s is assumed to be the superposition of single particle potentials. From the value of Ψ_s the particle charge is determined through the equation:

$$q = \frac{Q}{4\pi a^2} = \frac{\epsilon\epsilon_0 k_B T}{ez}\kappa \left[2sinh\left(\frac{1}{2}\Psi_S\right) + \frac{4}{\kappa a} tanh\left(\frac{1}{4}\Psi_S\right)\right]. \tag{4.5}$$

The effective charge for $C_{12}E_5$ coated particles in ionic strength $1\,mM$ NaCl is

$$q = 230\,e,$$

with e elementary charge.

We have thus varied the solution ionic strength: static light scattering data for PhP coated with $C_{12}E_5$ in NaCl $10\,mM$ and NaCl $50\,mM$ are shown in Figure 4.2 and Figure 4.3 respectively. The experimental data curve (90° diffused intensity vs. particles volume fraction) approaches to a linear trend indicating an Hard Sphere type interaction between the particles.

From the fit of the sample with NaCl $10\,mM$ we obtained

$$k_I' = 12.46,$$

corresponding to a virial coefficient

$$B_2 = 7.14 \cdot 10^{-21}\, m^3$$

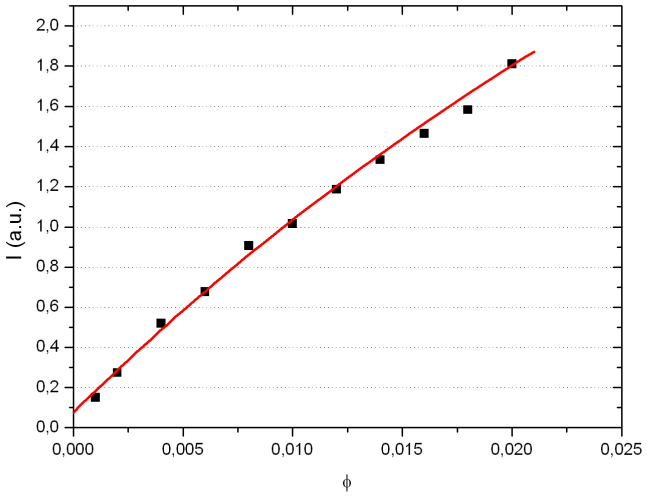

Figure 4.2: 90° diffuse light intensity for a PhP samplecoated with $C_{12}E_5$ surfactant in a ionic strength $I = 10\,mM$ NaCl. Black squares are the experimental points while the red line is the fit obtained through Equation 4.1

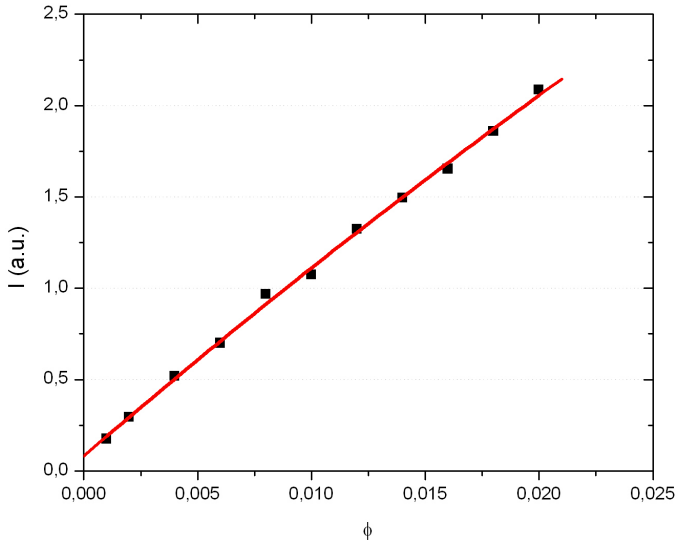

Figure 4.3: 90° diffuse light intensity for a PhP sample coated with $C_{12}E_5$ surfactant in a ionic strength $I = 50\,mM$ NaCl. Black squares are the experimental points while the red line is the fit obtained through Equation 4.1

and to an effective charge

$$q = 400e.$$

These results are in agreement with renormalization charge theory which predicts an augment of the effective charge by incrementing the solution ionic strength.

By fitting data of Figure 4.3 ($I = 50\,mM$) results

$$k'_I = 4.45;$$

in this situation $k'_I < k'^{HS}_I = 8$ indicating a partially attractive interaction. For this reason is not possible to extract a value for the effective charge.

4.1.2 Effective charge from dynamic light scattering measurements

The effective charge can be estimated also through Dynamic Light Scattering measurement. We prepared samples of PhP+$C_{12}E_5$ in NaCl $1\,mM$ at various particles volume fraction ϕ. We measured the diffusion coefficient D and we plotted D vs. ϕ (Figure 4.4). In this case, according to the treatment

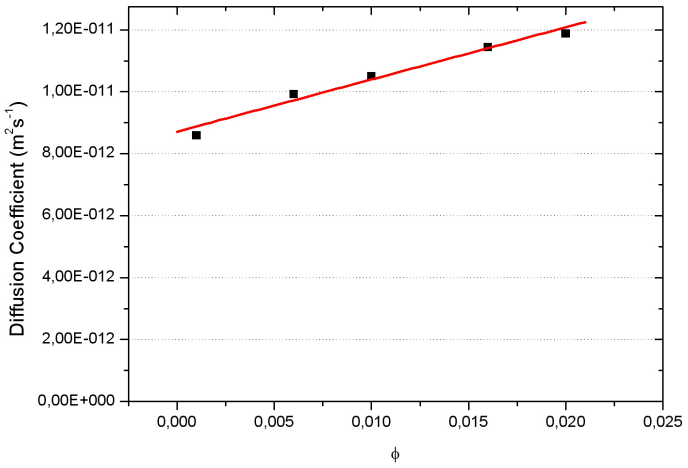

Figure 4.4: Diffusion coefficient vs. particles volume fraction for samples of PhP+$C_{12}E_5$ in NaCl $1\,mM$.

developed in section 3.1, we fitted the data with the function

$$D = D_0(1 + k'_D\phi), \tag{4.6}$$

where k'_D is related to the second virial coefficient as follows:

$$k'_D = \frac{2B_2}{v_P} - k'_{f0}. \tag{4.7}$$

From data of Figure 4.4 we extracted the value

$$k'_D = 17.26$$

With a *Mathematica* program similar to that realized to analyze Static Light Scattering data, we determined the effective particles charge, which in this case results

$$q = 220e.$$

The effective charge values obtained with the two methods are in agreement. We performed Dynamic Light Scattering measurements also on sample of PhP+$C_{12}E_5$ in NaCl $10\,mM$ and $50\,mM$ at various particles volume fraction. The data are reported in Figure 4.5. In the case of NaCl $10\,mM$ we

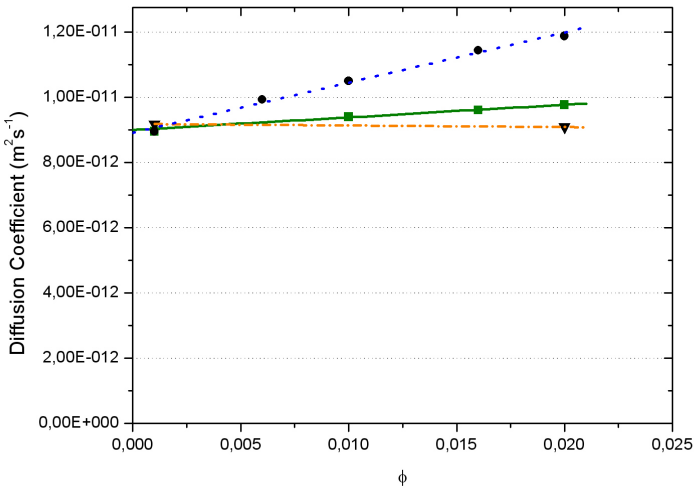

Figure 4.5: Diffusion coefficient vs. particles volume fraction for samples of PhP+$C_{12}E_5$ in NaCl $10\,mM$ (green line fit) and $50\,mM$ (red line-dot fit). Black dots with the corresponding blue dot fit curve are the $1\,mM$ data previously shown in Figure 4.4.

extracted an effective charge value

$$q = 430e,$$

in agreement with the value found through diffuse light measurement of $400e$. The k'_D coefficient ob-

tained from $50\,mM$ samples has a negative value, confirming the previously found result of partially attractive interaction between the particles.

4.1.3 Structural charge

To determine the structural charge of the PhP we used the surfactant $HTAB$, which is positively charged. We prepared solutions of PhP partially coated with $C_{12}E_5$ in NaCl $1\,mM$; with this solution we prepared different samples by adding various $HTAB$ concentrations, from $0.05\,mM$ to $0.4\,mM$. Since the particles are not fully coated with $C_{12}E_5$, the $HTAB$ can adsorb onto particles surface, each surfactant molecule bringing a positive charge.

We measured the diffusion coefficient D for each sample and we extracted the value of the coefficient k'_D. We studied both D and k'_D as function of the positive charges added to the solution. The data for k'_D are plotted in Figure 4.6. Both D and k'_D data exhibit a minimum: the presence of a min-

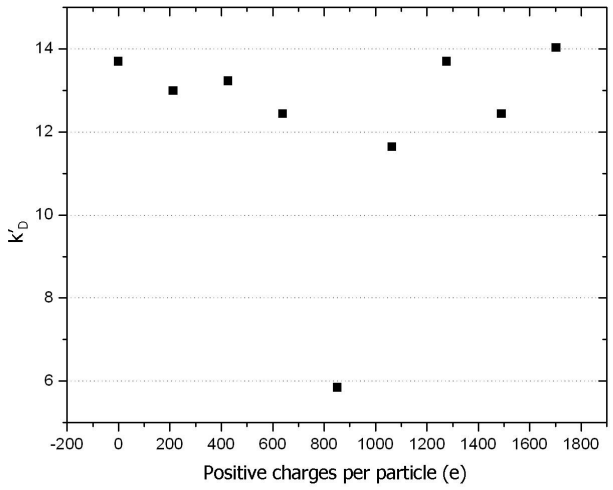

Figure 4.6: k'_D vs. positive charge per particle in elementary charge unit. k'_D have been obtained by studying the diffusion coefficient of samples of Php partially coated with $C_{12}E_5$ and with different concentration of $HTAB$.

imum indicates that, by adding $HTAB$, the particles charge is completely screened by the surfactant positive charges. The adsorption of other $HTAB$ molecules onto particles surface gives the same initial charge to the particles but of positive sign. The minimum of D and of k'_D is reached by adding a charge per particle of $850e$, which thus corresponds to the particles surface charge. This value is far different from that obtained by studying the diffuse light intensity and the diffusion coefficient for various particles volume fractions, described in the former sections. However while the previously

determined charges were the effective particles charges, namely those taking part in interaction phenomena, now we have evaluated the structural particles charge, i.e. the charge present on particles surface.

The values obtained for the particles effective charges ($q = 220e$ and $q = 230e$) do not agree with the predictions of the renormalization charge theory. Indeed, in Figure 4.7 is shown the renormalized charge vs. structural charge for different solution ionic strength: the effective charge corresponding to a structural charge of $800e$ is about $750e$.

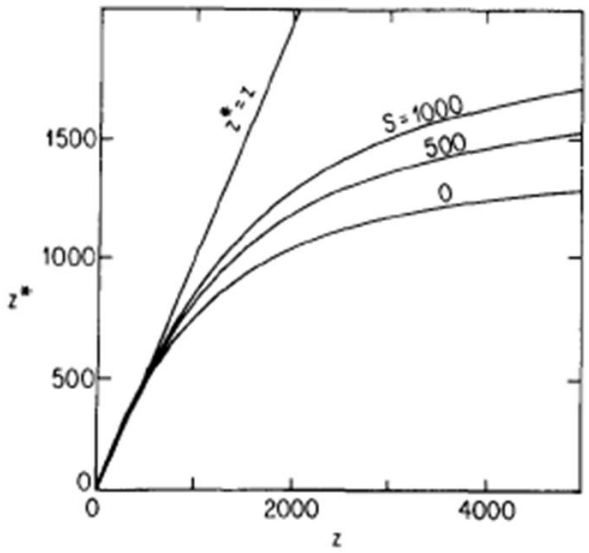

Figure 4.7: Effective charge vs. structural charge for various ionic strength.

Probably, the surface charge of the particles originates from the absorption of ions present in the solution. Indeed, there are no structural reasons for the presence of these charges. Thus we can suppose that the linking of $HTAB$ molecules on the particles promotes the absorption of other negative ions on the surface; in this way the estimated particles structural charge is higher than the value obtained if the $HTAB$ would not facilitate ions absorption. Hench, the charge on PhP is not univocal but depends on the molecules used to coat their surface. To verify this hypothesis we have studied the relation between effective and structural charge also on samples of PhP coated with the carbohydrate *Dodecyl-Alpha-D-Maltoside*, as described in the following section.

It is worthwhile noticing that we have reached the Hard Sphere condition both by incrementing electrolyte ionic strength and by adding the charged surfactant $HTAB$. The Hard Sphere condition is necessary to study carbohydrate-carbohydrate interaction since assures that no repulsive interaction is active.

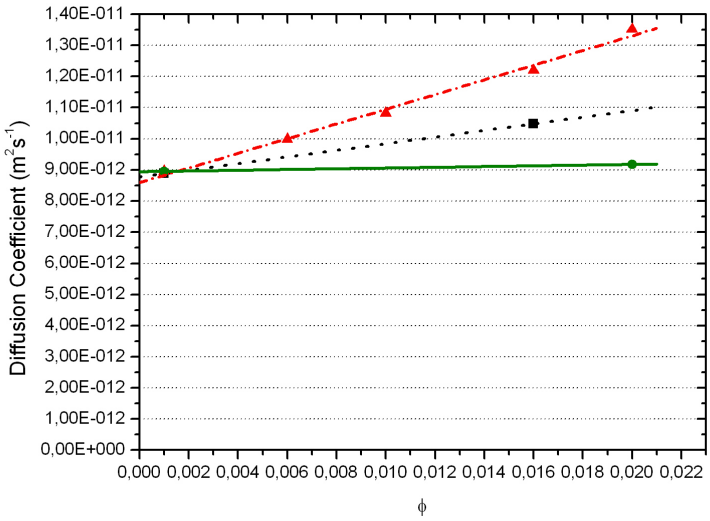

Figure 4.8: Diffusion coefficient vs. particles volume fraction for samples of PhPcoated with α-maltoside in NaCl $1\,mM$ (red), $10\,mM$ (blu), $50\,mM$ (green).

4.2 Preliminary measurements of carbohydrate-carbohydrate interactions

We coated the PhP with carbohydrate molecules of *n-Dodecyl-Alpha-D-Maltoside*, which should interact in presence of divalent ions. However to allow particles to experience attractive interaction we first extinguished electrostatic repulsive interaction, i.e. reached Hard Sphere condition.

4.2.1 Hard Sphere condition

We determined the Hard Sphere condition initially by gradually incrementing solution ionic strength and then by adding $HTAB$ molecules.

We prepared samples with different NaCl concentrations. In Figure 4.8 we report the diffusion coefficient D for various particles volume fractions in solution with ionic strength $1\,mM$, $10\,mM$ and $50\,mM$ NaCl. We fitted the experimental data with Equation 4.6 and we obtained the values reported in table 4.2.1.

Following the same procedures used for PhP coated with $C_{12}E_5$, from k'_D we determined the effective charge of the particles, finding for NaCl $1\,mM$ an effective charge of $500e$. By comparing this value with that obtained for particles coated with $C_{12}E_5$ ($q = 230e$) it results that particles coated with *n-Dodecyl-Alpha-D-Maltoside* experience an interaction determined by an higher charge. It's interesting noticing that in both cases of particles coated with $C_{12}E_5$ and with *n-Dodecyl-Alpha-D-*

[NaCl]	k'_D
$1\,mM$	29.58
$10\,mM$	12.12
$50\,mM$	0.655

Table 4.1: k'_D determined in samples of PhP coated with *n-Dodecyl-Alpha-D-Maltoside* for various ionic strengths.

Maltoside a ionic strength of $50\,mMNaCl$ makes $k'_D < k'^{HS}_D = 1.5$.
Also in the solution of PhP coated with carbohydrate molecules we have noticed that the repulsive interaction diminishes by incrementing solution ionic strength. The Hard Sphere condition is reached for $I \approx 50\,mM$.

The Hard Sphere condition have been obtained also through charge compensation by coating particles with $HTAB$ molecules. We prepared samples with PhP partially coated with *n-Dodecyl-Alpha-D-Maltoside*, starting from a volume fraction $\phi = 0.016$ in NaCl $1\,mM$ and with various $HTAB$ concentrations, from $0.05\,mM$ to $0.45\,mM$. Analogously to what done for particles coated with $C_{12}E_5$, we studied the behavior of D and of k'_D as a function of the $HTAB$ charges per particle in unit of the elementary charge e. The data for k'_D have been reported in Figure 4.9. Also in this

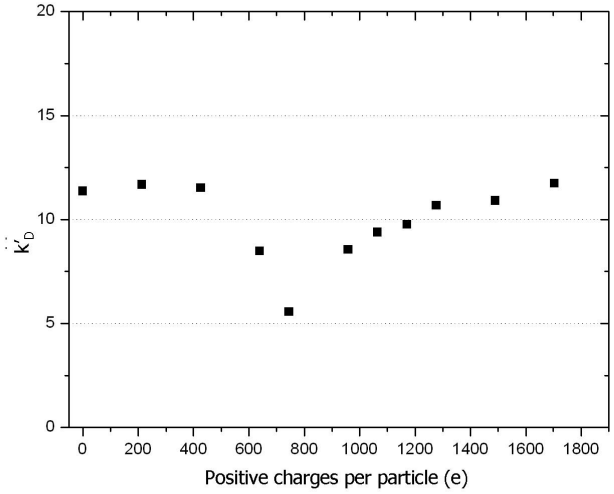

Figure 4.9: k'_D vs. positive charges per particle in elementary charge unit. k'_D have been obtained by studying the diffusion coefficient of samples of Php partially coated with *n-Dodecyl-Alpha-D-Maltoside* in NaCl $1\,mM$ and with different concentration of $HTAB$. The datum corresponding to an added charge of $850e$ is not present because we could not measure the diffusion coefficient since the particles collapsed.

case the k'_D curve presents a minimum at about $850e$: differently from the sample of $C_{12}E_5$ coated

particles, with carbohydrate coated particles we observed the collapse of the colloidal dispersion. This fact indicates that the interaction between the particles is different in the two analyzed situations.

In conclusion, also in the case of particles coated with *n-Dodecyl-Alpha-D-Maltoside* we have experimentally determined the Hard Sphere condition with the two methods of electrostatic screening (ionic strength $I = 50\,mM$ NaCl) and of charge compensation with $HTAB$. In this case the Hard Sphere condition is obtained with an $HTAB$ concentration of $0.15\,mM$, corresponding to a positive charge of $650e$ per particle.

4.2.2 Attractive Interaction

In order to obtain attractive interaction, we prepared a dispersion in which the particles interact through a Hard Sphere potential, namely PhP coated with *n-Dodecyl-Alpha-D-Maltoside* in NaCl $1\,mM$ and $HTAB$ $0.15\,mM$. We studied the diffusion coefficient at various particles volume fractions and we extracted the value for $k'_D = 6.86$. Since $k'^{HS}_D = 1.5$ in our samples particles experience a slightly repulsive interaction.

As reported in literature [4], carbohydrate-carbohydrate interaction is possible only in presence of divalent ions, in particular Calcium ions. For this reason we prepared samples by adding to the previously prepared dispersion (Php in NaCl $1\,mM$ and $HTAB$ $0.15\,mM$) various concentrations of $CaCl_2$. To determine the particles interaction we measured the diffusion coefficient. We found that for $CaCl_2$ concentrations lower than $12\,mM$, $k'_D > 1.5$ indicating that the particles do not interact attractively. Instead, for $CaCl_2$ concentration equal to $12\,mM$ we obtained $k'_D = -2.85$, which indicates the presence of an attractive interaction between the particles.

As a control, we prepared analogous samples with particles coated with $C_{12}E_5$: by adding $CaCl_2$ ions no attractive interaction takes place. This fact confirms that the attractive interaction is mediated by the carbohydrate molecular recognition.

Finally we added a solution of $EDTA$ to the samples where attractive interaction is present. $EDTA$ is a chelant molecule for Calcium ions: it means that when a solution contains molecules of $CaCl_2$ dissociated in divalent ions, each $EDTA$ molecule binds itself to a Calcium ion, preventing the possibility to the Calcium ion to link to other molecules. such as the carbohydrates.

As recognizable from data in Figure 4.10, by adding the $EDTA$ to the sample with attractive interaction, the dispersion dilutes and the diffusion coefficient assumes a value perfectly aligned along the line fitting the diffusion coefficient of the sample before adding both $CaCl_2$ and $EDTA$.

We have thus documented the possibility to inspect with light scattering techniques attractive interaction between carbohydrate molecules when the solution contains Calcium ions.

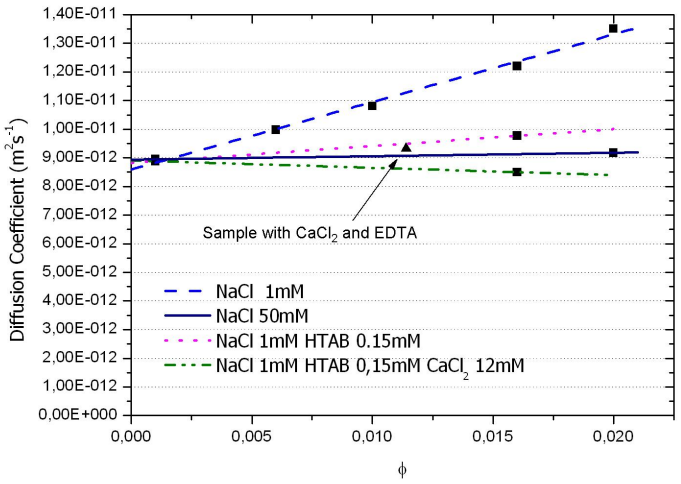

Figure 4.10: Diffusion coefficient vs. particles volume fraction in a solution of PhP + *n-Dodecyl-Alpha-D-Maltoside* in NaCl $1\,mM$.

Part II

Introduction

In the second part of this thesis we investigate previously undescribed phenomena taking place in bidisperse mixture of rod-sphere and sphere-sphere colloidal particles under the effect of an external oscillating electric field. Chapter 5 describes the behavior of various type of colloidal particles (dielectric, conductive, charged) under the action of an external electric field. In particular, when the particles are charged particles, the behavior of the dispersion strongly depends on the electric field frequency. The simplest regime can be found at high field frequencies where hydrodynamic and diffusional effects can be neglected and where charged particles can thus be assimilated to dielectric particles with a conductive skin. In this regime the colloidal polarizability can be described with the well known Maxwell-Wagner model. At low field frequencies instead, electrodynamic processes and solvent flows play a crucial role in determining the behavior of the particles. Within a linearized electrokinetic theory the phenomenon accounting for solvent flows in proximity of charged surface is the electro-osmosis, here described in section 5.4. Induced-Charge Electro-osmosis (ICEO) (section 5.5) refers instead to second order solvent flows which originate around conductive particles, where charges are not fixed but are induced by the electric field.

Section 6.1 reviews birefringence measurements results obtained on monodisperse mixture of rod-like particles and bidisperse mixture of rod-sphere colloids is proposed. Indeed, according to the theory proposed in chapter 5, rod-like particles orient preferentially parallel to electric field direction. However Mantegazza et al. [23] observed that when the rod-like particles are mixed with a sufficient concentration of smaller spherical particles, at low field frequency the rods display an anomalous orientation with the long axis perpendicular to the field direction. We performed Electric Transmitted Light Intensity measurements to study the scattering cross section of such systems and to acquire better insight into the physics of such phenomenon. Subsection 6.2.1 and subsection 6.2.2 present the experimental results for monodisperse suspension of rod-like particles and for mixtures of rods and spheres. Through our measurements we confirmed the phenomenon of anomalous orientation in bidisperse mixtures. Moreover in the same frequency range, we observed an overall field-induced clearing of the mixtures. In subsection 6.2.3 we demonstrate that such clearing effect can not be ascribed to the anomalous orientation of the rod-like particles but is related to a structuring of the secondary particles around the rods. In seeking a better explanation of these phenomena we found that the same field induced clearing is present also in mixture of large and small spheres, where no orientational effect is possible (section 6.3). Also in this case we found a decrease of the turbidity at low frequency. In subsection 6.3.1 we show that a repulsive interaction between large and small spheres can be responsible of such clearing effect. We conjecture that second order electro-osmotic flows can be responsible of all the observed phenomena (section 6.4) giving rise to a new electrokinetic phenomenon of “colloidal

concentration polarization" (section 6.5).

5 Colloidal particles in electric field

The behavior of colloidal dispersions under the effect of an external electric field is strictly determined by the dielectric properties of both the colloids and the suspending medium. In this chapter we propose a brief review of the phenomena occurring in different types of colloidal suspensions when an external electric field is applied.

5.1 Dielectric particles in dielectric medium

First of all we consider uncharged dielectric **spherical** particles immersed in a dielectric medium. In this case, due to the dielectric constant mismatch, a polarization charge arises at the particles/solvent interface. As the electric field is activated, polarization charges accumulate on the particle-solvent interface, thus making the particle's dipole moment to grow, either in the direction of the electric field or opposite to it. This yields a continuous electric displacement across the interfaces. The growth proceeds until a stationary condition is not established. The resulting polarizability can be calculated through the Clausius-Mossotti equation:

$$\alpha = 4\pi\epsilon_0\epsilon_s R^3 \frac{\epsilon_p - \epsilon_s}{\epsilon_p + 2\epsilon_s}, \tag{5.1}$$

where R is the particle's radius while ϵ_0, ϵ_p and ϵ_s are the vacuum, particle and solvent dielectric constant respectively.

In the case of **non-spherical** particles, due to the anisotropic shape, the induced particle dipole moment varies with the particle orientation with respect to the external electric field direction. Hence also the particle's energy is function of the particle's orientation. In the case of particles having dielectric constant higher than the solvent the field induced dipole moment is positive. Moreover when the particle is parallel to the external field direction the dipole moment is larger than the one in the

perpendicular configuration. As a consequence the parallel configuration is energetically favored. The same result can be found also for particles having dielectric constant lower than the solvent. In this case the dipole moment is negative and its absolute value is larger in the parallel configuration than in the perpendicular one. Thus dielectric particles orient preferentially parallel to the electric field direction.
Considering monodisperse colloidal solutions, the only exceptions to this behavior have been found in highly concentrated rods dispersions, where perpendicular orientation prevails [45, 46].

5.2 Dielectric and conductive particles in dielectric and conductive medium

When considering conductive dielectric particles immersed in conductive dielectric medium, the presence of an external electric field produces an induced polarization due to the conductivity and dielectric mismatch between the particles and the solvent. The polarization process can be described through the so called Maxwell-Wagner model. When the electric field is activated, free charges accumulate at the particles/solvent interface, producing a growth of the particle's dipole moment. The accumulated charges create a counterfield which opposes to the external one. This process continue until the field generated by the accumulated charges balances the conductivity mismatch between the particle and the solvent i.e. the internal current equals the external one.
For **spherical** particles, the polarizability can still by expressed through Equation 5.1, where ϵ_p and ϵ_s are the particles and solvent complex dielectric function respectively and can be written in terms of the real dielectric function ϵ' and of the volume conductivity K:

$$\begin{aligned} \epsilon_p &= \epsilon_p^{'} + i\frac{K_p}{\omega\epsilon_0} \\ \epsilon_s &= \epsilon_s^{'} + i\frac{K_s}{\omega\epsilon_0}. \end{aligned} \tag{5.2}$$

The polarizability of spherical conductive dielectric particles has a characteristic time τ_{MW} which depends on both conductivity and dielectric constants of the particles and on the solvent:

$$\tau_{MW} = \epsilon_0 \frac{\epsilon_p^{'} + 2\epsilon_s^{'}}{K_p + 2K_s}. \tag{5.3}$$

In the case of **non-spherical** elongated particles with short and long semiaxes a and b the polarizability can still be expressed through the Clausius-Mossotti equation (see Equation 5.1) modified to

include an orientational dependence:

$$\alpha = 4\pi\epsilon_0\epsilon_s a^2 b \frac{\epsilon_p - \epsilon_s}{3(\epsilon_s + (\epsilon_p - \epsilon_s)L)}, \tag{5.4}$$

where L is the geometrical depolarization factor for spheroidal particles [47]. It follows from Equation 5.4 that the process has a characteristic time depending on the particles orientation with respect to the electric field:

$$\tau_{MW} = \epsilon_0 \frac{(1-L)\epsilon_s^{'} + L\epsilon_p^{'}}{(1-l)K_s + LK_s}. \tag{5.5}$$

5.3 Charged particles

When charged particles are considered, the phenomenon becomes more complicated. In fact, as illustrated in subsection 1.3.1, charged colloidal particles in solution have an electric double layer formed by dispersed ions and counterions. The presence of an external electric field provokes the movement of the double layer ions, thus producing non negligible modifications in the double layer structure. As a consequence, to appropriately describe the behavior of charged particles in electric field, hydrodynamic, electric and diffusive processes have to be considered. Hence the physics of this systems is far more complicated than the situations previously considered.

The theoretical framework used to describe this type of system is the so called Standard Electrokinetic Model (SEM) [11, 10, 28, 48]. The SEM embodies all the relevant diffusive and hydrodynamic phenomena, combining charge conservation, Navier-Stoke and Poisson equations with boundary conditions for the electric field, ionic diffusion and conduction. The great generality of the SEM is also the cause of its extreme complexity. Exact solutions are available only in the case of spherical particles.

However, at high frequency, ions diffusion can be neglected and the hydrodynamic fluxes are local. As a consequence charged particles can be regarded as dielectric particles with a conductive skin. Indeed the double layer acts as a conductive coating and its properties can be embedded into an effective surface conductivity K^{σ}. Hence the behavior of charged colloids at high enough frequency can be described through an extended Maxwell-Wagner model (EMW) i.e. charged particles are analogous to conductive particles. The polarization process can be ascribed to the charge displacement inside the electric double layer necessary to produce matching between the ions current inside the electrolyte solution and the counterions current inside the electric double layer. To calculate the polarizability of a charged spherical particle it's necessary to know both the particle dielectric constant ϵ_p and its conductivity K_p. In particular K_p has to be regarded as a particles property including differ-

ent processes involving the double layer. It has been shown by O'Konski [49] that a non-conductive spherical particle with surface conductivity K_p^s generates the same dipolar field of a particle with volume conductivity K_p with

$$K_p = \frac{2K_p^s}{R}. \tag{5.6}$$

From the former equation it follows that, for highly charged colloids with thin double layer, the particle polarizability can be calculated through an appropriate estimation of the surface conductivity. This approximation is justified only at high frequency where the ion concentration is not influenced by the oscillating electric field [50, 51]. Hence in the limit case of high ionic strength, high particle's charge and high frequency the processes around a spherical particles can be embodied into a surface conductivity $K_p^s(q, \kappa, K_s)$, function of the particle surface charge q, of the Debye length κ^{-1} and of the solvent conductivity K_s:

$$K_p^s = \kappa^{-1}\left[exp\left(\left|\frac{e\zeta}{2k_BT}\right|\right) - 1\right](1 + 3m)\,K_s, \tag{5.7}$$

where e is the elementary charge , ζ is the particle surface potential, and m is a parameter depending on the type of electrolyte.

Since the particle surface charge q and the ζ potential for a $1:1$ electrolyte, when $\zeta >> 2k_BT/e$, are related by the equality

$$q = 2\frac{\epsilon_s\epsilon_0 k_BT}{e}\kappa sinh\left(\frac{e\zeta}{2k_BT}\right), \tag{5.8}$$

Equation 5.7 can be rewritten as:

$$K_p^s(\boldsymbol{r}) \approx q(\boldsymbol{r})\frac{K_s}{zeI}(1 + 3m), \tag{5.9}$$

with I ionic strength of the solution.

In synthesis, the EMW models is based on two simplifying hypothesis i.e. the assumption that at high frequency ion diffusion can be neglected and that hydrodynamic fluxes are local. Under these conditions, the polarizability of a charged spherical particle can be calculated through some steps. First, the surface conductivity of a non-conducting particles K_p^s is computed mapping superficial processes into a surface conductivity (Equation 5.7). Then, following O' Konski treatment, the surface conductivity is converted into an equivalent volume conductivity (Equation 5.6). Finally, by inserting K_p into Clausius-Mossotti formula (Equation 5.1) the particle polarizability is calculated according to the MW model.

Instead at low frequency the model is more complex because of the presence of various entan-

gled processes, including displacement of counterions within the electric double layer, solvent flows (electro-osmosis) which will be described in the next section, ion-screened electrostatics, perturbations of the neutral salt local concentration. This last occurrence, known as concentration polarization, is the basic mechanism at the origin of the so called α-relaxation process. The concentration polarization is due to the presence of two kinds of ionic motion: assuming a negative charged particle having thus a double layer rich in cations, there will be normal fluxes in the solution while at the particle surface there will be a tangential flux of cations along the interface. If the electric field is directed from the left to the right of the particle, on the particle right side there will be a normal outward flux of cations from the double layer and a normal inward flux of anion from the bulk solution. This process generates an increased neutral salt concentration c. On the contrary, on the particle left side, normal fluxes generate a decrease in electrolyte concentration. A gradient of neutral salt is established in a time inversely proportional to the effective ions diffusion coefficient D_{eff}:

$$\tau_\alpha \approx \frac{(R+\kappa^{-1})^2}{2D_{eff}} \tag{5.10}$$

with κ^{-1} double layer thickness and D_{eff} equals to:

$$D_{eff} = \frac{2D^+D^-}{D^+ + D^-}. \tag{5.11}$$

The characteristic frequency of the phenomenon is $\omega_\alpha \approx 1/\tau_\alpha$.

The modification in the salt concentration will provoke a compression of the double layer on the particle right side and an expansion on the left side. Hence, on the right side of the double layer cations accumulate close to the particle surface while on the left side they are driven at a grater distance from particle surface. Consequently the center of charges shifts to the left, generating a dipole moment pointing against the field. The concentration gradient generates diffusion fluxes from right to left, that means opposite to the tangential fluxes provoked by the external field. The concentration polarization mechanism is sketched in Figure 5.1. For sufficiently high frequency the ions accumulation cannot form and the diffusion current will be frozen, as sketched in Figure 5.1(b).

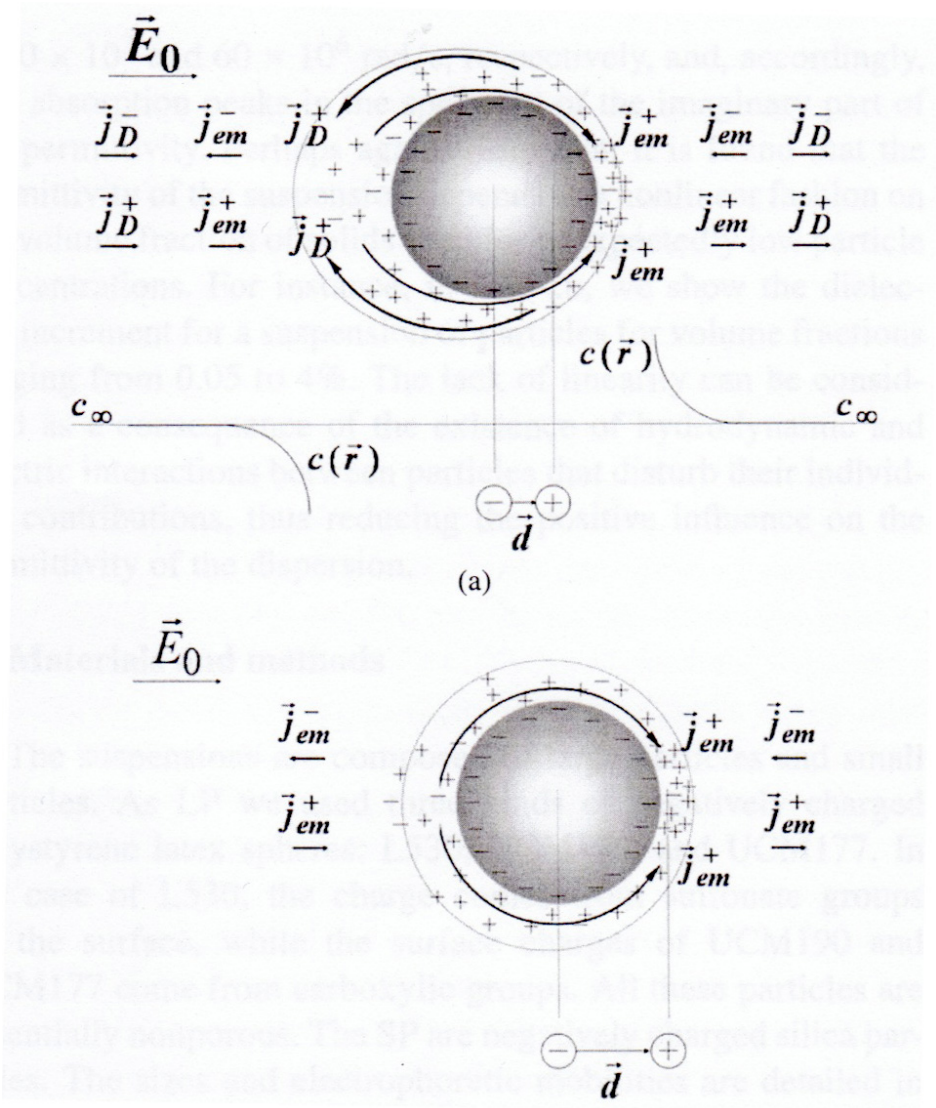

Figure 5.1: Schematic representation of the fluxes of counterions (+) and coins (-) around a negatively charged colloids in presence of an electric filed E_0.In (a) the concentration polarization mechanism causes diffusion fluxes ($j_D^{\pm}$) in addition to the electromigration ones ($j_{em}^{\pm}$) due to the action of the electric field. In (b) the frequency is above the α-relaxation and only electromigration fluxes remain.

5.4 Electro-osmosis

Electro-osmosis is a basic electrokinetic phenomenon. The physical mechanism is as follows. A surface or particle with surface charge q in aqueous solution, as described in subsection 1.3.1, attracts a screening cloud richer of counter-charged ions to form an electrochemical double layer. The application of an external electric field exerts on the electrolyte ions a force proportional to the ion charge q namely $F_e = E \cdot q$. At stationary condition this force is balanced by the viscous friction force $F_v = 6\pi\eta R v$, with R and v radius and velocity of the ions and η viscosity of the fluid. Hence the stationary velocity is:

$$v = \frac{Eq}{6\pi\eta R} \propto E. \tag{5.12}$$

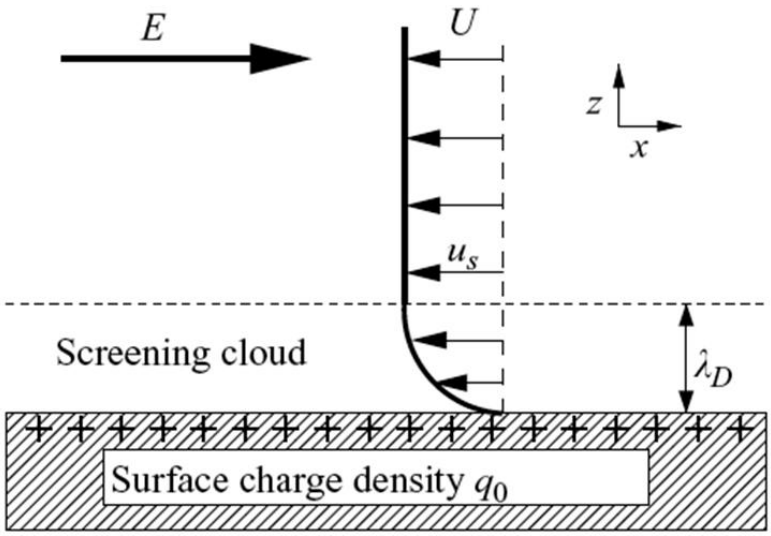

Figure 5.2: Electro-osmotic velocity profile.

In the region of neutral salt every ion is dragged by the same force, which is only proportional to the ion charge. Thus, in neutral salt region, there is no net flux. On the contrary, inside the double layer there is an excess of charges of one sign, so there is a net flux of ions. This flux drags the solvent generating a solvent profile velocity. The solvent velocity is zero at contact with the surface and exponentially reaches the value of Equation 5.12. The penetration length of this process is time dependent, since a certain time is necessary to the solvent flow to reach its stationary value and to extend far from the electric double layer zone in proximity of the charged surface.

5.5 Induced-Charge Electro-osmosis (ICEO)

The electro-osmotic flow described in the previous section involves the interaction of an applied field and a surface with fixed charge; hence the electro-osmotic flow is linear in the applied electric field. The induced-charged electro-osmosis is instead a non-linear phenomenon which originates in proximity of uncharged, polarizable (metal or dielectric) surfaces. In the simplest case, an uncharged conducting cylinder is considered. Immediately after the application of an external electric field $\boldsymbol{E} = E_0\boldsymbol{z}$, the field lines around the particle bend to intersect the conducting surface at a right angle. In response to the applied electric field, mobile ions in the electrolyte solution move: a current $\boldsymbol{J} = \sigma\boldsymbol{E}$ accumulate positive ions on one side of the particle and negative ions on the other side. Thus an induced opposite charge creates on the two side of the conductor. The dipolar charge grows until the establishment of a steady-state, i.e. no field line penetrates the induced double layer. The tangential field drives an electro-osmotic slip velocity (see Equation 5.12) proportional to the local double layer charge density, which drag solvent from the poles to the equator (see Figure 5.3). An ac field drives

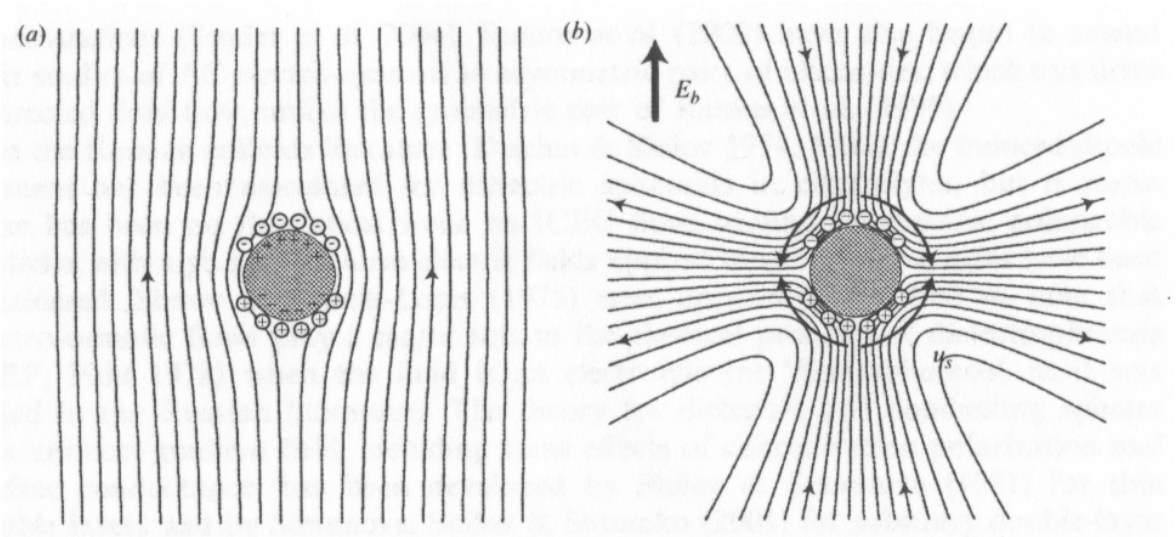

Figure 5.3: ...Electro-osmotic flow around a conducting cylinder with zero net charge.

an identical flow, when the electric field is oppositely directed, since it induces oppositely dipolar charges around the particle, generating the same net flow. All this treatment applies to uncharged, polarizable (metal or dielectric) surfaces.

Little is instead known about non-linear fluid flows in proximity of charged surfaces. In [14, 15] a model is proposed to explicitly calculate nonlinear solvent flows in proximity of charged dielectric particles as function of the zeta potential and of the ionic strength. The flow lines are sketched in Figure 5.4.

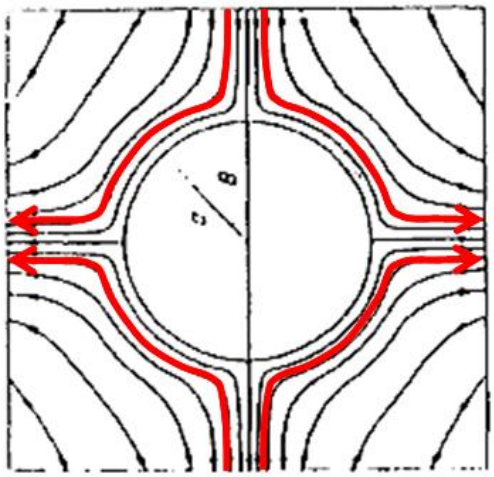

Figure 5.4: Pattern of distribution of nonlinear flows near a polarized particle.

6 Experimental results of electrokinetics interactions

6.1 Electric Birefringence Spectroscopy measurements (EBS)

6.1.1 Monodisperse PTFE suspensions

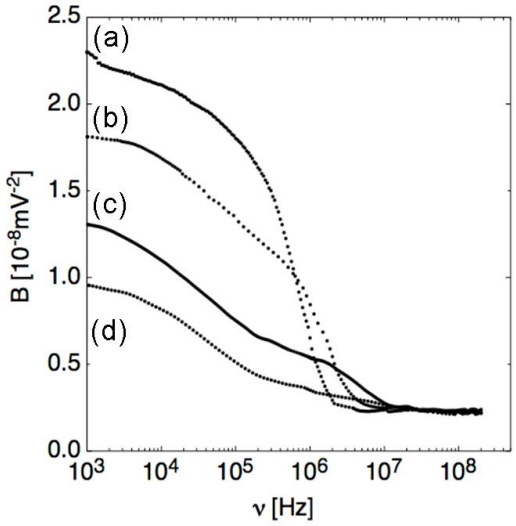

Figure 6.1: Frequency dependence of the Kerr coefficient $B(\nu)$ measured in PTFE solution ($\phi = 0.001$). Curves refer to different ionic strengths I: (a) $I = 0.02\,mM$ KCl; (b) $I = 0.05\,mM$ KCl; (c) $I = 1\,mM$ KCl; (d) $I = 4\,mM$ KCl [52].

Figure 6.1 shows a typical birefringence spectrum obtained by applying an electric field of about $1 - 3\,V/mm$ to an aqueous dispersion of PTFE rods with volume fraction $\phi = 10^{-3}$ at various ionic strengths [52]. At any frequencies the Kerr coefficient $B(\nu)$ decreases upon increasing the ionic strength. Moreover the Kerr coefficient is a decreasing function of the frequency in the kHz and MHz

region, except for a dip in the MHz region. Figure 6.2 shows an aqueous dispersion of PTFE rods with volume fraction $\phi = 10^{-3}$ with particles fully covered with AOT at various ionic strengths [52]. As highlighted in section 2.5, the AOT is an anionic surfactant which can be adsorbed onto particles surface to increase PTFE charge. In this case too $B(\nu)$ decreases by increasing the ionic strength of the solution.

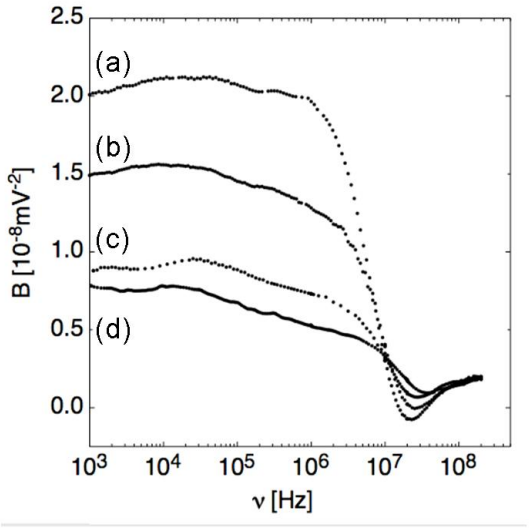

Figure 6.2: Frequency dependence of the Kerr coefficient $B(\nu)$ measured in PTFE solution ($\phi = 0.001$) where $10^{-4}\, mol/l$ AOT have been added. Curves referee to different ionic strengths I: (a) $I = 0.01\, mM$ KCl; (b) $I = 1\, mM$ KCl; (c) $I = 2\, mM$ KCl; (d) $I = 4\, mM$ KCl [52].

As highlighted in section 5.3 and recognizable in both Figure 6.1 and Figure 6.2, the behavior of charged particles in the electric field presents two different regime. At high enough frequency the rods behavior can be explained considering only electrostatics effects and ionic displacements, according to the extended Maxwell-Wagner model. As shown in Figure 6.3, the high frequency behavior of the Kerr coefficient can be fit using the Maxwell-Wagner model to describe the polarizability of a spheroidal particle. In Maxwell-Wagner regime $B(\nu)$ drops quickly toward the asymptotic value between 1 and $10\, MHz$; after a pronounced dip (in the case of highly charged particles), the asymptotic value is reached at frequencies above $100\, MHz$. The values of the Maxwell-Wagner frequency ν_{MW} extracted from the fitting function depend on the ionic strength and the particles charge.

Instead, at low frequency, $B(\nu)$ decreases smoothly and monotonically for low charged particles while, for highly charged particles, $B(\nu)$ is less dependent on ν. In the low frequency regime hydrodynamic effects can not be neglected and the interpretation of the Kerr coefficient behavior is far more complicated.

Figure 6.4 shows the fits obtained through Fixman's algorithm of two experimental curves. Fit

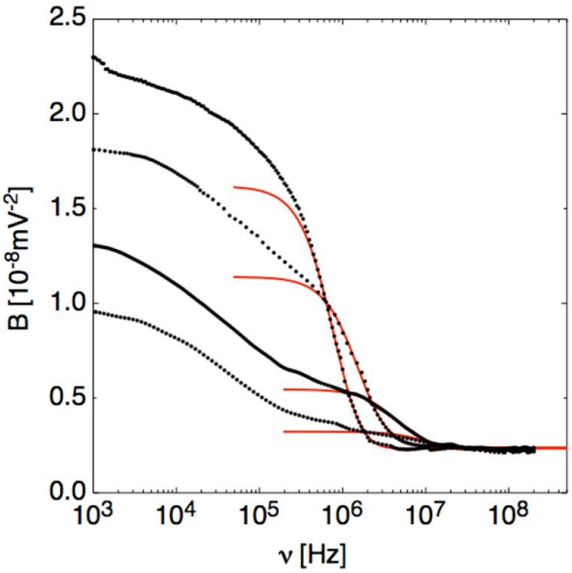

Figure 6.3: Maxwell-Wagner high frequency fit of the Kerr coefficients shown in Figure 6.1.

analysis indicates that the low frequency behavior of $B(\nu)$ vs. ν requires a negative hydrodynamic torque acting on rod-like particles.

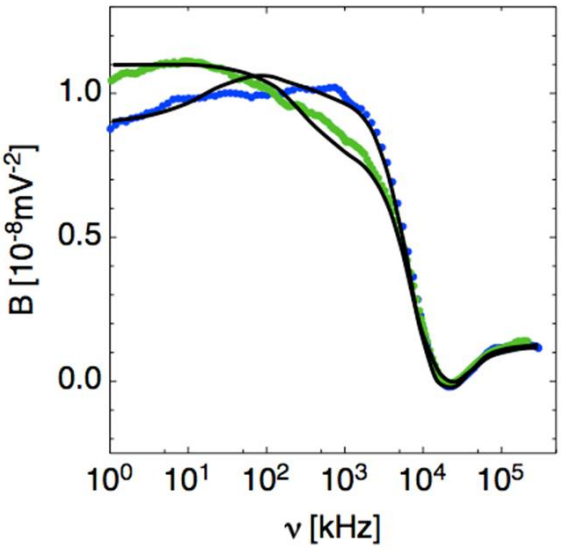

Figure 6.4: Fixman's fit of two experimental curves of $B(\nu)$.

6.1.2 Bidisperse PTFE + SP suspensions

As introduced in subsection 1.4.2 Mantegazza et al. [23] observed a strange low frequency behavior of the Kerr coefficient when charged rod-like "primary particles" (PP) are dispersed in a solution with smaller spherical "secondary particles" (SP) charged of the same sign.

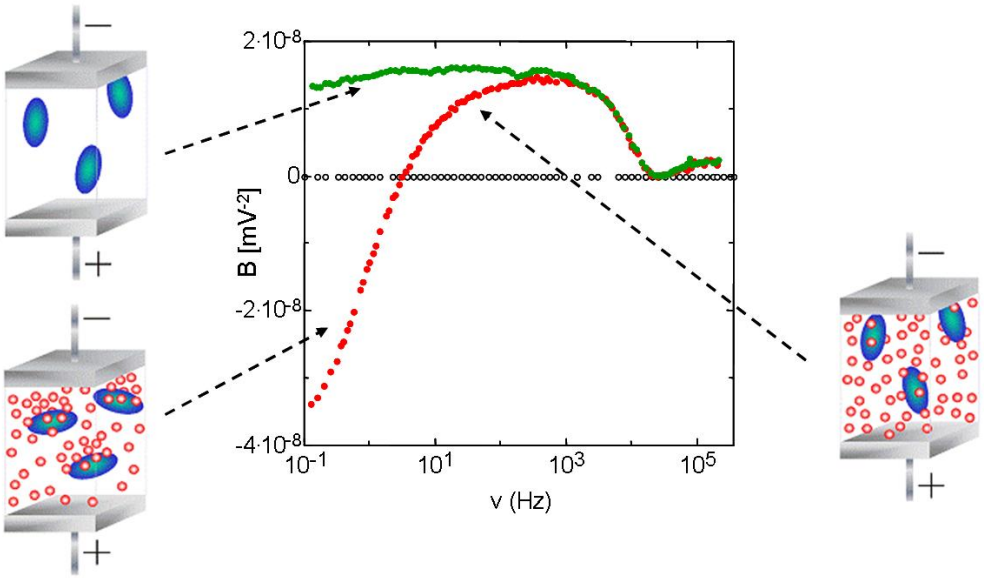

Figure 6.5: Kerr coefficient spectra for: Green dots: monodisperse PTFE ($\phi = 0.001$) (PP); Black empty dots: monodisperse polystyrene spherical particles ($R = 18\,nm$, $\phi = 0.01$) (SP); Red dots: bidisperse mixture of PP and SP ($\phi_{PP} = 0.001$, $\phi_{SP} = 0.01$)[23].

Green dots in Figure 6.5 represent the typical Kerr coefficient spectra for a dilute solution (volume fraction $\phi = 0.001$) of PTFE particle. The spectra is relatively flat up to about $1\,MHz$, indicating that the anisotropy of the electric polarization of the particles is basically constant. Above $1\,MHz$ $B(\nu)$ starts decreasing and reaches an asymptotic value around $100\,MHz$. The $B(\nu)$ trend indicates that the orientational order decreases for frequency higher than $1\,MHz$. For dilute dispersion of PP the Kerr coefficient always assumes positive values (with the possible exception of a small frequency interval in the MHz range [53]) and hence indicates that rods are oriented with their long axis parallel to the field direction. Black empty dots in Figure 6.5 are instead the birefringence signal of a dispersion of SP, in that case polystyrene spheres with radius $20\,nm$ and volume fraction $\phi = 0.01$. As expected spherical particles produce negligible signal with respect to rod like particles. Red dots finally represent $B(\nu)$ of a bidisperse mixture obtained by mixing PP and SP (volume fractions $\phi_{PP} = 0.001$ and $\phi_{SP} = 0.01$): the birefringence spectra shows a large negative value at low frequency, indicating that rods orient preferentially perpendicularly to the electric field direction. The parallel orientation is instead recovered at high frequency.

The exploration of many different bidisperse systems in [23] clearly indicates that the anomalous low frequency birefringence response is a general feature of charged rod-sphere mixtures, as evident from Figure 6.6 (a) and (b), where the same anomalous response has been obtained with different types of PP and SP particles respectively. The anomalous birefringence can not be ascribed

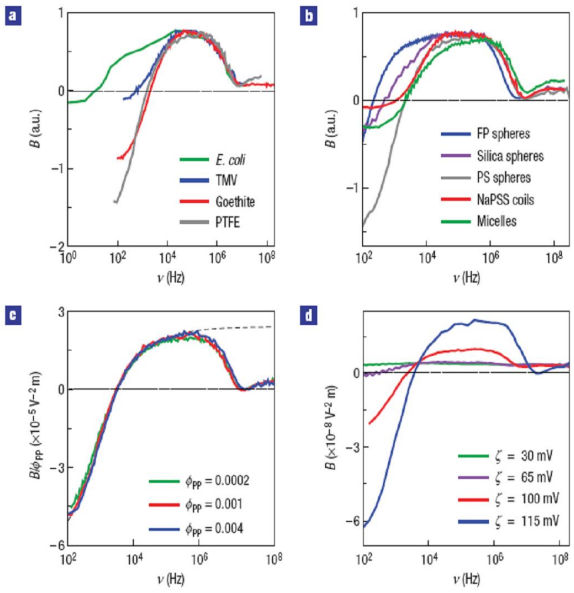

Figure 6.6: Kerr constant spectra for various PP and SP mixtures [23]. (a) $B(\nu)$ of mixtures of polystyrene spherical SP ($\phi_{SP} = 0.01$) with various PP. (b) $B(\nu)$ of mixtures of PTFE PP ($\phi_{PP} = 0.001$) with various negatively charged SP. (c) $B(\nu)/\phi_{PP}$ of mixtures of PTFE and polystyrene spherical SP ($R = 18\,nm$) at fixed $\phi_{SP} = 0.01$ and variable ϕ_{PP} (d) $B(\nu)$ of mixtures of PTFE PP ($\phi_{PP} = 0.001$) and Ludox AS30 SP ($R = 15\,nm$, $\phi_{SP} = 0.01$) at different concentration ϕ_T of a non-ionic surfactant, which controls the PTFE surface charge density and thus the ζ potential [23].

to an SP-mediated anisotropic interactions between rods: indeed, as highlighted in Figure 6.6 (c), there is a perfect collapse of several $B(\nu)/\phi_{PP}$ curves of mixture having the same ϕ_{SP} and various ϕ_{PP}. Thus the anomalous behavior is a property of each single rod surrounded of SP particles. Data in Figure 6.6(d) have been obtained by modifying the PTFE charge through the absorption of a charge non-ionic surfactant. Decreasing the PTFE charge both the high frequency normal response and the low frequency anomalous behavior decrease, demonstrating the electrokinetic nature of $B(\nu)$ on the whole explored frequency range. The effect depends also on SP charge and disappears when uncharged SP are employed. A quantitative analysis of the reported data allows also to exclude an SP-PP induced dipoles interaction as explanation of the anomalous effect.

The low frequency trend of $B(\nu)$ have been fitted through the function for the polarizability of charged spherical particles in electrolyte solution proposed by Fixman [54](see Figure 6.6(c). In Fixman model the frequency dispersion of the polarizability is related to a concentration-polarization mechanism and thus the characteristic frequency is given by the time required to the electrolyte ions to diffuse across the spherical particle and is typically $\propto 10 - 100\,kHz$. In this case instead the values extracted for the characteristic frequency in the anomalous range are about 10-1000 times smaller and of the order of time required to SP to diffuse across PP. Hence Mantegazza et al. indicate as possible

mechanism at the origin of the anomalous behavior an SP crowding on one side of the PTFE which generates a negative hydrodynamic torque on the PP particles.

6.2 Electric Transmitted Light Intensity measurements of rod-like particles

To get better insights into the physics of this anomalous behavior, we decided to study the effect of the electric field on the scattering cross section of PTFE+SP mixtures by performing Electric Transmitted Light Intensity (ETLI) measurements.

6.2.1 Monodisperse PTFE suspensions

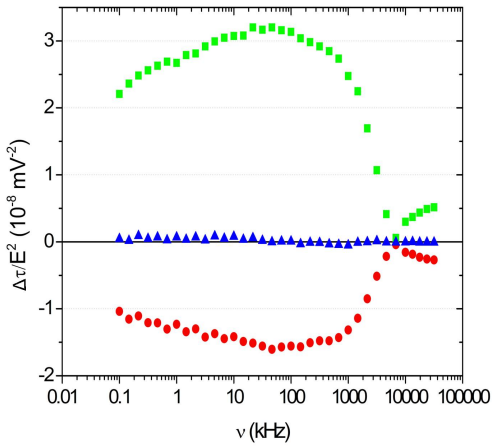

Figure 6.7: ETLI measurement of a dispersion of PTFE rod-like particles. $\phi_{PTFE} = 0.001$, ionic strength $I = 0.5\,mM$ KCl. Green squares: $\Delta\tau_{\|}/E^2$; Red dots: $\Delta\tau_{\perp}/E^2$; Blue triangles: $\Delta\overline{\tau}/E^2$.

Figure 6.7 shows the ETLI measurements performed on a monodisperse solution of PTFE rods ($\phi = 0.001$) in ionic strength $I = 0.5\,mM$ KCl. Since the turbidity variation is proportional to the square field amplitude for all frequencies and both polarizations, ETLI measurements plots present the turbidity variation induced by the application of the electric field divided for the square field amplitude as a function of the electric field frequency ν. Green squares and red dots are $\Delta\tau_{\|}$ and $\Delta\tau_{\perp}$, i.e. the induced turbidity variation detected with a light beam polarized parallel or perpendicular to the electric field direction respectively . Thus $\Delta\tau = \tau_E - \tau_0$ is the difference between turbidity measured in presence of the electric field and the turbidity of the sample in isotropy condition, when no electric field is applied. Blu triangles in Figure 6.7 have been obtained by calculating for each frequency the

difference between the "mean turbidity" defined as $\overline{\tau} = (\tau_{\|} + 2\tau_{\perp})/3$ and the turbidity of the sample in isotropy condition. For each frequency results $\overline{\tau} - \tau_0 \approx 0$.

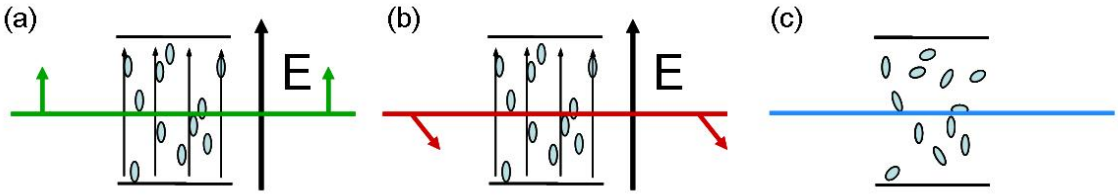

Figure 6.8: (a) $\tau_{\|}$, (b) $\tau_{\perp}$, (c) τ for the sample in an isotropy state.

6.2.2 Bidisperse PTFE + SP suspensions

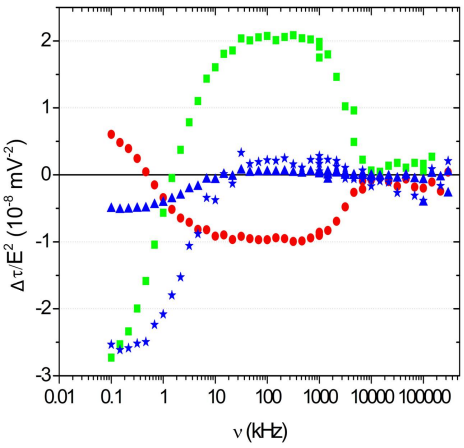

Figure 6.9: ETLI measurements of $\Delta\tau/E^2$ in a PTFE+P20 mixture measured for parallel (green squares) and perpendicular (red dots) polarizations. Blue triangles have been obtained by calculating $\Delta\overline{\tau}/E^2 = (\overline{\tau} - \tau_0)/E^2$. Blue stars are $\Delta\overline{\tau}/E^2$ magnified of five times. $\phi_{PTFE} = 0.001$, $\phi_{P20} = 0.01$, ionic strength $I = 0.5\,mM$ KCl.

Figure 6.9 presents $\Delta\tau/E^2$ data for a suspension of PTFE PP ($\phi_{PTFE} = 0.001$) and polystyrene spherical particles P20 as SP ($R_{P20} = 20\,nm$, $\phi_{P20} = 0.01$) in a ionic strength $I = 0.5\,mM$ KCl. The fact that $\tau_{\perp} > \tau_{\|}$ confirms the low-frequency orientational anomaly. The anomaly noticed in ETLI data and EBS data are in the same frequency range, with a characteristic frequency $\nu_{mix} \cong 5\,kHz$. The low frequency anomalous behavior is proportional to the volume fraction of PTFE particles, as evident from the perfect collapse of curves in Figure 6.10. The dependence on SP volume fraction is instead far more complicated (see Figure 6.11). Moreover $\overline{\tau} < \tau_0$ indicates an overall clearing of the dispersion.

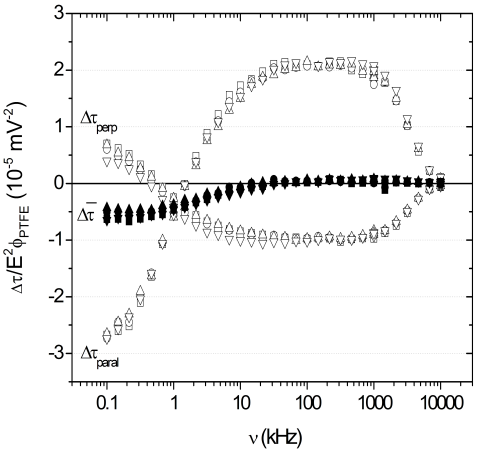

Figure 6.10: $\Delta\tau_{\|}/(E^2\phi_{PTFE})$, $\Delta\tau_{\perp}/(E^2\phi_{PTFE})$ and $\Delta\overline{\tau}/(E^2\phi_{PTFE})$ of PTFE + P20 ($\phi_{P20} = 0.01$) mixtures at various PTFE volume fractions (ionic strength $I = 0.5\,mM$ KCl). Squares: $\phi_{PTFE} = 0.0005$; Circles: $\phi_{PTFE} = 0.001$; Triangles: $\phi_{PTFE} = 0.002$; Capsized triangles: $\phi_{PTFE} = 0.003$.

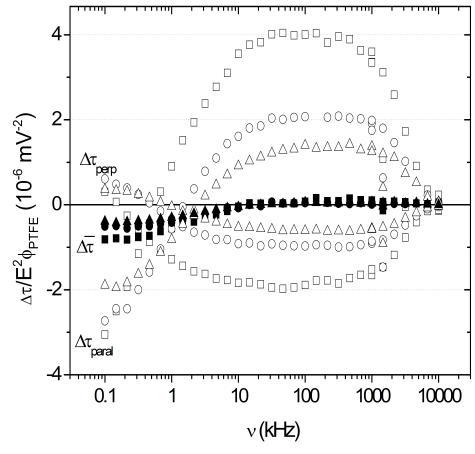

Figure 6.11: $\Delta\tau_{\|}/E^2$, $\Delta\tau_{\perp}/E^2$ and $\Delta\overline{\tau}/E^2$ of PTFE + P20 ($\phi_{PTFE} = 0.005$) mixtures at various P20 volume fractions (ionic strength $I = 0.5\,mM$ KCl). Squares: $\phi_{P20} = 0.002$; Circles: $\phi_{P20} = 0.005$; Triangles: $\phi_{P20} = 0.01$; Capsized triangles: $\phi_{P20} = 0.015$.

In the following section we demonstrate that this difference between $\overline{\tau}$ and τ_0 can not be simply ascribed to an orientational behavior of the PTFE rods.

6.2.3 Summation rules

As seen in subsection 2.4.1, the turbidity, being proportional to the total scattering cross section, depends on the optical polarizability of the dispersed particles and hence on their orientational distribution. From basic optical modeling, it is possible to show that, for any cylindrically symmetric distribution of our PTFE particles in high dilute condition, the average turbidity $\overline{\tau}$ coincides with τ_0, the turbidity of the same sample in the isotropic state. To perform the calculation we have first considered a particle having generic spatial orientation and axially symmetric polarizability and we have expressed the direction of the particle axis through a spherical coordinate system (see Figure 6.12).

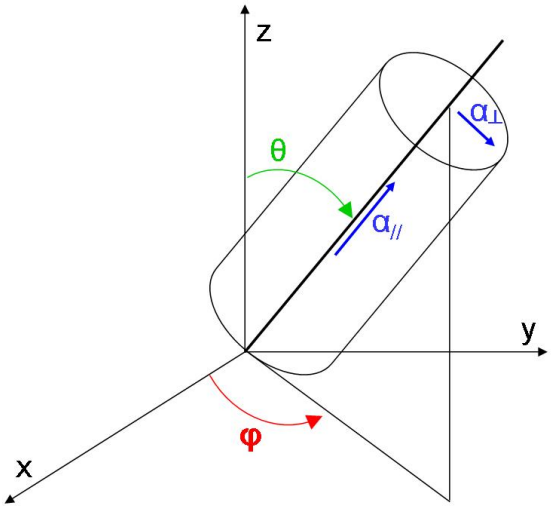

Figure 6.12: Spherical coordinate system for particle orientation.

According to Figure 6.12, the particle axis coordinate in the XYZ reference system are:

$$\begin{cases} x = sen\theta cos\phi \\ y = sen\theta sen\phi \\ z = cos\theta \end{cases} \tag{6.1}$$

In our notation, in the particle coordinate system, the polarizability of the colloid is a diagonal matrix

and the diagonal elements are $\alpha_{\parallel}$ and $\alpha_{\perp}$:

$$\alpha_{diag} = \begin{pmatrix} \alpha_{\perp} & 0 & 0 \\ 0 & \alpha_{\perp} & 0 \\ 0 & 0 & \alpha_{\parallel}. \end{pmatrix} \tag{6.2}$$

The particle polarizability in the XYZ coordinate system is obtained through a rotation of the diagonal matrix α_{diag} of an angle θ around X and of an angle $\pi/2 - \phi$ around Z, namely:

$$\alpha_{xyz} = \boldsymbol{R}_{\theta\phi} \cdot \alpha_{diag} \cdot \boldsymbol{R}_{\theta\phi}^{-1}, \tag{6.3}$$

where $\boldsymbol{R}_{\theta\phi}$ is defined as:

$$\boldsymbol{R}_{\theta\phi} = \begin{pmatrix} cos(\frac{\pi}{2} - \phi) & sen(\frac{\pi}{2} - \phi) & 0 \\ -sen(\frac{\pi}{2} - \phi) & cos(\frac{\pi}{2} - \phi) & 0 \\ 0 & 0 & 1 \end{pmatrix} \cdot \begin{pmatrix} 1 & 0 & 0 \\ 0 & cos\theta & sen\theta \\ 0 & -sen\theta & cos\theta \end{pmatrix} \tag{6.4}$$

If the particle considered are small enough, we can neglect the form factor in the expression of the scattered intensity. The scattered intensity is thus proportional to the square dipole moment modulated by the polarization toroid of the dipolar emission, namely:

$$I_S \propto |\boldsymbol{p}|^2 \, sen^2\Psi, \tag{6.5}$$

where $\boldsymbol{p}$ is the induced dipole moment while Ψ is the angle between the dipole moment and the scattering direction. The optical dipole moment induced in the particle by a light beam can be calculated by projecting the polarizability of the particle along the light polarization direction i.e. by calculating the scalar product between the polarizability matrix and the versor in the polarization direction. We calculated that product for light polarized along the three coordinate system axis directions:

$$\begin{cases} \boldsymbol{p}_x = E_0 \alpha_{xyz} \cdot \boldsymbol{u}_x = E_0 \alpha_{xyz} \cdot (1,0,0) \\ \boldsymbol{p}_y = E_0 \alpha_{xyz} \cdot \boldsymbol{u}_y = E_0 \alpha_{xyz} \cdot (0,1,0) \\ \boldsymbol{p}_z = E_0 \alpha_{xyz} \cdot \boldsymbol{u}_z = E_0 \alpha_{xyz} \cdot (0,0,1), \end{cases} \tag{6.6}$$

where $\boldsymbol{u}_x$,$\boldsymbol{u}_y$ and $\boldsymbol{u}_z$ are the unit vectors oriented as the system coordinate axises.

Indicating with $\boldsymbol{u}_s$ a generic unit vector in the scattering direction, $sen^2\Psi$ can be calculated as:

$$sen^2\Psi = 1 - (\boldsymbol{u}_p \cdot \boldsymbol{u}_s) = 1 - cos^2\Psi, \tag{6.7}$$

with $\boldsymbol{u}_p$ unit vector along dipole moment direction. Reminding that the power emitted from a dipole is the integral of the scattered intensity on the whole solid angle, we calculated, for each light beam polarization, the power radiated by the particle. As seen in subsection 2.4.1, the turbidity is directly related to the emitted power, so that we have calculated the mean turbidity $\overline{\tau} = (\tau_x+\tau_y+\tau_z)/3$, where τ_x,τ_y and τ_z are the turbidity measured with light polarized along X,Y and Z respectively. Through this calculation we verified that for a particle with any given spatial orientation, the average scattering cross section does not depend on the particle orientation and is alway proportional to $\alpha_{\parallel}^2 + 2\alpha_{\perp}^2$ i.e. $\overline{\tau} = (\tau_{\parallel} + 2\tau_{\perp})/3$. Thus, if we consider a dilute solution of small particles, so that both the form factor and the structure factor can be neglected, the optical properties of the solution depend only on the optical behavior of the dispersed particles. Hench $\overline{\tau} \propto \alpha_{\parallel}^2 + 2\alpha_{\perp}^2$.

In particular we considered a cylindrically symmetric distribution of rod-like particles and we modeled the orientational distribution of the particles with a 3D gaussian function with symmetry axis along the coordinate system directions. This model indeed should represent our experimental condition where the application of an external electric field to a colloidal dispersion of anisotropic particles biases the anisotropic orientational distribution of the particles generating a system with cylindric symmetry. By performing the calculation according to the model previously described we verified that $\overline{\tau} = (\tau_{\parallel} + 2\tau_{\perp})/3 = \tau_0$ where τ_0 is the mean turbidity of the sample in the isotropic state; τ_0 has been calculated through the integration of the power radiated by the particle on whole particle axis directions.

As introduced in section 2.1 the light intensity scattered from a particle depends on the the square of the particle form factor $F(\boldsymbol{q})$ defined as:

$$|F(\boldsymbol{q})|^2 = \frac{1}{V^2}\left|\int_V e^{i\boldsymbol{q}\cdot\boldsymbol{r}}\right|^2, \tag{6.8}$$

where V is the particle volume and $\boldsymbol{q}$ is the scattering vector. If the colloidal particles are small compared to the light wavelength $F(\boldsymbol{q}) = 1$ for each $\boldsymbol{q}$ and the interference between light scattered from different infinitesimal volume of the particle can be neglected. We investigated if, with our PTFE rod-like particles, the particles form factor invalidates the previously found results. According to [33] the form factor of rod-like particles with axis parallel to Z direction can be written as the composition of the form factor of a disk of radius R in the XY plane and of a stepwise function of length l along

the Z direction. Hence $F(\boldsymbol{q})$ can be calculated as:

$$F(q_{xy}, q_z) = \frac{sen(lq_z)}{lq_z} \frac{2J_1(Rq_{xy})}{Rq_{xy}}, \tag{6.9}$$

where q_z and q_{xy} are the scattering vector components in the z direction and in the XY plane respectively, with scattering vector defined as $\boldsymbol{q} = \boldsymbol{k}_i - \boldsymbol{k}_s$; $\boldsymbol{k}_i$ and $\boldsymbol{k}_s$ are the vectors in incident and scattering direction respectively. J_1 is the Bessel function of order 1. Similarly to the former procedures, assuming an external electric field parallel to the Z axis (i.e. rod particle aligned parallel to the external electric field), we calculated the variation of the mean turbidity $\overline{\tau}$ of the aligned sample with respect to the turbidity of the same sample in an anisotropic state. We have seen that the form factor does not invalidate the summation rule, so that the equality $\overline{\tau} \cong \tau_0$ remains valid. Hence we verified that the anomaly in the birefringence spectra can not be ascribed to an orientational behavior of the rod-like particles.

6.2.4 Analysis of the results

Low frequency ETLI measurements on rod-sphere mixtures present $\tau_\perp > \tau_\parallel$: this fact confirms the orientational anomaly found in birefringence measurements, with particles preferentially oriented perpendicularly to the electric field. However, this orientational behavior of the rods, does not account for the overall field-induced clearing of the mixtures, which present $\overline{\tau} < \tau_0$. The difference between $\overline{\tau}$ and τ_0 is proportional to the PTFE volume fraction while exhibit a more complicated monotonically increasing dependence on SP volume fraction. All this findings indicate that a field-induced redistribution of the spherical particles around each PTFE rod takes place in the same frequency range where the orientational anomaly is found, suggesting the two phenomena to be related. The two effects have the same characteristic frequency $\nu_{mix} \cong 5$ kHz, which is about 30 times lower than the expected α-relaxation frequency ν_α. The α-relaxation is the slowest electrokinetic effect and its basic mechanism is the concentration polarization, an asymmetric accumulation and depletion of neutral electrolyte which modifies the particle double layer (see section 5.3). Thus ν_α depends on the particles mean dimension R and on the mean ionic diffusion coefficient D:

$$\nu_{alpha} \propto \frac{D}{R^2}.$$

ν_{mix} results instead of the order of D_{SP}/R^2, where D_{SP} is the diffusion time of the secondary particles around rods having mean size equal to R. Thus the orientational anomaly and the field-induced clearing could be both due to a process analogous to the concentration polarization, where

the secondary particles act similarly to coions. We decided to verify this hypothesis by studying mixtures having spherical primary particles.

6.3 Electric Transmitted Light Intensity measurements of binary mixtures of spheres

Due to the difficulties in modeling mixtures involving rod-like particles, we decided to devote our attention (both experimentally and theoretically) to binary mixtures of spheres. We thus studied dispersions of large and small spheres with the hope that they could be a model system to reveal a general behavior of colloidal mixture.

Figure 6.13 shows the ETLI measurements in mixtures of polystyrene spherical primary particles P200 ($R = 200\,nm$) with P20 or P30 secondary particles ($R = 20$ or $R = 30\,nm$ respectively).The electric-field induces a turbidity variation in the samples, proportional to the square of the field amplitude E^2 (see Figure 6.13(c)): for this reason in the plots we present the clearing coefficient $\Delta\tau/E^2$. Figure 6.13(a) shows the clearing coefficient for a mixture of P200+P20 and for a mixture of P200+P30 ($\phi_{P200} = 0.002$, $\phi_{P20,P30} = 0.01$). There is a field-induced clearing for both light polarizations at frequencies $\nu < \nu_{mix} \cong 3 - 5$ kHz, which depends on the secondary particles cross-section. The clearing is anisotropic with $\tau_\perp < \tau_\parallel$. Figure 6.13(b) presents the clearing coefficient divided by the P200 volume fraction for mixture of P200 and P20, with various ϕ_{P200}. As evident from the collapse of all the curves, the turbidity variation is proportional to the P200 volume fraction. The dependence on the secondary particles volume fraction is instead far more complex, as evident from Figure 6.14. The effect is slightly dependent on the ionic strength: in Figure 6.15 $\Delta\tau_\perp/E^2$ is shown for a mixture of P200+P20 at various ionic strengths of KCl.

Since in sphere-sphere systems no orientational effect is possible, the field-induced clearing is an unambiguous mark of an interaction phenomenon between large and small spheres. In subsection 6.3.1 we present a calculation performed within second virial expansion formalism which shows that the intensity diffused by the mixture decreases in presence of a repulsive interaction between large and small spheres.

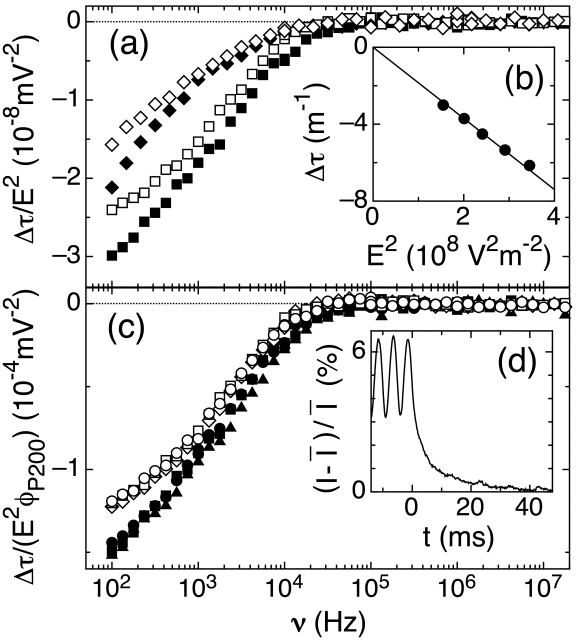

Figure 6.13: Field-induced clearing coefficient (a) $\Delta\tau/E^2$ and (b) $\Delta\tau/(E^2\phi_{P200})$ vs. electric field frequency in mixtures of large and small spheres. Full (empty) symbols indicate perpendicular (parallel) polarization. In (a) P200+P20 (diamonds), P200+P30 (squares). $\phi_{P200} = 0.0002$. In (b) P200+P30 mixtures with various ϕ_{P200}. Dots: $\phi_{P200} = 0.0003$; Squares: $\phi_{P200} = 0.0002$; Triangles: $\phi_{P200} = 0.0001$. In (c) turbidity variation $\Delta\tau$ vs E^2 for a P200+P30 mixture. In (d) relative variation in the transmitted intensity I for a mixture of P200+P30. $\overline{I}$ indicate the transmitted intensity when no field is applied. $E = 24\,Vmm^{-1}$ for $t < 0$ while $E = 0$ for $t > 0$. In (c) and (d) $\nu = 100$ Hz and $\phi_{P200} = 0.0002$. In all panels $\phi_{SP} = 0.01$ [55].

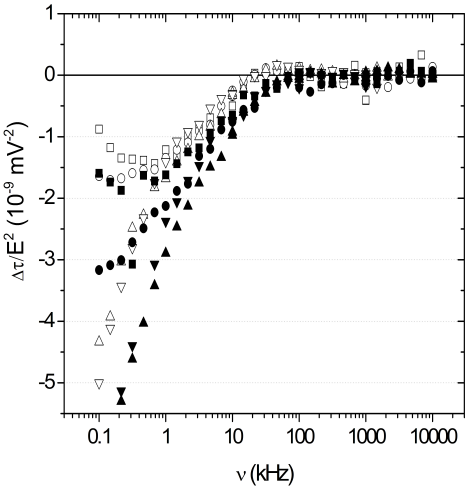

Figure 6.14: Field-induced clearing coefficient $\Delta\tau_\perp/E^2$ (full symbol) and $\Delta\tau_\parallel/E^2$ (empty symbol) for P200+P20 mixtures ($\phi_{P200} = 0.0005$, ionic strength $I = 0.5\,mM$) at various ϕ_{P20}. Squares: $\phi_{P20} = 0.002$; Dots: $\phi_{P20} = 0.005$; Triangles: $\phi_{P20} = 0.01$; Capsized triangles: $\phi_{P20} = 0.015$.

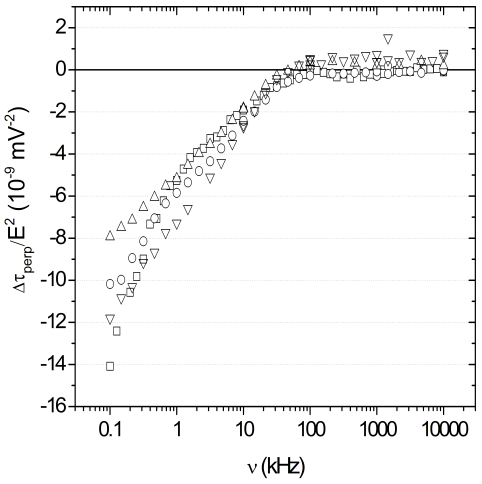

Figure 6.15: Field-induced clearing coefficient $\Delta\tau_\perp/E^2$ for P200+P20 mixtures ($\phi_{P200} = 0.001$, $\phi_{P20} = 0.01$) at various ionic strengths of KCl. Squares: $I = 0.2\,mM$; Dots: $I = 0.5\,mM$; Triangles: $I = 1\,mM$; Capsized triangles: $I = 1.5\,mM$.

6.3.1 Light scattering in binary mixtures of large and small spheres

We want to model the light scattering signal of a mixture of large and small spheres to study what happens to the turbidity of the system in presence of an interaction between the colloids. In general, for a colloidal dispersion, the total scattered intensity in the forward direction is related to the average square fluctuations of the dielectric constant:

$$I(\boldsymbol{k}) \propto \left\langle |\delta\hat{\epsilon}(\boldsymbol{k})|^2 \right\rangle,$$

where $\delta\hat{\epsilon}(\boldsymbol{k})$ is the fourier transform of the dielectric constant fluctuation in real space $\delta\epsilon(\boldsymbol{r})$, i.e. $\delta\hat{\epsilon}(\boldsymbol{k}) = \int d\boldsymbol{r} e^{i\boldsymbol{k}\cdot\boldsymbol{r}}\delta\epsilon(\boldsymbol{r})$.

For a one-component colloidal dispersion with number density $\rho = N/V$, indicating with ϵ_s and ϵ_p the solvent and particle dielectric constant respectively and with V_p the particle volume, the total dielectric constant is:

$$\epsilon(\mathbf{r}) = \epsilon_s + \rho(\mathbf{r})(\epsilon_p - \epsilon_s)V_p \tag{6.10}$$

where the product between ρ and V_p is the particles volume fraction. The dielectric constant fluctuations in $\boldsymbol{k}$ space can be written in terms of the particles concentration fluctuations $\langle|\delta\hat{\rho}(\boldsymbol{k})|^2\rangle$:

$$\langle|\delta\hat{\epsilon}(\boldsymbol{k})|^2\rangle = \Delta\epsilon^2 V_p^2 \langle|\delta\hat{\rho}(\boldsymbol{k})|^2\rangle \tag{6.11}$$

where $\Delta\epsilon$ is the difference between the dielectric constant of particle and solvent.
For a two-component mixture of species 1 and 2, the Equation 6.10 can be rewritten as:

$$\epsilon(\mathbf{r}) = \epsilon_s + \rho_1(\mathbf{r})\Delta\epsilon_1 V_{p1} + \rho_2(\mathbf{r})\Delta\epsilon_2 V_{p2}$$

so that the mixture dielectric constant fluctuations assume the form:

$$\langle|\delta\hat{\epsilon}(\boldsymbol{k})|^2\rangle = \Delta\epsilon_1^2 V_{p1}^2\langle|\delta\hat{\rho}_1(\boldsymbol{k})|^2\rangle + \Delta\epsilon_2^2 V_{p2}^2\langle|\delta\hat{\rho}_2(\boldsymbol{k})|^2\rangle + 2\Delta\epsilon_1\Delta\epsilon_2 V_{p1}V_{p1}\langle\delta\hat{\rho}_1(\boldsymbol{k})\delta\hat{\rho}_2(\boldsymbol{k})\rangle \quad (6.12)$$

The presence of any sort of interaction between the colloids affects the concentration fluctuations and, as a consequence, the optical response of the system.

It is known from literature [56] that the light intensity scattered by a one component colloidal dispersion is proportional to the osmotic isothermal compressibility χ_T , defined as:

$$\chi_T = -\frac{1}{V}\left(\frac{\partial V}{\partial P}\right)_T = \frac{1}{\rho}\left(\frac{\partial \rho}{\partial P}\right)_T$$

where P is the osmotic pressure of the system. A relative osmotic compressibility can be defined as:

$$\chi_R = \rho k_B T \chi_T = \left[\frac{\partial(\beta P)}{\partial \rho}\right]^{-1}, \quad (6.13)$$

with $\beta = 1/k_B T$. Reminding the thermodynamic definition of pressure:

$$P = -\left[\frac{\partial A}{\partial V}\right] \quad (6.14)$$

where A is the Helmholtz free energy, Equation 6.13 and Equation 6.14 can be combined to obtain:

$$\frac{1}{\rho\chi_R} = \frac{\partial^2}{\partial\rho^2}\left(\frac{A}{VK_BT}\right) = \frac{1}{\rho S(\boldsymbol{k}=0)} \quad (6.15)$$

where, according to [56], the static structure factor for $\boldsymbol{k} = 0$ is defined as $S(0) = \frac{1}{V}\frac{\langle\delta\hat{\rho}^2\rangle}{\rho}$, where the density fluctuations are for $\boldsymbol{k} = 0$. In the following we always consider the scattering in the forward direction and thus we omit to explicitly indicate the $\boldsymbol{k}$ dependence.

For a binary mixture of species 1 and 2 the static structure factor depends also on the cross density

correlation between the two species:

$$\begin{aligned} S_{11} &= \tfrac{1}{V}\tfrac{\langle \delta\hat{\rho}_{11}^2 \rangle}{\rho_{11}} \\ S_{22} &= \tfrac{1}{V}\tfrac{\langle \delta\hat{\rho}_{22}^2 \rangle}{\rho_{22}} \\ S_{12} = S_{21} &= \tfrac{1}{V}\tfrac{\langle \delta\hat{\rho}_1 \delta\hat{\rho}_2 \rangle}{\sqrt{\rho_1\rho_2}} \end{aligned} \tag{6.16}$$

where the Fourier transforms of the density fluctuations are taken for $\boldsymbol{k} = 0$. Hence the mean square density fluctuations are related to the Helmholtz free energy second derivatives through the following equality:

$$\begin{pmatrix} \rho_1 S_{11} & \sqrt{\rho_1\rho_2} S_{12} \\ \sqrt{\rho_1\rho_2} S_{12} & \rho_2 S_{22} \end{pmatrix} = \frac{1}{V} \begin{pmatrix} \langle \delta\hat{\rho}_1^2 \rangle & \langle \delta\hat{\rho}_1 \delta\hat{\rho}_2 \rangle \\ \langle \delta\hat{\rho}_1 \delta\hat{\rho}_2 \rangle & \langle \delta\hat{\rho}_2^2 \rangle \end{pmatrix} = \begin{pmatrix} \frac{\partial^2}{\partial\rho_1^2}\left(\frac{\beta A}{V}\right) & \frac{\partial^2}{\partial\rho_1\partial\rho_2}\left(\frac{\beta A}{V}\right) \\ \frac{\partial^2}{\partial\rho_1\partial\rho_2}\left(\frac{\beta A}{V}\right) & \frac{\partial^2}{\partial\rho_2^2}\left(\frac{\beta A}{V}\right) \end{pmatrix}^{-1} \tag{6.17}$$

To find the influence of colloidal interaction on the scattered intensity it is convenient to express the Helmholtz free energy A with a second virial expansion. It can be shown that:

$$\frac{\beta A}{V} = \rho_1 \ln \rho_1 - \rho_1 + \rho_2 \ln \rho_2 - \rho_2 + B_{11}\rho_1^2 + 2B_{12}\rho_1\rho_2 + B_{22}\rho_1^2 \ldots$$

in which the second virial coefficient B_2^{ij} contains the interaction potential $V^{ij}(\mathbf{r})$ between the species i and j:

$$B_2^{ij} = -\frac{1}{2}\int d\mathbf{r}\left(e^{-\beta V^{ij}(\mathbf{r})} - 1\right). \tag{6.18}$$

The second derivatives in Equation 6.17 assumes the form:

$$\begin{aligned} \tfrac{\partial^2}{\partial\rho_1^2}\left(\tfrac{\beta A}{V}\right) &= \tfrac{1}{\rho_1} + 2B_{11} \\ \tfrac{\partial^2}{\partial\rho_2^2}\left(\tfrac{\beta A}{V}\right) &= \tfrac{1}{\rho_2} + 2B_{22} \\ \tfrac{\partial^2}{\partial\rho_1\partial\rho_2}\left(\tfrac{\beta A}{V}\right) &= 2B_{12} \end{aligned}$$

Hence the concentration fluctuations in Equation 6.17 can be rewritten in terms of the second virial coefficients:

$$\frac{1}{V}\begin{pmatrix} \langle \delta\hat{\rho}_1^2 \rangle & \langle \delta\hat{\rho}_1 \delta\hat{\rho}_2 \rangle \\ \langle \delta\hat{\rho}_1 \delta\hat{\rho}_2 \rangle & \langle \delta\hat{\rho}_2^2 \rangle \end{pmatrix} = \begin{pmatrix} \frac{1}{\rho_1} + 2B_{11} & 2B_{12} \\ 2B_{12} & \frac{1}{\rho_2} + 2B_{22} \end{pmatrix}^{-1} \tag{6.19}$$

and by solving the matrix equality:

$$\begin{aligned}
\langle \delta\hat{\rho}_1^2 \rangle &= \frac{\rho_1+2B_{22}\rho_1\rho_2}{1+2B_{11}\rho_1+2B_{22}\rho_2-4B_{12}^2\rho_1\rho_2+4B_{11}B_{22}\rho_1\rho_2} \\
\langle \delta\hat{\rho}_2^2 \rangle &= \frac{\rho_2+2B_{11}\rho_1\rho_2}{1+2B_{11}\rho_1+2B_{22}\rho_2-4B_{12}^2\rho_1\rho_2+4B_{11}B_{22}\rho_1\rho_2} \\
\langle \delta\hat{\rho}_1\delta\hat{\rho}_2 \rangle &= -\frac{2B_{12}\rho_1\rho_2}{1+2B_{11}\rho_1+2B_{22}\rho_2-4B_{12}^2\rho_1\rho_2+4B_{11}B_{22}\rho_1\rho_2}
\end{aligned} \tag{6.20}$$

To calculate the effects of interactions on the scattered intensity we at first determined the relative variation in the diffused intensity in presence of hard sphere interaction between the particles (I_{HS}) with respect to the intensity diffused by same system in absence of any colloidal interactions (I_0). Namely we substituted in Equation 6.12 the expression of the concentration fluctuations as a functions of the second virial coefficients for hard sphere potential and we evaluated the quantity:

$$\begin{aligned}
&\Delta_{HS} = \tfrac{I_{HS}-I_0}{I_0} = \\
&\Delta\epsilon_1^2 V_{p1}^2 \tfrac{\rho_1+2B_{22}^{HS}\rho_1\rho_2}{1+2B_{11}^{HS}\rho_1+2B_{22}^{HS}\rho_2-4(B_{12}^{HS})^2\rho_1\rho_2+4B_{11}^{HS}B_{22}^{HS}\rho_1\rho_2} + \\
&+\Delta\epsilon_2^2 V_{p2}^2 \tfrac{\rho_2+2B_{11}^{HS}\rho_1\rho_2}{1+2B_{11}^{HS}\rho_1+2B_{22}^{HS}\rho_2-4(B_{12}^{HS})^2\rho_1\rho_2+4B_{11}^{HS}B_{22}^{HS}\rho_1\rho_2} + \\
&-2\Delta\epsilon_1\Delta\epsilon_2 V_{p1}V_{p1} \tfrac{2B_{12}^{HS}\rho_1\rho_2}{1+2B_{11}^{HS}\rho_1+2B_{22}^{HS}\rho_2-4(B_{12}^{HS})^2\rho_1\rho_2+4B_{11}^{HS}B_{22}^{HS}\rho_1\rho_2}
\end{aligned} \tag{6.21}$$

We then evaluated the relative variation Δ_{int} in the diffused intensity in presence of other particles interactions in addition to the hard sphere ones (I_{int}) with respect to the intensity diffused by the same system in absence of any colloidal interactions (I_0):

$$\Delta_{int} = \frac{I_{int} - I_0}{I_0}. \tag{6.22}$$

In particular Δ_{int} have been calculated with an equality similar to Equation 6.21 where, instead of the hard sphere virial coefficient B_2^{HS} we considered various type of interactions between the particles. The quantity:

$$\frac{\Delta_{Int} - \Delta_{HS}}{1 + \Delta_{HS}} \tag{6.23}$$

is the one directly related to our measurements results, according to Equation 2.37. We thus considered different interaction potentials between the particles and we found that a repulsive interaction

between large and small spheres can decrease the scattering of the system. The related turbidity variation is comparable to that observed in our ETLI experiments.

6.3.2 Analysis of the results

All the data point toward a scenario where the presence of the electric field activates a repulsive interaction between large and small spheres which creates an anisotropic depletion layer of SP around the PP. We have analyzed data reported in Figure 6.13 to model the shape of the field-induced SP density distribution and to quantify $\phi_{SP}(\boldsymbol{r})$, the local value of ϕ_{SP} at a distance $\boldsymbol{r}$ from the center of each P200 particle. In particular $\phi_{SP}(\boldsymbol{r}, E) = \phi_{SP}(\boldsymbol{r}, E = 0) + \delta\phi_1(\boldsymbol{r}) + \delta\phi_2(\boldsymbol{r})$, where $\phi_{SP}(\boldsymbol{r}, E = 0)$ is the secondary particles density in zero field condition while $\delta\phi_1(\boldsymbol{r})$ and $\delta\phi_2(\boldsymbol{r})$ are the $O(E)$ and $O(E^2)$ field-induced local density variation respectively. So defined $\delta\phi_1(\boldsymbol{r})$ is odd along the field direction, $\delta\phi_2(\boldsymbol{r})$ is even along E while both density variations have cylindrical symmetry around E. Due to the experimental techniques employed in our measurements, we are not able to detect $\delta\phi_1(\boldsymbol{r})$, as shown from the following argument. Indeed, we can associate to $\phi_{SP}(\boldsymbol{r}, E)$ a refractive index distribution $n(\boldsymbol{r}, E) = n_0(\boldsymbol{r}) + n_1(\boldsymbol{r}) + n_2(\boldsymbol{r})$ where n_0 is the refractive index for $E = 0$ while n_1 and n_2 are the $O(E)$ and $O(E^2)$ field-induced perturbation the the refractive index of the system. If $E \parallel z$, n_1 and n_2 are odd and even along z direction respectively. In our experimental system, n_1 and n_2 can be considered small with respect to n_0 since the scattering power of the SP is much inferior to the scattering power of the PP. The amplitude of the scattered optical field at a certain scattering vector $\boldsymbol{q}$, can be considered as the sum of different contributions:

$$\begin{aligned} E_0^o(\boldsymbol{q}) &= F\left[n_0(r,\theta,z)\right] \quad \in \Re \\ E_1^o(\boldsymbol{q}) &= F\left[n_1(r,\theta,z)\right] \quad \in \Im \\ E_2^o(\boldsymbol{q}) &= F\left[n_2(r,\theta,z)\right] \quad \in \Re \end{aligned}$$

where θ is the angle between incident and scattering direction while F stands for Fourier transform operation of the quantity between parenthesis. The belonging to real and imaginary set follows from the property of Fourier transform of odd and even functions. Thus the scattered intensity results:

$$I(\boldsymbol{q}) = |E_0^o + E_1^o + E_2^o|^2 \cong E_0^o(\boldsymbol{q})^2 + 2E_0^o(\boldsymbol{q})E_2^o(\boldsymbol{q}) + E_1^o(\boldsymbol{q})^2. \tag{6.24}$$

Since $E^o \propto \alpha$ we can give an approximate evaluation of the former three contributions to the diffused intensity. In our experimental system $E_0^o(\boldsymbol{q})^2$ is due to the scattering of the P200 and is proportional to α_{P200}^2. E_1^o and E_2^o instead involve the contribution to the scattering of the regions of depletion of

the SP and thus depend on the polarizability of such depleted regions α_D. According to Clausius-Mossotti equation (see Equation 5.1) with the substitution of dielectric constants with the square refractive indexes, we can calculate α^2_{P200} and α_D as:

$$\begin{aligned} \alpha_{P200} &= \frac{n^2_{P200}-n^2_{mean}}{n^2_{P200}+2n^2_{mean}} \\ \alpha_D &= \frac{n^2_D-n^2_{mean}}{n^2_S+2n^2_{mean}} \end{aligned} \tag{6.25}$$

where $n_{P200} = 1.59$, $n_{mean} = \left(n^2_{H_2O} + (n^2_{SP} - n^2_{H_2O})\phi_{SP}\right)^{\frac{1}{2}}$ is the mean refractive index of the dispersion given by the contribution of the solvent and of the secondary particles. For simplicity we assumed $n_D = n_{H_2O}$ which implies a complete depletion of SP in proximity of each P200. With this assumption it results that α_D is two order of magnitude lower than α_{P200}. Accordingly $E^o_0(\boldsymbol{q})E^o_2$ being proportional to the product $\alpha_{P200}\alpha_D$ is two order of magnitude lower than $(E^o_0)^2$ while $(E^o_1)^2$ is four order of magnitude lower. Thus the last term of Equation 6.24 gives a null or negligible contribution to the scattered intensity while the mixing term is the dominant one. Hence scattering experiments enable only to quantitatively evaluate $\delta\phi_2$.

To verify the former prediction we calculated the scattering of a "traffic light", i.e. a spherical particle surrounded by two spherical zones with radius equal to the particle's radius, one having higher refractive index and the other having lower refractive index than the surrounding medium (see Figure 6.16). The two spherical volumes correspond to region of accumulation and depletion of the secondary particles i.e. to a $\delta\phi_1 \neq 0$.

It's worthwhile noticing that for a "traffic light" smaller than light wavelength, one should expect a diffuse light equals to that scattered by the particles alone. Indeed the object can be regarded as a punctiform oscillating dipole, where the dipoles of the accumulation and depletion regions are equal in modulus but have opposite directions, giving null contribution to the total scattering. Thus a small "traffic light" is indistinguishable from the particle alone. Instead, when the "traffic light" have dimensions comparable to light wavelength, the contributions to the scattered field coming from different parts of the object are not in phase. To calculate the total scattered light we followed the procedure described in subsection 6.2.3 with the addition of a form factor accounting for the assumed $\delta\phi_1$. In particular the optical field scattered from the "traffic light" have been calculated as:

$$E_s(\boldsymbol{q}) = \alpha_{P200}F_{P200}(\boldsymbol{q}) + \alpha_A F_A(\boldsymbol{q})e^{i\boldsymbol{q}\cdot\boldsymbol{d}} + \alpha_D F_D(\boldsymbol{q})e^{-i\boldsymbol{q}\cdot\boldsymbol{d}},$$

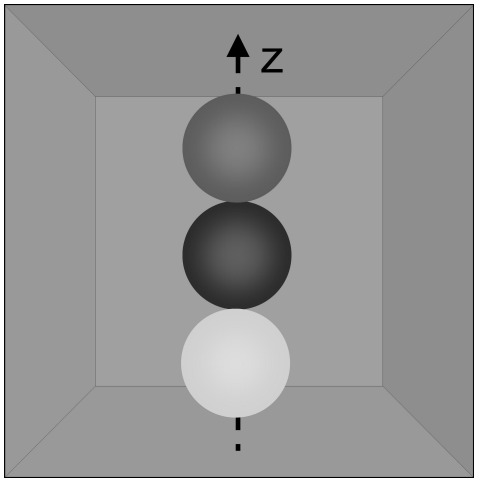

Figure 6.16: "Traffic light" model of SP perturbations around a P200 PP. Gray levels reflect different refractive indexes: clear spherical volume ($n = 1.333$), background ($n = 1.336$), dark spherical volume ($n = 1.338$), P200 ($n = 1.59$).

where $\alpha_A = -\alpha_D$ (α_D defined as in Equation 6.25). For simplicity we assumed that the accumulation and depletion regions have the same radius R of the P200 particles and thus results:

$$F_{P200}(\boldsymbol{q}) = F_D(\boldsymbol{q}) = F_A(\boldsymbol{q}).$$

Moreover we assumed the axis of the "traffic light" along the z direction and the distance $\boldsymbol{d}$ between the center of the particle and that of the two surrounding spherical regions equals to $2R$. We then considered light polarized along z and along y directions and we calculated the scattered intensity at a certain $\boldsymbol{q}$ as:

$$I(\boldsymbol{q}) = |E_s(\boldsymbol{q})|^2 \, sen^2\Psi \tag{6.26}$$

where $sen^2\Psi$ accounts for the toroid of polarization with Ψ angle between the light polarization direction and the scattering direction. The total scattered intensity has been calculated by integrating Equation 6.26 over the whole scattering directions. By comparing the scattering of the "traffic light" with that of the particle alone we found that the $\delta\phi_1$ distribution of SP does not modify the scattering of the particle. We verified that the presence of non negligible form factor does not affect the result that light scattering experiments can reveal only $\delta\phi_2$ concentration modifications.

To explain our experimental observations we conjectured a simple geometry for the distribution $\delta\phi_2$, as the one sketched in Figure 6.17(a), where the SP concentration is incremented within two spherical regions along E direction of radius R_S while is depleted within a toroidal region having inner diameter equals to that of the P200 and radius equal to R_T centered on E. To calculate the scattered intensity we used the same procedure as for the "traffic light" with a proper form factor

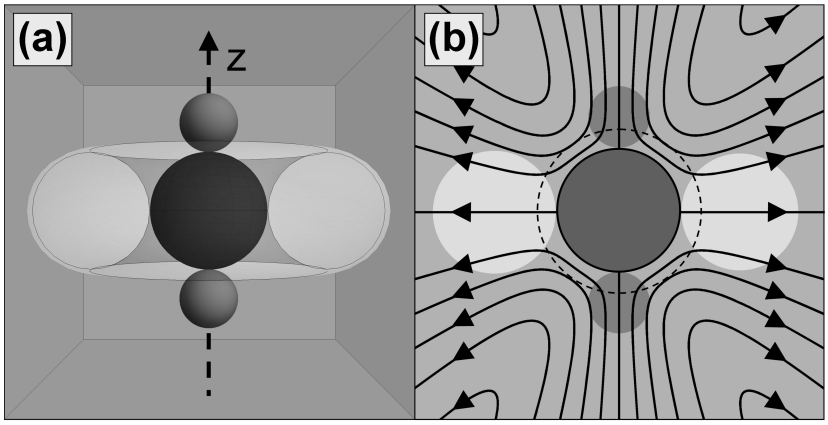

Figure 6.17: $O(E^2)$ perturbations around a P200 PP: (a) geometrical model of $\delta\phi_2$ used to quantitatively match the scattering data in Figure 6.13(b) for $\nu = 100\,Hz$ and $E = 15\,Vmm^{-1}$. The SP density is incremented ($\delta\phi_2 > 0$) within two spherical region along E and decreased ($\delta\phi_2 < 0$) within an equatorial toroidal region with inner section equal to that of P200 particle. Gray levels reflect different resulting refractive indexes: toroid ($n = 1.335$), background ($n = 1.336$), spherical volume ($n = 1.337$), P200 ($n = 1.59$). (b) $O(E^2)$ solvent flows around a P200 drown according to the model in [14, 15]. The dashed line represents the SP exclusion shell.

for the accumulation and depletion regions. Also in this case the polarizability of the spherical and toroidal regions have been calculated according to Clausius-Mossotti equation:

$$\alpha_S = \frac{n_S^2 - n_{mean}^2}{n_S^2 + 2n_{mean}^2}$$

$$\alpha_T = \frac{n_T^2 - n_{mean}^2}{n_T^2 + 2n_{mean}^2}$$

where the refractive indexes of the sphere n_S and of the toroid $_T$ have been kept as free parameters of the model, with the only assumption of $n_S > n_{mean}$ and $n_T < n_{mean}$. In particular we have expressed n_S and n_T through the rate of accumulation (f_a) and depletion (f_d) of SP:

$$\alpha_S = n_{mean} + f_a(n_{mean} - n_{H_2O})$$
$$\alpha_T = n_{mean} - f_d(n_{mean} - n_{H_2O})$$

We varied f_a, f_d, R_S and R_T to reproduce the turbidity variations observed in experiments. The extensions of the two regions R_S and R_T have been estimated through the recovery time t_{ETLI}, the time necessary to the scattering anomaly to diffuse away after the electric field is switched off. Since $t_{ETLI} \cong 6$ ms corresponds to an SP diffusion over about 350 nm, we assumed the toroidal region having the same section of the P200 and we found we could reproduce experimental data with $R_S = 100$ nm, $n_T = 1.335$ and spherical volume $n_S = 1.337$, which correspond to an SP depletion and accumulation of 20% and 50% respectively.

We verified that the field-induced SP arrangement can not be ascribed to an induced dipole-induced dipole interaction, which would produce too weak forces and too high characteristic frequency in the MHz Maxwell-Wagner regime. The SP density distribution can instead be related to the presence of $O(E^2)$ electro-osmotic flows around the large particles, as those sketched in Figure 6.17(b). In the next section we will describe the $O(E^2)$ electro-osmotic flows that we conjecture responsible of the clearing in both rod-sphere and sphere-sphere mixtures and of the anomalous hydrodynamic torque in bidisperse mixtures of rod-like and spherical particles.

6.4 $O(E^2)$ electro-osmotic flows

As described in chapter 5, electro-osmotic flows originate as a consequence of electric force acting on the charge fluid inside the particle's electric double layer. In particular, in the case of symmetric double layer, $O(E)$ fluxes originate in the proximity of the charged surface. However, in presence of $O(E)$ polarization effect, the electric double layer looses its symmetry: the resulting electro-osmotic fluxes will present also an $O(E^2)$ dependence. In this case standard electrokinetic model does not adequately describe the hydrodynamics of the system.

The "ICEO" model introduced in section 5.5 applies to uncharged, highly polarizable particles. In this case, there are no $O(E)$ flows so that $O(E^2)$ flows are the dominant effect generated by the presence of an electric field in the system. The condition is thus rather different from ours: in charged system as our colloidal mixtures, $O(E)$ flows are not only present but usually play a prominent role, shading higher order terms in the flow field . However, as highlighted in the former section, due to basic optical reasons, we are not sensible to $O(E)$ structure and thus $O(E^2)$ flows can be detected. We drew our flow fields, here reported in Figure 6.17(b) according to the theoretical model proposed in [14, 15] which applies to charged dielectric particles and allows to explicitly calculate flow lines from zeta potential and ionic strength values.

We expect in general SP to be dragged along flow lines except when the flow runs too close to the PP surface, where SP are taken apart due to both steric and electrostatic repulsion. This exclusion shell, represented in Figure 6.17(b) through a dashed line, is larger than the electric double layer. Accordingly SP are excluded from the double layer region i.e. the region where the flow lines are the strongest. As a consequence SP accumulate at the PP poles and deplete the equatorial region around PP as observed in our experiments.

In this picture, the responsible mechanism at the base of $O(E^2)$ fluxes should be the concentration polarization effect, which perturbs the double layer structure generating an asymmetric charge

distribution. However the characteristic frequency of the phenomenon $\nu_{mix} \approx D_{SP}/R_{PP}^2 < \nu_\alpha$. Moreover, the 1 ms time required to the toroidal depleted region to establish, would require higher flow velocities than the ones predicted in [14, 15] for standard particles in simple electrolyte. Both these facts suggest that the SP being charged are not passive probes of the $O(E^2)$ field-induced flows but play an active role in greatly affecting the flows field, generating a giant and slow electro-osmotic phenomenon.

Similar considerations can be done to explain the anomalous orientation observed in mixtures of PTFE and secondary spherical particles. As for the sphere-sphere mixtures, the characteristic frequency of the phenomenon $\nu_{mix} < \nu_\alpha$ suggests the presence of a new electrokinetic effect. Moreover, as shown in subsection 2.3.1, at low frequency the hydrodynamic torque σ_H plays a significant role in determining particles orientation. $\sigma_H = \int dS \boldsymbol{r} \times f(\boldsymbol{r})$, where $f(\boldsymbol{r})$ is the viscous force acting on the particle surface S and thus directly related to the electro-osmotic flows inside the dispersion. In his numerical model, Fixman showed that while the electric torque σ_E is always positive, σ_H assumes negative values in presence of slowly diffusing coions [32]. Thus the giant negative torque observed in PTFE+SP mixture at a frequency $\nu_{mix} < \nu_\alpha$ indicates the presence of a new electrokinetic phenomenon involving SP.

6.5 Colloidal concentration polarization

All the data showed in this thesis indicate the presence of a new electrokinetic phenomenon that by analogy we call "colloidal concentration polarization". As the electric field is turned on, SP accumulate for mobility mismatch on one side of the larger PP (PTFE or P200 particles) while depleting on the other side, generating an $O(E)$ SP distribution $\delta\phi_1 \neq 0$. This accumulation continues until it is compensated at $\nu < \nu_{mix}$ by the diffusion of the SP across the PP, a phenomenon similar to the electrolyte "concentration polarization". This polar SP distribution cannot be detected through ETLI experiments due to symmetry properties of the particles density and of the relative scattered fields. However we expect this "colloidal concentration polarization", being SP charged, to greatly affect PP double layer structure generating an enhancement of the non-linear electro-osmotic flows. At $\nu < \nu_{mix}$ such $O(E^2)$ flows could have the amplitude required to create the $\delta\phi_2 \neq 0$ SP distribution around P200 and to account for the large negative torque experienced by PTFE particles.

Acknowledgments

L'esperienza di questi anni di dottorato è stata per me momento decisivo di crescita professionale e umana. Per questo desidero ringraziare coloro che in essa mi sono stati compagni.

Innanzitutto desidero ringraziare il mio tutore Tommaso Bellini per avermi guidato con pazienza e grande disponibilità in un campo tanto complesso come l'elettrocinetica non lineare. Lo ringrazio per avermi insegnato che, per fare ricerca, è necessario amare ciò che si studia. Questa provocazione mi ha accompagnato nel lavoro del dottorato e in ogni aspetto della vita.

Grazie a Davide Pini per le utilissime discussioni sui contenuti della tesi.

Grazie a tutti gli amici del laboratorio di Fluidi complessi:

grazie a Cecco e Marco per l'attenzione che mi hanno sempre dedicato;

grazie a Roberto, Giuliano, Silvia, Matteo, Fabio, Tommy, Ben, Vale...nelle vicende di questi anni mi siete stati vicini con un affetto straordinario!

Grazie a tutti coloro che hanno reso possibile questo lavoro:

i miei genitori, Anna, Marta, Patrizia e i tantissimi amici che mi hanno accompagnato e sostenuto con commuovente disponibilità.

Grazie a Mattia e Letizia per avermi rivoluzionato la vita! Grazie anche per aver voluto condividere con me ogni istante di questa tesi.

Grazie a Pietro, grande compagno nel cammino della vita.

Grazie a don Giussani e don Carron perchè con la vostra compagnia e amicizia sto scoprendo il meglio.

Bibliography

[1] E. J. W. Verwey and J. T. G. Overbeek. *Theory of the Stability of Lyophobic Colloids*. Elsevier, Amsterdam, 1948.

[2] M. P. Valignat, O. Theodoly, J. C. Crocker, W. B. Russel, and P. M. Chaikin. *PNAS*, 102:4225, 2005.

[3] M. M. Baksh, M. Jaros, and J. T. Groves. *Nature*, 427:139, 2004.

[4] J. M. de la Fuente and S. Penades. *Glycoconjugate J.*, 21:149, 2004.

[5] A. J. Reynolds, A. H. Haines, and D. A. Russel. *Langmuir*, 22:1156, 2006.

[6] J. M. de la Fuente, A. G. Barrientos, T. C. Rojas, J. Rojo, J. Canada, A. Fernandez, and S. Penades. *Angew. Chem. Int. Ed.*, 40:2258, 2001.

[7] J. M. de la Fuente, P. Eaton, A. G. Barrientos, M. Menendez, and S. Penades. *J. Am. Chem. Soc.*, 127:6192, 2005.

[8] D. Prosperi, C. Morasso, Mantegazza. F., M. Buscaglia, L. Hough, and T. Bellini. *Small*, 2:1060, 2006.

[9] F. F. Reuss. *Mem. Soc. Imperiale Naturalistes de Moscow*, 2:327, 1809.

[10] J. Lyklema. *Fundamentals of Interface and Colloid Science*, volume II. Solid-Liquid Intefaces. Academic Press, London, 1995.

[11] W. B. Russel, D. A. Saville, and W. R. Schowalter. *Colloidal Dispersions*. Cambridge University Press, 1989.

[12] J. L. Anderson. *Annu. Rev. Fluid Mech.*, 21:61, 1989.

[13] T. M. Squires and M. Z. Bazant. *J. Fluid. Mech.*, 509:217, 2004.

[14] N. I. Gamayunov, V. A. Murtsovkin, and A. S. Dukhin. *Colloid J. USSR*, 48:197, 1986.

[15] V. A Murtsovkin. *Colloid J.*, 58:341, 1996.

[16] T. M. Squires and M. Z. Bazant. *J. Fluid. Mech.*, 560:65, 2006.

[17] A. Ramos, H. Morgan, N. G. Green, and A. Castellanos. *J. Coll. Interface Sci.*, 217:420, 1999.

[18] A. Adjari. *Phys. Rev. E*, 61:R45, 2000.

[19] A. B. D. Brown, C. G. Smith, and A. R. Rennie. *Phys. Rev E*, 63:016305, 2001.

[20] V. Studer, A. Pepin, Y. Chen, and A. Ajdari. *Micreoelec. Eng.*, 61-2:915, 2002.

[21] M. Mpholo, C. G. Smith, and A. B. D. Brown. *Sens. Act. B*, 92:262, 2003.

[22] D. G. Grier. *Nature*, 424:267, 2003.

[23] F. Mantegazza, M. Caggioni, M. L. Jimenez, and T. Bellini. *Nature Phys.*, 1:103, 2005.

[24] B. J. Berne and R. Pecora. *Dynamic Light Scattering*. Claredon Press, 1996.

[25] C. T. O' Konski. *Molecular electro-optics*. Marcel Dekker, New York, 1976.

[26] T. Bellini, V. Degiorgio, and F. Mantegazza. *Colloids Surf., A*, 140:103, 1998.

[27] H. Watanabe and A. Morita. *Adv. Chem. Phys.*, 56:255, 1984.

[28] E. H. B. De Lacey and L. R. White. *J. Chem. Soc., Faraday Trans. 2*, 77:2007, 1981.

[29] E. J. Hinch, J. D. Sherwood, W. C. Chen, and P. N. Sen. *J. Chem. Soc., Faraday Trans 2*, 80:535, 1984.

[30] W. C. Chew and P. N. Sen. *J. Chem Phys.*, 77:4683, 1982.

[31] R. W. O'Brien. *J. Coll. Interface Sci.*, 92:204, 1983.

[32] Marshall Fixman. *J. Chem. Phys.*, 124:214506, 2006.

[33] H. C. van de Hulst. *Light Scattering by Small Particles*. 1957.

[34] W. Brown. *Light scattering - Principles and development.* Claredon Press, 1996.

[35] M. Corti and V. Degiorgio. *J. Chem. Phys.*, 85:711, 1950.

[36] B. U. Federhof. *J. Phys.: Math. Gen.*, 11:929, 1978.

[37] G. K. Batchelor. *J. Fluid. Mech.*, 74:1, 1976.

[38] P. H. Wiersema, A. L. Loeb, and J. Th. G. Overbeek. *J. Coll. Interface Sci.*, 22 (1):78, 1966.

[39] B. V. Derjaguin. *Kolloid Z.*, 69:155, 1934.

[40] S. Alexander, P. M. Chaikin, P. Grant, G. J. Morales, P. Pincus, and D. Hone. *J. Chem. Phys.*, 80:11, 1984.

[41] E. Trizac, L. Bocquet, M. Aubouy, and H. H. von Grunberg. *Langmuir*, 19 (9):4027, 2003.

[42] R. O. Watts, D. Henderson, and R. J. Baxter. *Adv. Chem. Phys.*, 21:421, 1971.

[43] R. J. Baxter. *J. Chem. Phys.*, 49:6, 1968.

[44] F. Reif. *Fundamental of statistical and termal physics*. 1985.

[45] C. T. O'Konski and B. H. Zimm. *Science*, 111:113, 1950.

[46] M. A. Lauffner. *J. Am. Chem. Soc.*, 61:2412, 1939.

[47] T. Bellini and F. Mantegazza. *Interfacial Electrokinetics and Electrophoresis*. CRC, 2001.

[48] M. Mandel and T. Odijk. *Ann. Rev. Phys. Chem.*, 35:75, 1984.

[49] C. T. O' Konski. *J. Chem. Phys.*, 60:64, 1960.

[50] S. S. Dukhin and V. N. Shilov. *Adv. Coll. Interface Sci.*, 80:535, 1984.

[51] R. W. O' Brien and W. N. Rowlands. *J. Coll. Interface Sci.*, 159:471, 1993.

[52] F. Mantegazza, T. Bellini, M. Buscaglia, V. Degiorgio, and D. A. Saville. *J. Chem. Phys.*, 113:6984, 2000.

[53] T. Bellini, F. Mantegazza, V. Degiorgio, R. Avallone, and D. A. Saville. *Phys. Rev. Lett.*, 82:5160, 1999.

[54] M. Fixman. *J. Chem. Phys.*, 72:5177, 1980.

[55] L. Fornasari, F. Mantegazza, M. L. Jimenez, M. Buscaglia, and T. Bellini. *Phys. Rev. E*, 79:060401, 2009.

[56] R. Klein and B. D'Aguanno. *Static scattering properties of colloidal suspensions. In Light Scattering: Principles and Development*. Claredon Press, Oxford, 1996.